UNIVERSITY OF CALIFORNIA, SAN DIEGO

Anomalous Magnetization Reversal in Exchange Biased Thin Films and Nanostructures

A dissertation submitted in partial satisfaction of the
requirements for the degree Doctor of Philosophy
in
Physics

by

Zhi-Pan Li

Committee in charge:

Professor Ivan K. Schuller, Chair
Professor Neal Bertram
Professor Sunil K. Sinha
Professor Harry Suhl
Professor Edward Yu

2006

The dissertation of Zhi-Pan Li is approved, and it is acceptable in quality and form for publication on microfilm:

Chair

University of California, San Diego

2006

TABLE OF CONTENTS

LIST OF FIGURES

LIST OF TABLES

ACKNOWLEDGEMENT

First of all, it is my pleasure to thank my girlfriend, Xiaowei Zheng, for her love and support throughout the years. Without her, I would not have even considered joining UCSD, and Ivan's renowned magnetism group, and without her encouragement and support, I would not have completed my thesis so smoothly. She made everyday of the past four years at UCSD a joyful and unforgettable experience. And her exuberating enthusiasm toward work and high moral and academic standard for herself have always inspired me to become a better person and a passionate researcher.

Second and also foremost, I would like to thank my adviser Ivan Schuller for his support and inspiration. I have learned a lot from his personality and research experience, and wish I could have done better. I am very much obliged to his deep care for the students on how to do solid research, write papers, prepare for conferences, and establish oneself in the community. His criticism of my occasional carelessness, encouragement of becoming a more independent researcher, and generosity to send me to various conferences to present my work and meet with people made my four years at UCSD a full and fruitful experience.

I am also very lucky to have overlapped with my colleagues in the group, who are always so generous and sharing. Working with Dr. Johannes Eisenmenger and Oleg Petracic helped me grasp much of the experimental and theoretical aspects of exchange bias and magneto-optics, diversify my research topics, and establish valuable collaborations. Collaborating with Dr. Igor Roshchin, Rafael Morales, Casey Miller, Xavier Batlle on various topics on and beyond this thesis has been such a constructive and delightful experience, from which I have learned so much not only about exchange bias or magnetism in general, but also about how to build a strong and constructive collaborative relationship with your colleagues. I am confident that we will carry on the collaboration as far as our career in physic goes. I also have to thank Changpeng Li and Dr. Thomas Gredig for their il-

luminating discussion, and frank suggestion on my research and papers. Also, it has been my great pleasure to work with many ingenious and brilliant researchers outside the group: professor Sunil Sinha and Dr. Sujoy Roy at UCSD, professor Kai Liu and his student Justin Olamit at UC Davis, Dr. Mike Fitzsimmons and Brian Kirby at Los Alamos National Lab. From them, I have learned so much about different experimental techniques, like x-ray and neutron scattering, vector magnetometry, etc. Also, through countless communications and meetings, we together have established a better understanding of exchange bias phenomenon.

Finally, I would like to thank all my committee members for their support and valuable suggestion on my work. And I also want to express my deep gratitude to my parents for their continuous support and understanding of my life and work at US.

The text of chapter II, in part, is a reprint of the material as it appears in Oleg Petracic, Zhi-Pan Li, Igor V. Roshchin, M. Viret, R. Morales, X. Batlle, and Ivan K. Schuller, "*Bi-domain state in the exchange bias system FeF_2/Ni*," Appl. Phys. Lett. **87**, 222507, © 2005 American Institute of Physics, where the dissertation author was the second author, Igor Roshchin, Oleg Petracic, Rafael Morales, Zhi-Pan Li, X. Batlle and Ivan K. Schuller, "*Lateral length scales in exchange bias*," Europhys. Lett., **71**, 297, © 2005 Institute of Physics, where the dissertation author was the fourth author, and Justin Olamit, Elke Arenholz, Zhi-Pan Li, Oleg Petracic, Igor V. Roshchin, R. Morales, X. Batlle, Ivan K. Schuller, and Kai Liu, "*Loop Bifurcation and Magnetization Rotation in Exchange Biased Ni/FeF_2*," Phys. Rev. B **72**, 012408, © 2005 The American Physical Society, where the dissertation author was the third author. The co-authors in this publication directed, supervised, and co-worked on the research which forms the basis of this chapter.

The text of chapter III, in part, is a reprint of the material as it appears in Zhi-Pan Li, Oleg Petracic, Rafael Morales, Justin Olamit, Xavier Batlle,

Kai Liu, and Ivan K. Schuller, "*Asymmetric Reversal in Inhomogeneous Magnetic Heterostructures*," Phys. Rev. Lett. **96**, 217205 © 2006 The American Physical Society, where the dissertation author was the first author, and Zhi-Pan Li, Oleg Petracic, Johannes Eisenmenger, and Ivan K. Schuller, "*Reversal behavior of exchange-biased submicron dots*," Appl. Phys. Lett. **86**, 072501 © 2005 American Institute of Physics, where the dissertation author was the first author, R. Morales, Zhi-Pan Li, O. Petracic, X. Batlle and Ivan K. Schuller, "*Magnetization depth dependence and reversal processes in exchange coupled FeF_2/FM bilayer*," Appl. Phys. Lett. **89**, 072504 © 2006 American Institute of Physics, where the dissertation author was the second author, and Johannes Eisenmenger, Zhi-Pan Li, Waldemar A. A. Macedo, and Ivan K. Schuller, "*Exchange Bias and Asymmetric Reversal in Nanostructured Dot Arrays*," Phys. Rev. Lett. **94**, 057203 © 2005 The American Physical Society, where the dissertation author was the second author. The co-authors in this publication directed, supervised, and co-worked on the research which forms the basis of this chapter.

The text of chapter IV, in part, is a reprint of the material as it appears in Zhi-Pan Li, Johannes Eisenmenger, Casey W. Miller, and Ivan K. Schuller, "*Anomalous Spontaneous Reversal in Magnetic Heterostructures*," Phys. Rev. Lett. **96**, 137201 © 2006 The American Physical Society, where the dissertation author was the first author. The co-authors in this publication directed, supervised, and co-worked on the research which forms the basis of this chapter.

VITA

2000	B.S., Peking University, China
2002	M.S., Yale University
2006	Ph.D., University of California, San Diego

PUBLICATIONS

"Single-molecule signal enhancement using a high - impedance ground plane substrate." Krishanu Ray, Michael D. Mason, Celeste Yang, Zhi-Pan Li, and Robert D. Grober, Appl. Phys. Lett. **85**, 5520 (2004).

"Exchange Bias and Asymmetric Reversal in Nanostructured Dot Arrays." Johannes Eisenmenger, Zhi-Pan Li, Waldemar A. A. Macedo, and Ivan K. Schuller, Phys. Rev. Lett. **94**, 057203 (2005).

"Reversal behavior of exchange-biased submicron dots." Zhi-Pan Li, Oleg Petracic, Johannes Eisenmenger, and Ivan K. Schuller, Appl. Phys. Lett. **86**, 072501 (2005).

"Lateral length scales in exchange bias." Igor Roshchin, Oleg Petracic, Rafael Morales, Zhi-Pan Li, X. Batlle and Ivan K. Schuller, Europhys. Lett., **71**, 297 (2005).

"Loop Bifurcation and Magnetization Rotation in Exchange Biased Ni/FeF_2." Justin Olamit , Elke Arenholz, Zhi-Pan Li, Oleg Petracic, Igor V. Roshchin, R. Morales, X. Batlle, Ivan K. Schuller, and Kai Liu, Phys. Rev. B **72**, 012408 (2005).

"Depth profile of uncompensated spins in an exchange bias system ." S. Roy, M.R. Fitzsimmons, S. Park, M. Dorn, O. Petracic, Igor V. Roshchin, Zhi-Pan Li, X. Batlle, R. Morales, A. Misra, X. Zhang, K. Chesnel, J.B. Kortright, S.K. Sinha and Ivan K. Schuller, Phys. Rev. Lett. **95**, 047201 (2005).

"Bi-domain state in the exchange bias system FeF_2/Ni." Oleg Petracic, Zhi-Pan Li, Igor V. Roshchin, M. Viret, R. Morales, X. Batlle, and Ivan K. Schuller, Appl. Phys. Lett. **87**, 222507 (2005).

"Angular Dependence of Exchange Anisotropy on Cooling Field in FM/Fluoride Thin Films." Justin Olamit, Zhi-Pan Li, Ivan K. Schuller, Kai Liu, Phys. Rev. B. **73**, 24413 (2006).

"Magnetization reversal of uncompensated Fe moments in exchange biased Ni/FeF_2 bilayers." Elke Arenholz, Kai Liu, Zhi-Pan Li and Ivan K. Schuller, Appl. Phys. Lett. **88**, 072503 (2006).

"Anomalous Spontaneous Reversal in Magnetic Heterostructures." Zhi-Pan Li, Johannes Eisenmenger, Casey W. Miller, and Ivan K. Schuller, Phys. Rev. Lett. **96**, 137201 (2006).

"Asymmetric Reversal in Inhomogeneous Magnetic Heterostructures."Zhi-Pan Li, Oleg Petracic, Rafael Morales, Justin Olamit, Xavier Batlle, Kai Liu, and Ivan K. Schuller, Phys. Rev. Lett. **96**, 217205 (2006).

"Magnetization depth dependence and reversal processes in exchange coupled FeF_2/FM bilayer." R. Morales, Zhi-Pan Li, O. Petracic, X. Batlle and Ivan K. Schuller, Appl. Phys. Lett. **89**, 072504 (2006).

"Combined neutron and synchrotron studies of magnetic films." Sunil K. Sinha, Sujoy Roy, M. R. Fitzsimmons, S. Park, M. Dorn, Oleg Petracic, Igor V. Roshchin, Zhi-Pan Li, Xavier Batlle, Rafael Morales, A. Misra, X. Zhang, K. Chesnel, J. B. Kortright, Ivan K. Schuller, Pramana - J. Phys. **67**, 47 (2006).

FIELDS OF STUDY

Physics

ABSTRACT OF THE DISSERTATION

Anomalous Magnetization Reversal in Exchange Biased Thin Films and Nanostructures

by

Zhi-Pan Li
Doctor of Philosophy in Physics
University of California, San Diego, 2006
Professor Ivan K. Schuller, Chair

When a ferromagnet/antiferromagnet (FM/AF) bilayer is cooled below the Néel temperature T_N of the AF in a magnetic field, exchange bias (EB) phenomenon arises. Although EB was discovered nearly 50 years ago, a general understanding is still lacking regarding the competing interactions and length scales involved and how they give rise to a rich variety of magnetization reversal behavior. In this thesis, I will address these questions by studying the cooling field dependence, asymmetric magnetization reversal, and spontaneous reversal in epitaxial FeF_2 / polycrystalline FM bilayers. Two types of transitions from negative to positive EB with increasing cooling fields were found: for in-plane twinned FeF_2, a continuous transition was found, while coexistence of EB of both signs was observed for untwinned FeF_2. This is attributed to the relevance between the AF "domain" size and the FM domain wall width and confirmed by micromagnetic simulation. Nanostructuring the FM significantly decreases the onset cooling field for positive EB with decreasing dot sizes when the FM dot size is comparable with the AF "domain" size ($\sim$500nm). The high quality epitaxial exchange bias system also constitutes a model system for studying magnetization reversal asymmetry. By vector magnetometry and simulation, we found that the FM reverses through parallel domain walls, which results in highly asymmetric hysteresis loops. Also, the FM near the FM/AF interface exhibits a more asymmetric reversal than that

farther away from the interface. These results unambiguously show the existence of a FM parallel domain wall and its importance in asymmetric magnetization reversal. Moreover, we found another surprising phenomenon that when positively exchange biased, the FM can spontaneously reverse its magnetization in a constant field when cooled below T_N due to the strong interfacial coupling. When heating up in the same field, the FM magnetization reverses at $T > T_N$, giving rise to a tunable thermal hysteresis. Discovery of this phenomenon suggests a revised energy competition mechanism for positive EB, which includes parallel FM and AF domain wall energy. By studying these different but strongly related magnetization reversal behaviors, we demonstrated the central role of competing length scales and interactions in heterostructured magnetic systems.

I

Introduction

When a ferromagnet/antiferromagnet (FM/AF) bilayer is cooled below the Néel temperature T_N of the AF in a magnetic field (H_{FC}), the so-called exchange bias (EB) effect arises [1, 2, 3]. It is manifested as a shift of the hysteresis loop along the magnetic field axis. The magnitude of the shift is defined as the exchange bias field H_{EB}. EB is also described as a unidirectional anisotropy due to the single fold symmetry over 360° rotation in the sample plane [1]. EB has been intensely studied in the past ten years due to its significance in providing a magnetic reference in spintronics devices such as spin valve and magnetic tunneling junctions [4]. Also, as magnetic nanostructures become smaller as a result of modern nanofabrication techniques, they can become magnetically unstable when the anisotropy energy barrier can be readily overcome by thermal fluctuation. EB was found to be able to provide an additional anisotropy to stabilize the magnetization. More importantly, it is of physical significance in understanding competing interactions and relevant length scales of two coupled magnetic materials. A rich variety of physical phenomena, *e.g.*, magnetization reversal asymmetry [5], thermal stability [6, 7], positive EB [8], training effect [9, 10] have been found. This motivates us to look into how the interfacial exchange interaction couples two dissimilar systems with different length and energy scales, and modifies their magnetic response. In this thesis, I will demonstrate how the cooling field dependence

(Chapter II), asymmetric magnetization reversal (Chapter III), and spontaneous magnetization reversal (Chapter IV) can be induced and tuned by controlling critical length scales and energies in exchange bias in a simple model system, epitaxial-FeF_2/polycrystalline-FM bilayer. Below I will first give a brief introduction to the current understanding of exchange bias (Section I.A). Then, the system of interest FeF_2/FM (Section I.B), experimental techniques (Section I.C), and simulation methods (Section I.D) employed in this thesis will be introduced.

I.A General Understanding of Exchange Bias

EB is generally believed to be due to the exchange coupling between the FM and AF across the interface. The simplest EB model, Meiklejohn-Bean model, assumes the FM with negligible anisotropy reverses by coherent rotation, while the AF with infinite uniaxial anisotropy is frozen (Fig. I.1). Thus, the EB field can evaluated as $\mu_0 H_{EB} = -J_{FM/AF}\mathbf{S}_{FM} \cdot \mathbf{S}_{AF}/(M_{FM}t_{FM})$ [1, 2]. Here, $J_{FM/AF}$ is the interfacial coupling between FM and AF interfacial moments $\mathbf{S}_{FM}$ and $\mathbf{S}_{AF}$. M_{FM} and t_{FM} are the saturation magnetization and thickness of the FM, respectively. This model can explain many important experiment observations, *e.g.*, $1/t_{FM}$ thickness dependence of H_{EB} [11]. It also predicts that H_{EB} is directly proportional to $\mathbf{S}_{AF}$. However, using the ideal $\mathbf{S}_{AF}$ for nominally uncompensated AF interface strongly overestimates H_{EB}. Moreover, while the formula predicts zero EB for a nominally compensated AF interface, significant EB was found experimentally [12].

Various theoretical models have been proposed to address the discrepancy. Some models believe that EB can be induced without uncompensated interfacial AF moments. Instead, EB arises from perpendicular coupling [13] or absorption and emission of spin waves at the interface [14]. Other models claim that uncompensated interfacial moments are essential to EB, and Meiklejohn-Bean model is correct if appropriate $\mathbf{S}_{AF}$ is assumed. In general, these models fall into two major

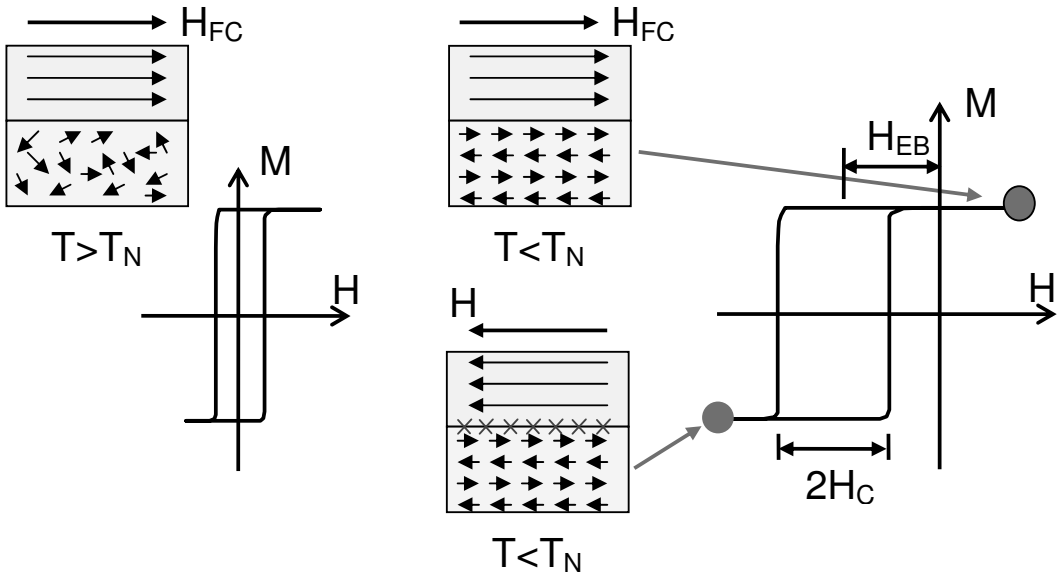

Figure I.1: The schematic spin configurations and hysteresis loops of the FM and AF at temperatures above and below T_N according to Meiklejohn-Bean model, assuming ferromagnetic interfacial coupling. The two layers from top to bottom are FM and AF layers, respectively. The AF moments are disordered at $T > T_N$ and frozen at $T < T_N$. The crosses at the FM/AF interface indicates that the interfacial coupling is frustrated.

categories. Models in the first category assume AF or FM domains parallel to the interface [15, 16, 17], where winding and unwinding of the domain walls reduces the effective interfacial moments, or interfacial AF moments deviate from their bulk configuration to account for non-zero $\mathbf{S}_{AF}$ [13, 18, 16]. Models assuming perpendicular AF domains were also proposed, where uncompensated AF moments arise from surface roughness[19], spin counting statistics in finite AF grains [20], piezomagnetism [21], or domain states due to bulk defects[22].

Recent experimental effort has focused on searching for evidence of either parallel or perpendicular domains. AF parallel domains have been observed by magnetometry [23, 24], Brillouin light scattering [25] and XMLD experiment [26], but their relationship with EB remains unclear. In the XMLD experiment, for example, evidence of parallel AF domain walls were observed in systems with negligible H_{EB}, while in systems with much larger H_{EB}, parallel AF domain walls become much less significant. Moreover, very large H_{EB} was found in systems

with large anisotropies, like FeF_2 [12] and CoO. This seems to suggest that a soft AF, in which parallel domain walls can be easily promoted, is not favorable for EB. Additionally, Ohldag *et al.* imaged with x-ray absorption spectroscopy uncompensated Ni spins in an ultra-thin NiCoOx layer forming at the surface of NiO upon Co deposition, where there is negligible exchange bias. They found these uncompensated Ni spins couple more strongly with the FM rather than AF, indicating that unpinned uncompensated moments are not responsible for exchange bias [27]. On the other hand, parallel FM domain walls have not been convincingly observed and were mostly ignored in most EB studies [28], probably because the interfacial coupling energy is much weaker than that in a conventional hard/soft magnetic structure where similar exchange spring was claimed [29, 30].

Perpendicular domain structures in the AF have been very intensely studied, in order to quantify the amount of uncompensated moments near the FM/AF interface. A recent experiment showed that the domain state in the volume of the AF created by diluting CoO by MgO can result in perpendicular domain walls extending to the FM/AF interface, causing increased uncompensated interfacial moments, supporting the domain state model [31]. This model was also supported by many other experiments [32, 33, 34, 35, 21, 36], but it always requires a significant amount of dilution in the AF either by impurities or defects to create the desired domain state. Takano *et al.* found about 1% of the interfacial AF moments are uncompensated and pinned on CoO surface, which coincides with the estimate from spin counting statistics in AF grains [20]. Using X-ray magnetic circular dichroism (XMCD) measuring the total electron yield (TEY) in Co/NiO, Co/IrMn, and CoFe/PtMn bilayers, approximately 0.5 monolayer of uncompensated moments were found, yet only 8% of those moments are pinned and responsible for EB [37]. Similarly, magnetic force microscopy (MFM) experiment found about 7% coverage of pinned interfacial uncompensated AF spins, which gives H_{EB} of the right order of magnitude using the Meiklejohn-Bean model [38]. Pinned moments were also observed in the bulk of the AF, and found to be crucial

to EB [39]. Although there is a large amount of theoretical and experimental work in the literature, key questions about the roles of pinned and unpinned, interfacial and bulk AF moments remain unresolved.

A related problem to AF domain structures is how the FM reverses when exchange biased. Fitzsimmons *et al.* found by neutron scattering a significant spin-flip scattering intensity in the decreasing-field hysteresis branch, while in the increasing branch the intensity is below the noise level [5]. This suggests that the reversal processes are asymmetric between the two field sweeping directions. From the symmetry point of view, for a system without unidirectional anisotropy, positive and negative magnetic field directions are equivalent, and this is also required by time-reversal symmetry. This is manifested in odd-symmetric magnetic hysteresis loops and reversal processes, or $M(+H) = -M(-H)$. However, EB or unidirectional anisotropy breaks this time-reversal symmetry, and favors the magnetization to be in one of the two orientations. Thus, the magnetic hysteresis is no long symmetric, and the two reversal processes may be also different. In fact, asymmetric magnetization reversal has been studied by polarized neutron reflectometry (PNR) [5], photoemission electron microscopy (PEEM) [40], magneto-transport [41], Lorenz transmission electron microscopy (TEM) [42], magneto-optical indicator film (MOIF) [43], and magneto-optical Kerr effect (MOKE) [44]. In some systems, the reversal in the decreasing field branch is dominated by transverse magnetic moments, a phenomenon that was interpreted as due to coherent magnetic rotation. The absence of transverse moments in the increasing field branch was interpreted as domain wall propagation [5, 40]. Different, even opposite scenarios were also found [44, 45], for example, asymmetrically kinked hysteresis [46], training induced reversal asymmetry [47], etc. With well established experimental evidence, theoretical models were proposed and studied by Monte-Carlo simulation [48], Stoner-Wolfarth calculation [49], or micromagnetic simulation [50]. The most convincing argument thus far has been the competition between uniaxial and unidirectional anisotropies [49], but how they compete with each other and result

in the reversal asymmetry remains unclear. The origin of magnetization reversal asymmetry in EB systems remains a controversial and highly debated issue, and a unified and general understanding is lacking. In Chapter III, I will demonstrate that there are two main competing mechanisms for asymmetric reversal: the first is parallel FM domain walls, and the second is the competition between unidirectional and uniaxial anisotropy.

Another interesting phenomenon specific but not limited to the fluoride EB system is positive EB [8]. Here, the sign of EB is defined with respect to H_{FC}. When the hysteresis loop is shifted opposite to H_{FC}, we define EB to be negative, otherwise, EB is positive. While most EB systems exhibit negative EB, a few systems containing FeF_2 [51], $FeZnF_2$ [33], MnF_2 [52], magnetic oxides like $La_{0.67}Sr_{0.33}MnO_3/SrRuO_3$ [53], or ferrimagnet systems like FeSn/FeGd [54] exhibit positive EB, and in some cases EB of both signs. The sign of EB can be controlled by environmental variables, like cooling field [51, 52], temperature [33, 55], or changes of AF domain states in the bulk [56, 33] or at the interface [57]. Among these, fluoride systems (FeF_2 and MnF_2) represent a most typical system for positive EB because when positive exchange biased, they exhibit virtually all experimental features found in negative EB case, including very similar temperature evolution. In this case, the sign of EB can be tuned by H_{FC}, and is commonly believed to be due to the competition between the antiferromagnetic interfacial coupling and the Zeeman energy of uncompensated AF moments [51]. For a small H_{FC}, the antiferromagnetic coupling between the FM and AF favors negative uncompensated AF moments. At a low temperature, AF moments freeze in the negative orientation, thus stabilizing the FM in the positive direction and giving rise to negative EB. However, a large enough H_{FC} can overcome the interfacial coupling, align and eventually freeze AF moments in the field direction, and give rise to positive EB. By correlating the vertical shift of magnetic hysteresis loops with the sign of EB, Nogués *et al.* concluded that dominating AF interfacial coupling is a necessary condition for positive EB [51]. This was also recently

confirmed by measuring the vertical shift of the Fe hysteresis loop with XMCD [58], and magnetic depth profile with x-ray resonant scattering [39], and neutron scattering experiment in FeF_2/(Ni, Co) systems [59].

For an intermediate H_{FC}, H_{EB} gradually increases from negative to positive with increasing H_{FC}. This cooling field dependence is sample and roughness dependent. In the limit of small interfacial roughness, where the EB field value is nearly constant, in twinned FeF_2 systems, it was found that increasing roughness makes the system to go into positive EB at a smaller cooling field. In MnF_2, the opposite trend was found. Another interesting behavior in the transition from negative to positive EB is that the coercivity of the FM is enhanced when H_{EB} crosses zero [60]. Leighton *et. al.* suggests that for an intermediate H_{FC} the AF breaks into small subsystems with either positive or negative moments. Increasing H_{FC} changes the relative ratio of these two types of subsystems, and at the same time leads to frustration at the interface, and thus enhanced coercivity. In Chapter II, I will demonstrate that enhanced coercivity for an intermediate H_{FC} results from the comparison of the AF subsystem size and FM domain wall width. Also, In chapter IV, I will show that not only can the interfacial coupling compete with the AF Zeeman energy, it can also compete with the FM Zeeman energy under certain conditions, and give rise to thermally induced spontaneous magnetization reversal.

I.B Crystalline and Magnetic Properties of FeF_2

FeF_2 is an AF with Néel temperature $T_N = 78.4$ K. Its crystalline structure is body-center tetragonal, with $a = b = 4.70$ Å and $c = 3.31$ Å (Fig. I.2 (a)) (Table A.1). FeF_2 has a very large uniaxial anisotropy, $K_1 = 1.35 \times 10^4$ kJ/m^3 along the c axis [61]. Hence it can be considered as a model Ising system as verified by the measured universality class of FeF_2 at AF phase transition [62]. The exchange constants are J_1 (neighboring ions along c axis) = -0.048 cm^{-1}, J_2

(neighboring ions at the corner and body center of the unit cell) = 3.46 cm^{-1}, and J_3 (neighboring ions along a axis) = 0.149 cm^{-1} (J is defined in the way that the exchange energy is $\mathcal{H} = J\mathbf{S}_1 \cdot \mathbf{S}_1$). Clearly, the antiferromagnetic interaction between the body center and corner spins dominates over the other two. Therefore, at low temperatures, AF spins freeze along the [001] direction, with antiparallel corner and center spins (Fig. I.2 (a)) [63]. The above magnetic properties of FeF_2 are tabulated in Table A.3.

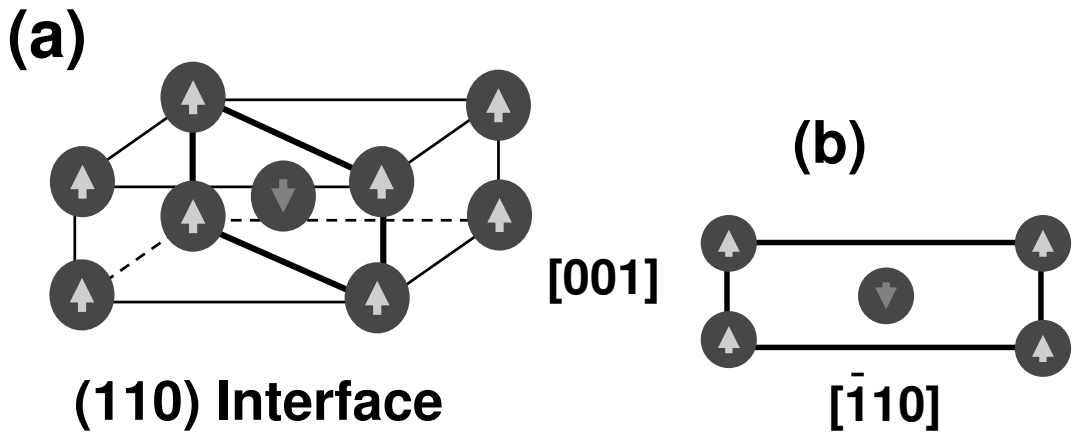

Figure I.2: (a) FeF_2 body-center tetragonal crystalline structure. Circles represent Fe atoms, with arrows in the center representing the orientation of Fe spins along c axis. F atoms are not shown. The thick lines mark the (110) surface. (b) FeF_2 (110) compensated surface.

FeF_2 (110) surface is of interest in this study. As shown in Fig. I.2 (b), this surface is nominally compensated, however exchange bias as large as 1.1 erg/cm^2 has been observed [12]. Two different FeF_2 in-plane structures were studied in this thesis. On MgO (100) substrates, FeF_2 grows twinned with [001] orientation of two neighboring AF grains perpendicular to each other, and at 45° with respect to MgO [001] direction (Fig. I.3 (a)). This is because MgO has a cubic crystalline structure, with a = 4.21 Å. On MgF_2 (110) substrates, FeF_2 grows untwinned with [001] of FeF_2 and MgF_2 parallel to each other (Fig. I.3 (b)) due to the same body-center tetragonal structure of MgF_2 as FeF_2, and similar lattice constants (Table A.1). The lattice constants of MgF_2 are $a = b$ = 4.62 Å and c = 3.05 Å,

about 1.7% mismatch with FeF_2 in a axis and 8.5% in c axis. The growth and characterization of epitaxial FeF_2 is detailed in the next section.

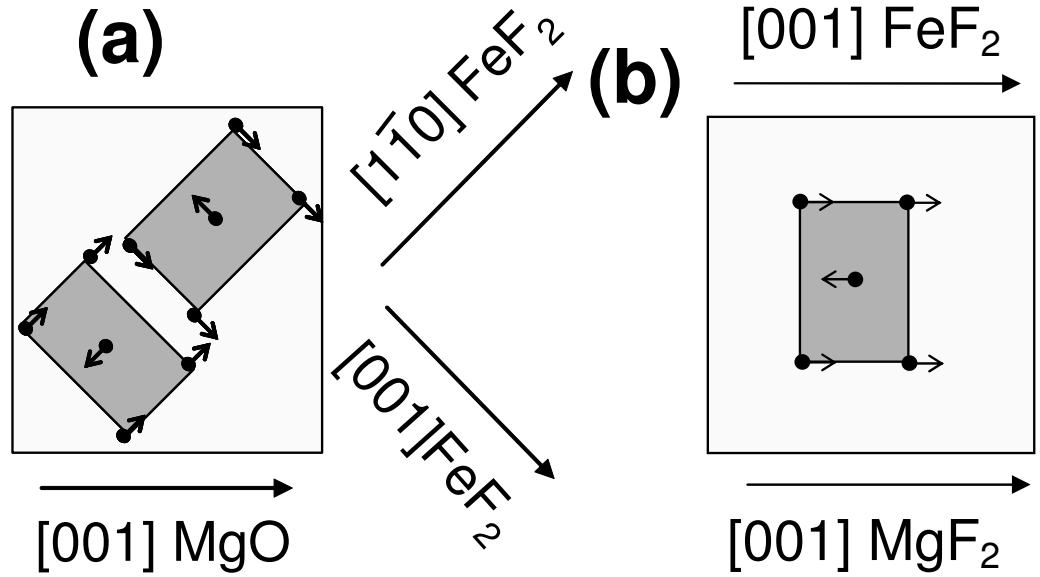

Figure I.3: Epitaxy relationship of FeF_2 on (a) MgO (100) and (b) MgF_2 (110) substrates. The big square in light gray and the small rectangle in dark gray refer to the substrate and the FeF_2 crystallite, respectively. Small black arrows on FeF_2 represent the orientation of Fe spins.

I.C Experimental Techniques

I.C.1 Sample Fabrication

Growth

FeF_2/FM thin films were grown on single crystal MgO (100) or MgF_2 (110) substrates measuring 10×10 mm^2 by electron-beam evaporation. First, the substrates were cleaned in methanol ultrasonic bath for 10 minutes. Sample holders were also cleaned in acetone and then methanol ultrasonic bath. Then, the substrates were mounted on the sample holder, and loaded into the evaporation chamber. The chamber was baked overnight and cooled down before the evaporation started. The base pressure was typically around 1-2$\times 10^{-7}$ Torr with liquid nitrogen cold trap. The substrate was first baked at 500°C for an hour. For MgF_2

substrates, after baking, O_2 with partial pressure 1×10^{-4} Torr was introduced in the chamber through a needle valve for 30 minutes with the substrate temperature still at 500°C to remove solvent residue on the substrate.

On MgF_2 substrates, FeF_2 was deposited at 300°C at a rate of 0.5 Å/s, and on MgO substrates, FeF_2 was deposited at 200°C at the same rate. The chamber pressure during FeF_2 growth was usually below 7×10^{-7} Torr. The FM was deposited at 150°C at the same rate of 0.5 Å/s, and the chamber pressure during deposition was around $1-3\times10^{-6}$ Torr. As a protection against oxidation, Al was deposited finally at a rate of 0.5-1 Å/s at 150°C. In certain occasions, 300 Å ZnF_2 was deposited before FeF_2 deposition as a buffer layer. ZnF_2 has lattice constants $a = b = 4.71$ Å and $c = 3.13$ Å, thus it reduces the lattice mismatch in c axis to 5%, and possibly causes less strain and fewer dislocations in FeF_2. ZnF_2 was deposited at 300°C at a rate of 0.5 Å/s, with 1×10^{-6} Torr deposition pressure.

Lithography

FeF_2/FM thin films were nanostructured by electron-beam lithography. Since the bilayer deposition needs to be grown at high temperatures, deposition through a mask of positive resist like PMMA followed by lift-off is not suitable for this purpose, and negative e-beam resist was chosen. Fig. I.4 shows the nanofabrication procedure. First, the sample was spin coated with negative e-beam resist at 4000 rpm for 60 seconds, and then baked in a convection oven for 30 minutes at 85°C. The thickness of the resist prepared in this way is about 100 nm, according to the factory specification. A small colloid droplet of 100 nm diameter gold particles was dropped at the corner and edge of the sample for focusing the electron beam. The sample was then loaded into the scanning electron microscope (SEM).

Circular dot arrays measuring 80×80 μm^2 were defined by electron beams at doses between 100 to 150 $\mu C/cm^2$ at 1000 times magnification. Dot sizes range from 100 to 600 nm, and the periodicity is nominally twice the dot diameter.

Usually 2 by 2 arrays were stitched together to minimize of the influence of sample or laser movement on magneto-optical Kerr effect measurement. Solid 80×80 μm^2 reference squares were also defined. After the sample was taken out of the SEM, it was post-baked in the convection oven at 85°C for 20 minutes. During post-baking, the developer was water-bathed at 22°C. To develop the resist, the sample was first dipped in the developer for 40 seconds, followed by rinsing in deionized water for 3 minutes. Then the sample was dried by N_2 gas, and the pattern was examined in an optical microscope.

After the e-beam lithography, exposed resist formed a mask for subsequent Ar^+ ion milling. The parameters for ion milling are, 3 kV acceleration voltage, 40 mA ionic current, and 20 mTorr pressure. Under this condition, the etching rate is about 10 Å/min for Fe, and it usually takes about 30 minutes to etch 40 Å aluminum (the top 20 Å is oxidized into ∼30 Å thick aluminum oxide). By controlling the ion-milling time, two different types of nanostructures can be prepared from the same bilayer sample: in type A, only the FM layer was nanostructured, while in type B both the FM and FeF_2 were nanostructured (Fig. I.5). In most cases in this thesis, type A samples were studied. Type B was studied to modify the spin configuration of FM dots by introducing more defects due to radiation damages. Nanodots were imaged by atomic force microscopy (AFM), and an example of dots of 300 nm diameter is shown in Fig. I.6.

I.C.2 Structural Characterization

The structural properties of FeF_2/FM bilayers were characterized by x-ray reflectivity, diffraction and scanning transmission electron microscopy (STEM). Low angle x-ray reflectivity gives the roughness and thickness of each individual layer, while high angle x-ray diffraction tells different crystalline orientations. By exploiting the electron energy loss spectroscopy (EELS), cross sectional STEM done at Oak Ridge National Lab by Dr. Maria Varela images different atomic layers from the substrate to the FM. Results from these characterization show

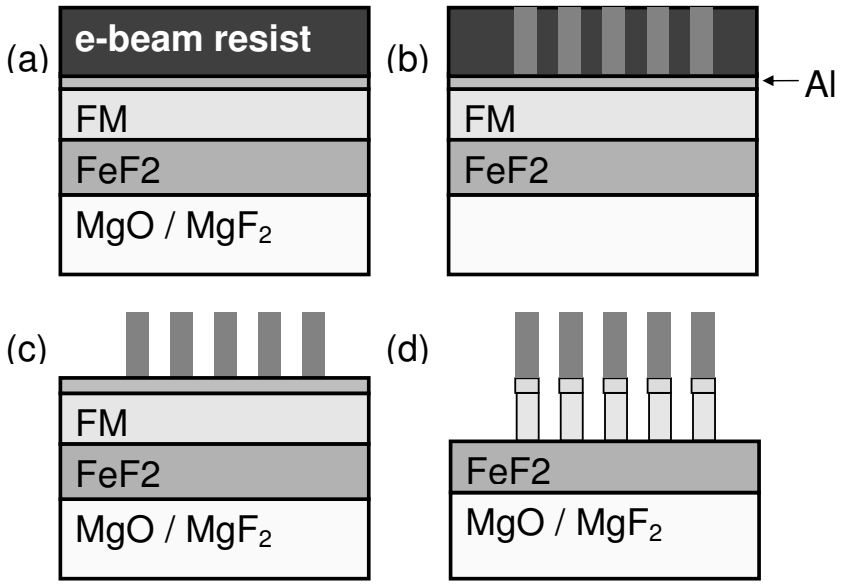

Figure I.4: Process to nanostructure the FM on top of a continuous FeF_2 layer. (a) Spin coating negative electron beam resist. (b) Electron beam lithography. (c) Developing the e-beam resist. (d) Argon Ion milling.

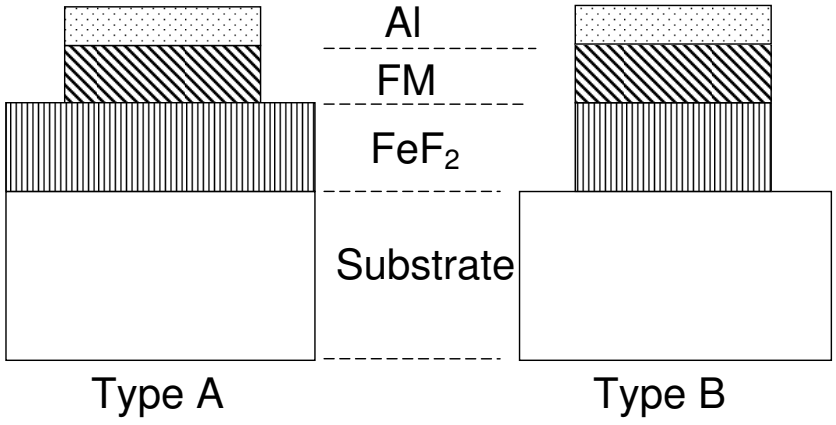

Figure I.5: Schematics of sample types A and B, where FeF_2 is either intact or etched.

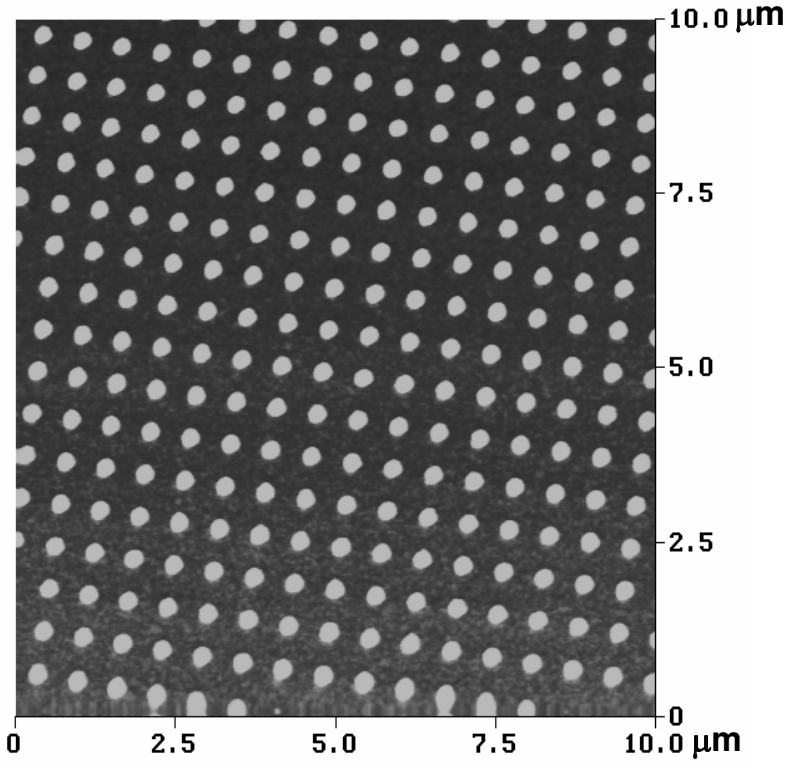

Figure I.6: AFM image of nanodots of 300 nm diameter, and 600 nm periodicity. The scale in the image is in the unit of micrometer.

that high quality epitaxial FeF_2 (110) layers were grown, and the FM layer is polycrystalline.

X-ray low angle reflectivity and high angle diffraction were performed on a two-axis x-ray diffractometer. After the sample was mounted, a θ-scan (rocking scan) was done with $2\theta = 1.0°$ to calibrate the θ offset, or the misalignment between the actual and system assumed sample normal. Below, I will take sample ZF37 as an example to illustrate the procedure. The nominal structure of this sample is MgF_2 / ZnF_2 (30 nm) / FeF_2 (30 nm) / Ni (3 nm) / Al (3 nm). The result from low angle calibration scan is shown in Fig. I.7. In this case, the center of the peak is at $\theta_c = 0.41°$, while it is supposed to be at $\theta_0 = 0.5°$, thus $\theta_{offset} = -0.09°$. Low angle reflectivity was measured with 2θ gradually increasing from 1° to 5°, with θ starting from $0.5 + \theta_{offset}$, which is 0.41° in this case. The reflectivity is then fitted with LSFIT program provided by Sunil Sinha's group based on optical reflection. Fig. I.8 (a) and (b) show the fitting to the reflectivity and its Fourier transform $|\int q_z^4 I(q_z) e^{iq_z z} dq_z|$, where q_z is the z component of the wave transfer vector, and $I(q_z)$ is the reflectivity. The thicknesses of ZnF_2, FeF_2, Ni, and Al are 254, 415, 21, and 20 Å, respectively. The roughnesses of the substrate and the layers above are 0.9, 5.7, 12, 14, and 10 Å, respectively.

Before starting x-ray diffraction, the substrate rocking scan was performed to recalibrate θ_{offset}. First, a fast $\theta - 2\theta$ scan with 2θ between 26° to 28.5° was performed around the substrate MgF_2 (110) peak at $2\theta = 27.3°$ for Cu Kα line, as shown in Fig. I.9 (a). The substrate (110) peak consists of two peaks of similar magnitudes at $2\theta = 27.32°$ and 27.39°, with $\Delta 2\theta = 0.07°$. This may be due to different wavelengths of Cu Kα1 and Kα2 lines, 1.540563 and 1.544390 Å, respectively [64] or structural defects like facets. Considering the Bragg condition $2d \sin\theta = \lambda$, for small wavelength variation, we have $2d \cos\theta \Delta\theta = \Delta\lambda$, thus, $\Delta\theta = \Delta\lambda / \lambda \tan\theta$. This gives $\Delta\theta = 0.035°$, same as the observed difference. Therefore, the double peak feature is due to the dual wavelengths of the x-ray source. Here, we fit the peaks with a single Gaussian function, and fix 2θ at $2\theta_c = 27.34°$

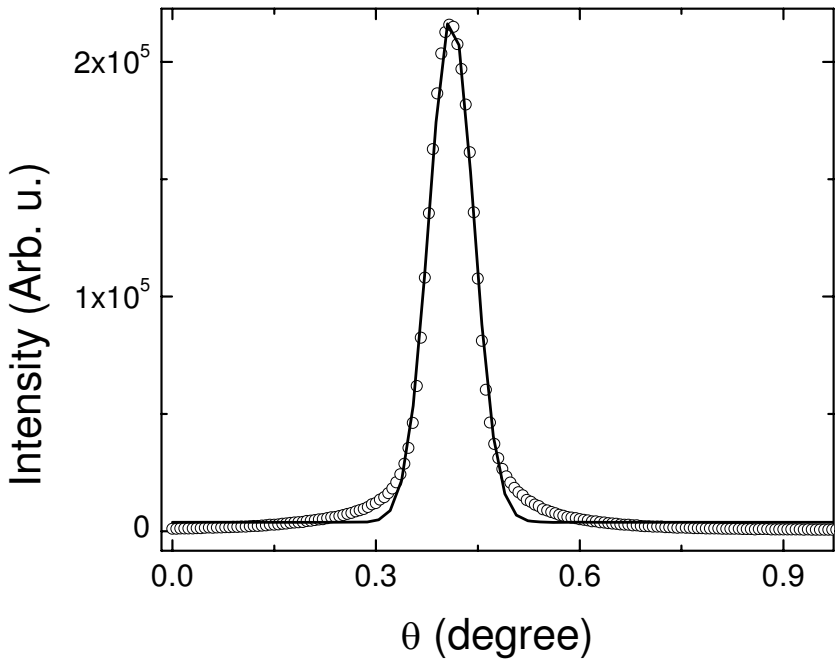

Figure I.7: θ-scan to align the sample normal with $2\theta = 1.0°$. The open circle and line are the experimental data and the fit to a Gaussian function, respectively. From the fit, the center of the peak was found to be at 0.41°.

for substrate rocking scan (Fig. I.9 (b)). The full width half maximum (FWHM) is 0.22°, and the center is at 13.58°. If there is no misalignment, it should center at $\theta = 13.67°$, therefore, $\theta_{offset} = -0.09°$, similar to what was found earlier in low-angle alignment scan. Using θ_{offset}, x-ray diffraction is performed with 2θ scanning from 20° to 70° (Fig. I.10 (a)).

MgF_2 (110) (220), FeF_2 and ZnF_2 (110) (220) can be identified. Substrate impurity peaks were also found. Since FeF_2 and ZnF_2 have very similar lattice parameters (0.024° different in their (110) peak positions)(Table A.1), we were not able to distinguish their crystalline peaks from each other. Their (110) peak centers at $2\theta = 26.82°$. Rocking scan was performed around this 2θ value (Fig. I.11). One can clearly see two distinct peaks, a sharp one and a broad one overlaid on top of each other. Fitting this curve with two Gaussian functions gives their widths being 0.16° and 1.13°, respectively. We attribute the broad one to diffuse scattering at the interface, which is also present in rocking scans around a low angle specular

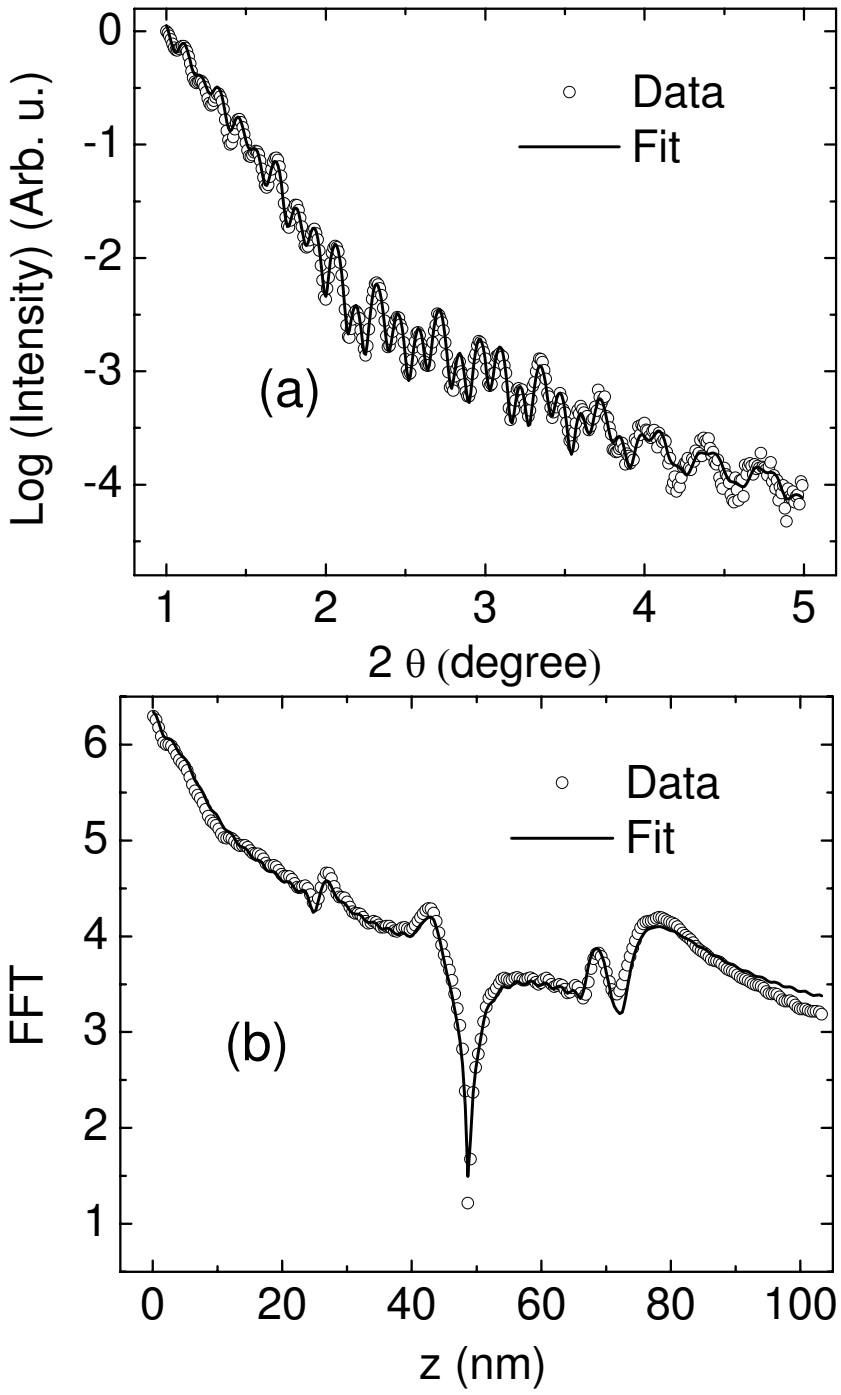

Figure I.8: (a) Normalized low angle x-ray reflectivity (open cirle) measured with 2θ scanning from 1° to 5°. The line is a fit to the experimental result based on the optical model. (b) Fast Fourier transform (FFT) of the reflectivity $|\int q_z^4 I(q_z) e^{iq_z z} dq_z|$ from the experiment (open circle) and the fit (line).

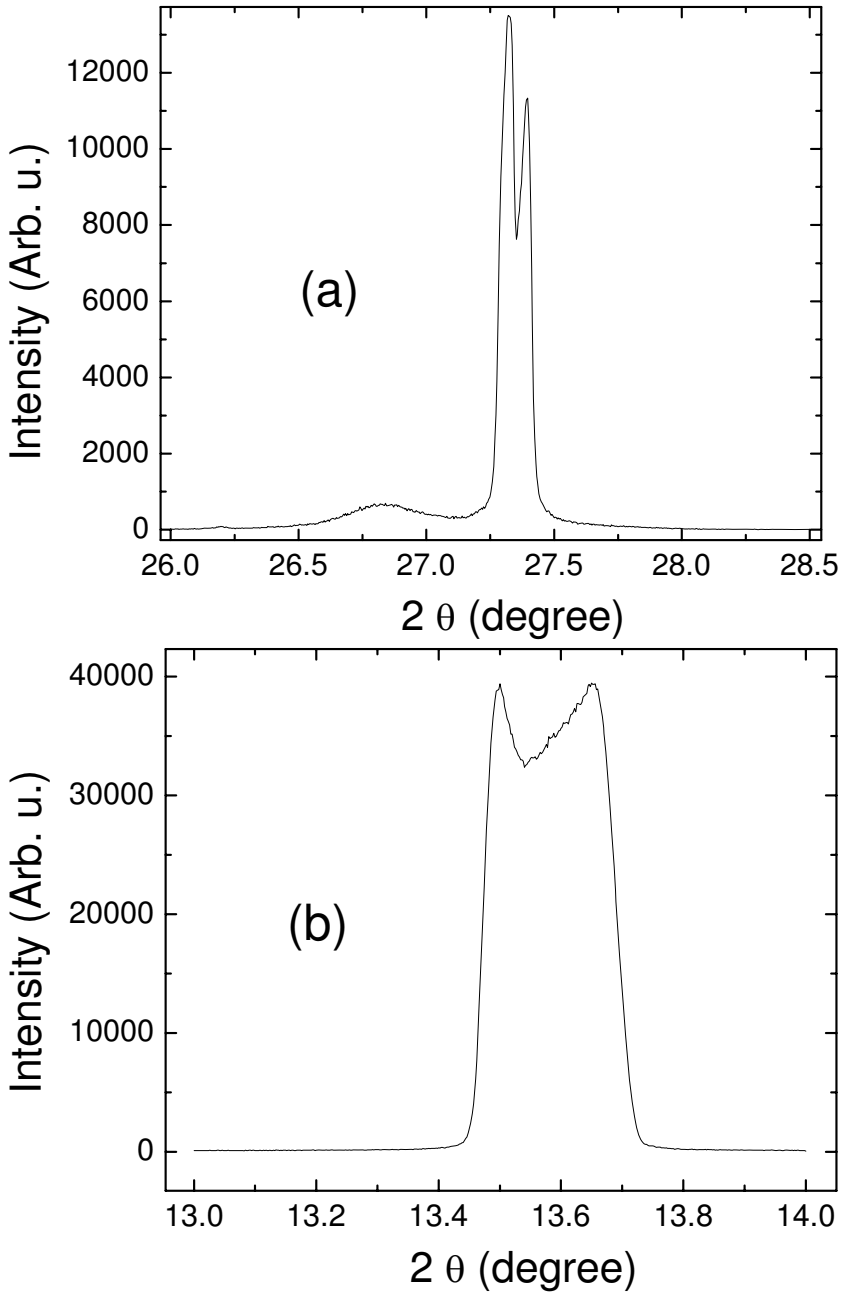

Figure I.9: (a) A fast $\theta-2\theta$ coupled scan across the MgF_2 (110) peak at $2\theta = 27.34°$. The small peak on the left of the main MgF_2 (110) peak is from FeF_2 and ZnF_2 (110) at $2\theta \approx 26.83°$. (b) MgF_2 substrate rocking scan around MgF_2 (110) peak with $2\theta = 27.34°$.

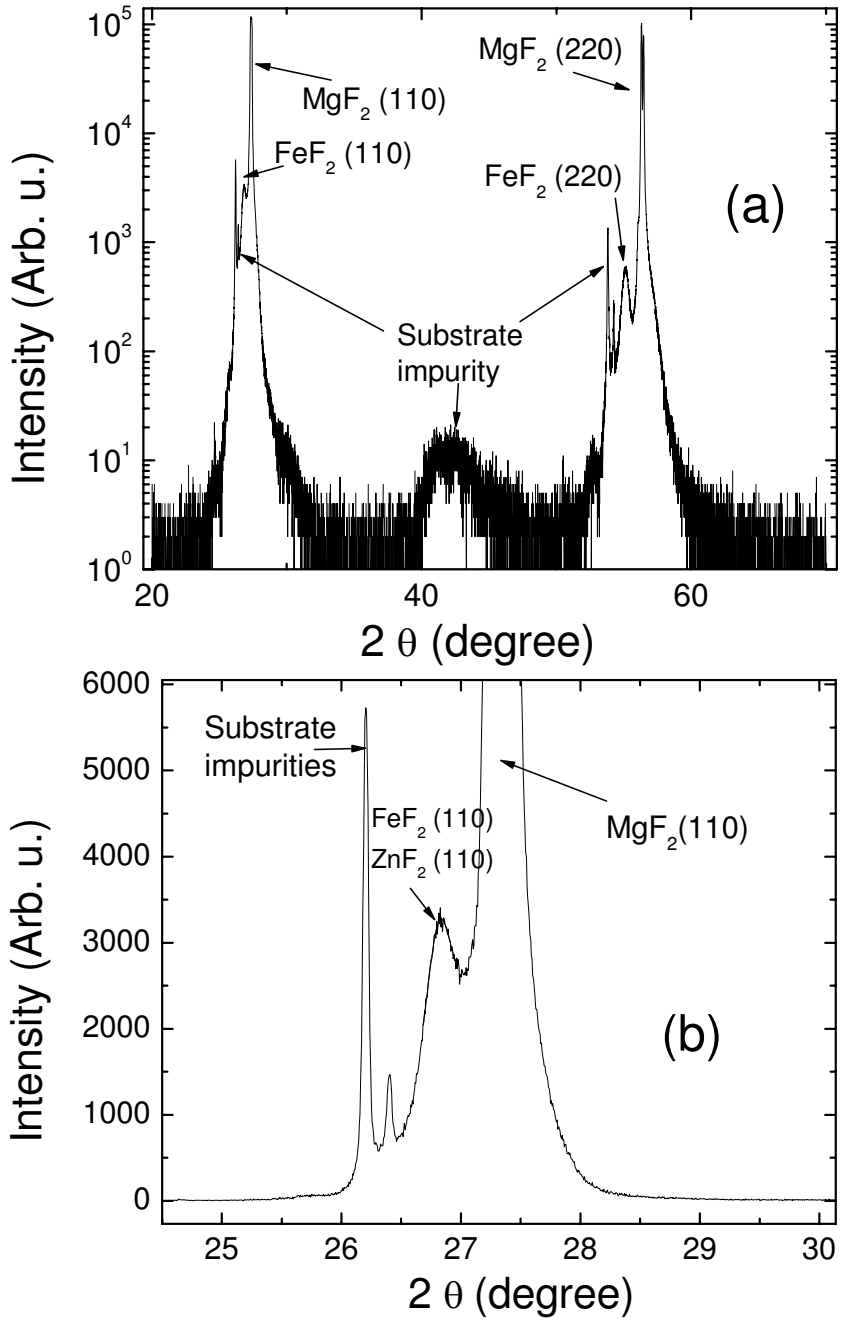

Figure I.10: (a) High angle x-ray diffraction with 2θ scanning from 20° to 70°. (b) Zoom-in around MgF_2 (110) peak.

(Fig. I.7). The narrow one is from the angular dispersion of FeF_2 (110) orientation. The width 0.16° measured here is limited by the slit size. Using a narrow slit, we found the width is as small as 0.04°. Compared with what was found before in twinned FeF_2 on MgO substrates, where the FWHM of rocking scan around FeF_2 (110) is about 2-4°, untwinned FeF_2 clearly has much higher crystalline quality. This was confirmed by cross sectional STEM imaging on samples with the same nominal structure FeF_2 (50 nm) / Co (4 nm) / Al (2.5 nm) on MgO and MgF_2 substrates.

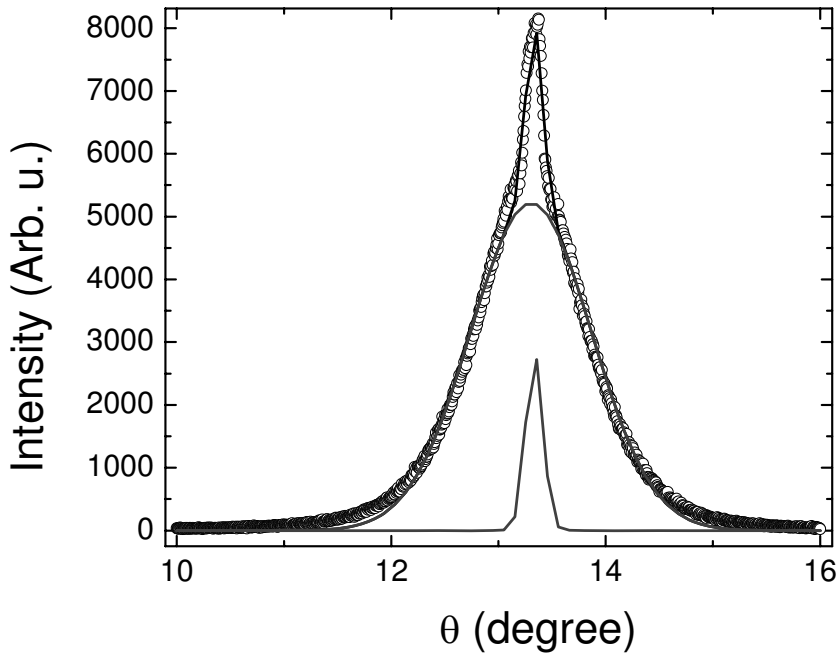

Figure I.11: Rocking scan (black) around FeF_2 and ZnF_2 (110) peak $2\theta = 26.82°$. It is fitted with two Gaussian functions plotted in light gray.

From Fig. I.12, one can see that FeF_2 grows epitaxially on MgF_2 substrates, with high crystalline quality. Atomic planes formed with very high regularity, and can be clearly identified. No granularity was observed. Major defects observed may be anti-phase boundaries or low angle grain boundaries (like the one marked with green arrows) that originate from the interface with the substrate. The thin Co layer is polycrystalline, but seems discontinuous. Fig. I.13 (a) and (b) show high resolution image of FeF_2 close to its interface with Co and MgF_2

substrate, respectively. Highly regular FeF_2 atomic planes were found near both interfaces. High energy electrons can result in radiation damage on fluoride, which can be seen in regions circled in Fig. I.13 (b). When FeF_2 was grown on a MgO substrate, although FeF_2 is also epitaxial, its crystalline quality is much worse than that on MgF_2 substrates (Fig. I.14). Therefore, untwinned FeF_2 on MgF_2 substrates has a much longer structural modulation length scale than its twinned counterpart on MgO substrates. This difference has significant implications in its magnetic behavior when coupled with the FM, and will be addressed in Chapter II.

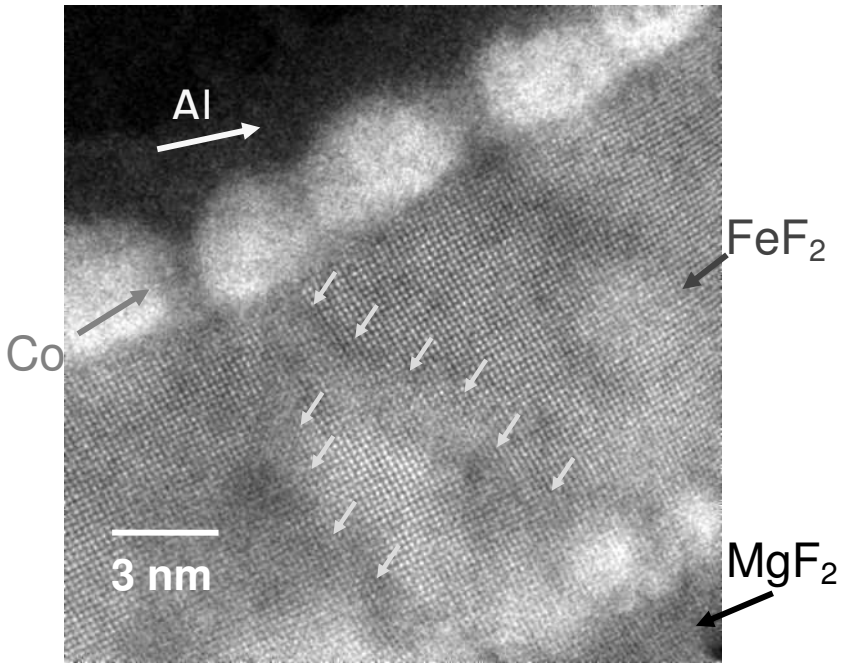

Figure I.12: STEM image of FeF_2/Co/Al grown on a MgF_2 substrate. Gray arrows mark the defects in the FeF_2 layer.

I.C.3 Magnetic Characterization

Magnetic properties of the samples were mainly characterized by superconducting quantum interference device (SQUID) and magneto-optical Kerr effect (MOKE). We also collaborated with Kai Liu's group at University of California, Davis, to characterize the samples' reversal mechanism with vector vibrating sample magnetometry (VSM), with Sunil Sinha's group at University of California,

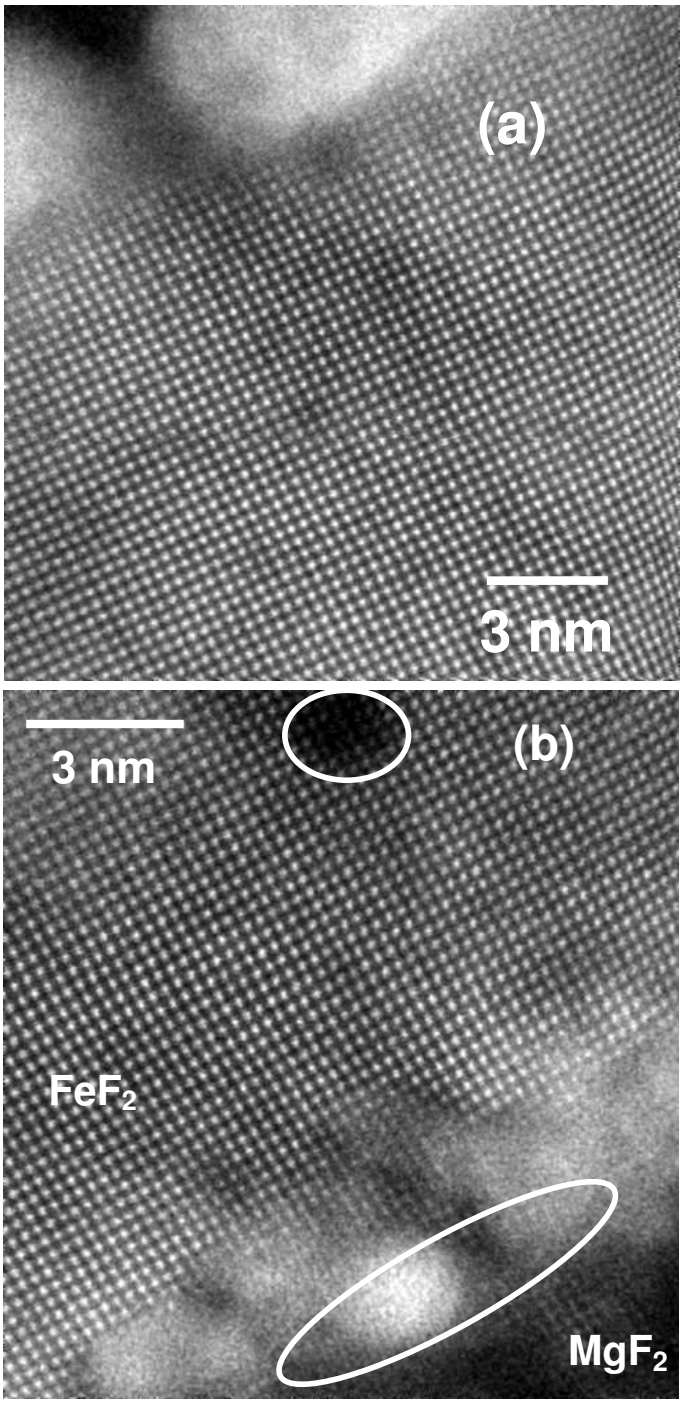

Figure I.13: High resolution STEM image at (a) Co/FeF_2 and (b) FeF_2/MgF_2 interfaces, on the same sample as in Fig. I.12. The two circles highlight the radiation damage to FeF_2 and MgF_2.

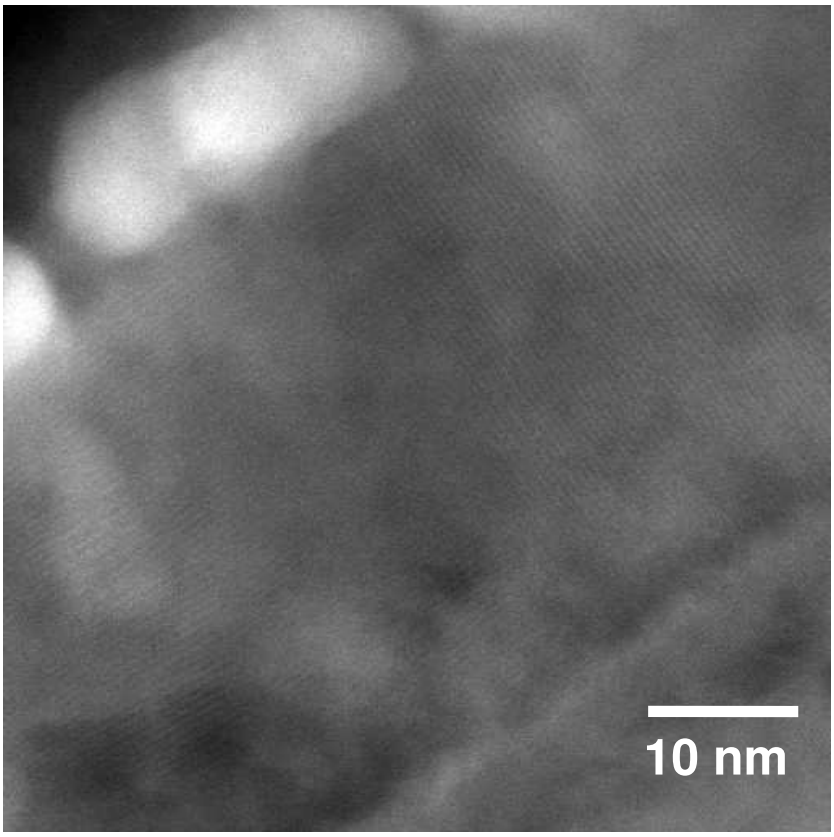

Figure I.14: STEM image of FeF_2/Co/Al grown on a MgO substrate. From top to bottom, different layers are Co, FeF_2 and MgF_2, respectively.

San Diego, and Mike Fitzsimmons at Los Alamos National Laboratory to study the magnetic depth profile with resonant x-ray scattering and neutron scattering. Experiments were also performed at Advanced Light Source of Lawrence Berkeley National Lab in collaboration with Elke Arenholz using element-specific x-ray magnetic circular dichroism (XMCD) measuring total electron yield (TEY). Below I will focus on the home-made low temperature (4.2 - 300 K) high magnetic field (up to 7 T) magneto-optical Kerr effect (MOKE) setup.

Magneto-optical Kerr effect exploits the anisotropy in the reflection material induced by its magnetic moments, which interact with the incoming light, and rotate its polarization as it is reflected [65, 66]. There are three different Kerr effect geometries (Fig. I.15). The first is polar Kerr effect, which is sensitive to the magnetic moment perpendicular to the sample plane. This effect is most pronounced for normal incidence. The second is longitudinal Kerr effect, where the moment is in the sample plane parallel to the plane of reflection. For both polar and longitudinal MOKE, the Kerr rotation is proportional to the magnitude of the magnetic moment. The last is transverse MOKE, which is sensitive to the moment perpendicular to the plane of reflection in the sample plane. Different from the previous two, in transverse MOKE, the polarization of the reflected beam does not change. Instead, the reflectivity of p polarized light changes by an amount proportional to the the transverse moment. Here p and s polarization refers to the polarization with $\mathbf{E}$ vector parallel or perpendicular to the plane of reflection, respectively. Note that these three Kerr effects are not defined by how the sample is oriented, but by the orientation of the relevant magnetization. In general, these three effects are coexistent, when the sample magnetic moment is arbitrarily oriented. In our case, due to the limitation imposed by the cryostat geometry, the magnetic field and sample easy axis are parallel to each other in the plane of reflection. Since the magnetic moment is mostly along the field direction with a relatively sharp magnetization reversal (Fig. I.16), longitudinal MOKE is dominant, while in certain geometry transverse MOKE can be observed as well.

Fig. I.16 shows the setup of our MOKE system. The light source is an intensity stabilized HeNe laser, whose wavelength is $\lambda = 632.8$ nm. The laser intensity chopped into a square wave for later detection by a lock-in amplifier. Then, the laser beam diameter is enlarged by 10 times through a beam expander. The purpose of beam expansion is to reduce the beam size when it is focused by a lens on the sample, since the focal point size is inversely proportional to the incident beam diameter before the lens. Next it passes through a Glan-Thompson polarizer, which is also a beam splitter. It is set up in the way so that the outgoing beam is in p polarization. Then it passes through a quarter wave-plate and a lens, and is focused on the sample. The quarter wave-plate compensates the induced ellipticity due to non-perfect optical elements and Kerr effect. On the sample holder inside the cryostat, there are two small mirrors, one of which deflects the incoming beam onto the sample and the other reflects the beam out of the cryostat, so that the angle of incidence on the sample is between 45 to 55 degree, close to the Brewster angle of the substrate (MgO or MgF_2). This reduces the background signal from substrate reflection when measuring exchange biased nanodots. After the beam leaves the cryostat, it is collimated by a lens and then passes through a half wave-plate. The half wave-plate rotates the polarization of the laser beam by 45°, so that the s and p components have similar intensities. Then a Glan-Thompson polarization beam splitter splits the beam into s and p polarization and directs them into two photo diodes. The voltage from the two diodes is fed into a differential pre-amplifier. The difference signal, amplified by 1000 to 5000 times, is then sent to a lock-in amplifier. The amplifier locks at the chopper frequency, measures the difference signal between the two photo diodes, and sends the data to a computer. Before the measurement is started, the half wave-plate is adjusted so that the intensity difference between the two polarizations is the zero. During the measurement, as the magnetic moment changes with magnetic field, the polarization of the reflected laser beam rotates, and results in a small intensity imbalance between the two polarizations, proportional to the Kerr rotation angle.

In this way, the small angular change is transformed into small intensity difference, which can be easily measured. Below, a brief analytical description of this setup is given to show what we measured was indeed the longitudinal magnetic moment.

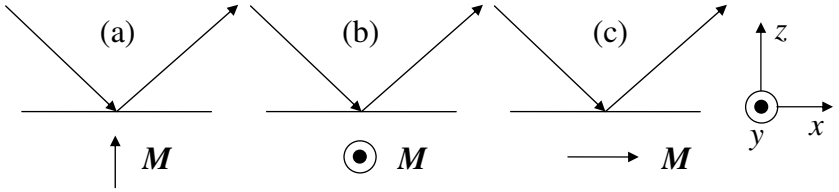

Figure I.15: Schematics of (a) polar Kerr effect, (b) transverse Kerr effect, and (c) longitudinal Kerr effect.

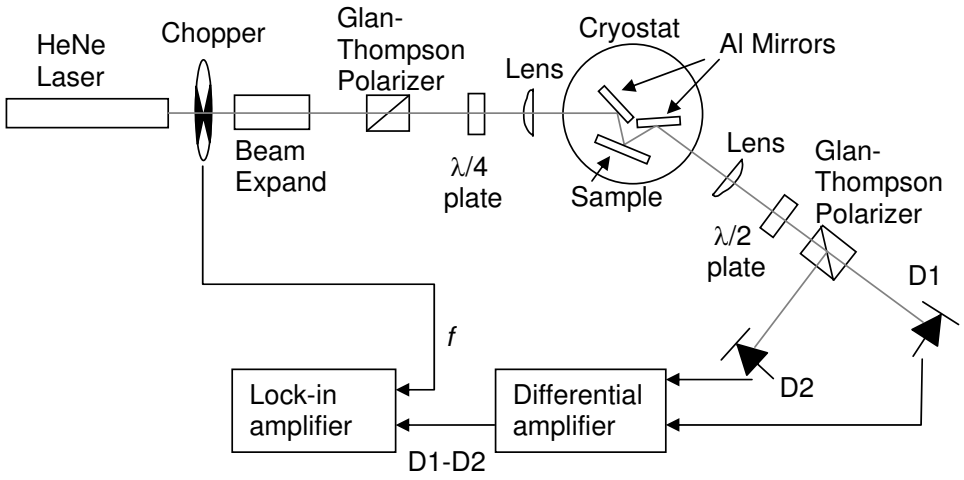

Figure I.16: Schematics of the home-made low-temperature, high-field MOKE setup.

From Ref. [67], we have the follow reflectivity matrix,

$$\begin{pmatrix} E_p^r \\ E_s^r \end{pmatrix} = \mathbf{R} \begin{pmatrix} E_p^i \\ E_s^i \end{pmatrix} = \begin{pmatrix} r_{pp} & r_{ps} \\ r_{sp} & r_{ss} \end{pmatrix} \begin{pmatrix} E_p^i \\ E_s^i \end{pmatrix}, \text{ where}$$

$$r_{pp} = \frac{\mu_1 N_2 \cos\theta_1 - \mu_2 N_1 \cos\theta_2}{\mu_1 N_2 \cos\theta_1 + \mu_2 N_1 \cos\theta_2} + \frac{2i\mu_1\mu_2 N_1 N_2 \cos\theta_1 \sin\theta_2 m_y Q}{\mu_1 N_2 \cos\theta_1 + \mu_2 N_1 \cos\theta_2} \quad \text{(I.1)}$$

$$r_{ps} = -\frac{i\mu_1\mu_2 N_1 N_2 \cos\theta_1 (m_x \sin\theta_2 + m_z \cos\theta_2) Q}{(\mu_1 N_2 \cos\theta_1 + \mu_2 N_1 \cos\theta_2)(\mu_2 N_1 \cos\theta_1 + \mu_1 N_2 \cos\theta_2)} \quad \text{(I.2)}$$

$$r_{ss} = \frac{\mu_2 N_1 \cos\theta_1 - \mu_1 N_2 \cos\theta_2}{\mu_2 N_1 \cos\theta_1 + \mu_1 N_2 \cos\theta_2} \quad \text{(I.3)}$$

$$r_{sp} = \frac{i\mu_1\mu_2 N_1 N_2 \cos\theta_1 (m_x \sin\theta_2 + m_z \cos\theta_2) Q}{(\mu_1 N_2 \cos\theta_1 + \mu_2 N_1 \cos\theta_2)(\mu_2 N_1 \cos\theta_1 + \mu_1 N_2 \cos\theta_2)} \quad \text{(I.4)}$$

Here, E_p^i, E_s^i are the p and s component of the electric field vector of the incident beam, and (E_p^r, E_s^r) is the vector of the reflected beam. Subscripts 1 and 2 refer to air and the magnetic media, respectively. μ is the magnetic susceptibility, and is assumed to be 1 for all later discussion. N is the index of refraction. θ_1 and θ_2 are the angles of incidence and refraction with respect to the sample normal, and follow Snell's law $N_1 \sin\theta_1 = N_2 \sin\theta_2$. m_x, m_y, and m_z are the three components of the unitless magnetic moment normalized by the total magnetic moment, using the coordinate system in Fig. I.15. Q is the complex magneto-optical constant. For bulk Fe, $N_2 = 2.85 + 3.36i$, and $Q = 0.0215e^{-i0.073}$ [68, 69]. From the above formula, one can clearly see that $s - s$ (s polarizer and s analyzer) configuration does not yield any magnetic information (Equation I.3), while $p - p$ configuration gives an intensity change proportional to the transverse magnetization m_y (Equation I.1). This shows that p and s polarizations are not symmetric. A cross configuration ($s - p$ or $p - s$) contains both longitudinal and polar magnetic moments (Equations I.2 and I.4). This is consistent with the general belief that longitudinal and polar Kerr effects yield a rotation of the polarization plane, while transverse Kerr effect yields a reflectivity change in p polarization. For our geometry, it becomes less obvious which components are relevant. Due to the thin film nature of our samples, m_z is negligible here, but the transverse component m_y can become significant during reversal, and cannot be ignored.

In the following evaluation, we assume 45° incidence, and use bulk Fe magneto-optical constants for magnetic media 2. For p incidence, after rotating

the polarization of the reflected beam by 45° followed by beam splitting, straightforward calculation gives the intensity difference, $1.8 \times 10^{-3} I_0(m_x + 0.01 m_x m_y)$, where I_0 is the incident beam intensity. Considering the usually small transverse moment m_y, the intensity difference is dominated by longitudinal component m_x. When the incident beam is s polarized, the intensity difference is $-2.2 \times 10^{-3} I_0 m_x$. It is not surprising to find no transverse term m_y for s incident polarization, since m_y is only associated with p polarized light (see Equation I.1). Practically, the only significant difference between s and p polarization of incidence is the change of sign. If one rotates the incident polarization to 45° with respect to p or s polarization plane, and the half wave-plate accordingly (about 3° adjustment), the intensity difference between two polarizations is $6 \times 10^{-3} I_0(m_y + 0.03 m_x)$, dominated by the transverse component m_y. Since the longitudinal component is usually much larger than the transverse component, the second term may be still visible, but can be easily subtracted. The robustness of these three geometries against misalignment of incident polarization is also tested. Misalignment smaller than 3° does not yield any significant changes. Therefore, the above calculation proves our MOKE setup is capable of measuring both longitudinal and transverse magnetic moment. A typical measurement result from a FeF_2/Fe unpatterned thin film is shown below in Fig. I.17.

I.D Simulation Techniques

Micromagnetics is a very useful simulation technique for studying submicron magnetic structures. The idea of micromagnetics is to discretize a magnetic geometry into small cells, each of which can be regarded as a macrospin, and then let these spins evolve in an effective field H_{eff} according to Landau-Lifschitz-Gilbert (LLG) equation. The LLG equation is as follows [70],

$$\frac{d\mathbf{M}}{dt} = -|\gamma| \mathbf{M} \times \mathbf{H}_{eff} + \frac{\alpha}{M_S} (\mathbf{M} \times \frac{d\mathbf{M}}{dt}),$$

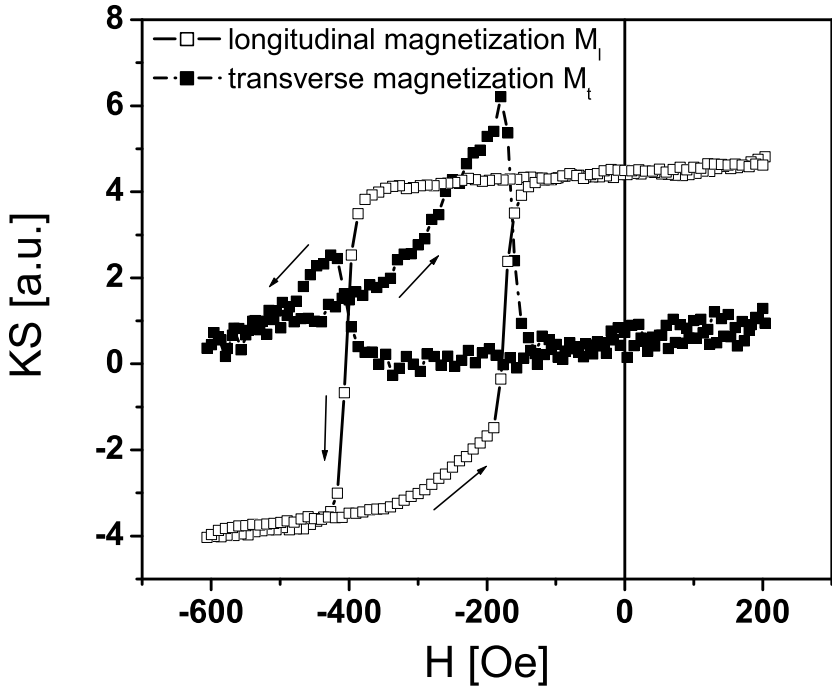

Figure I.17: Kerr effect signal (KS) of longitudinal M_l (open symbols) and transverse M_t magnetization as a function of magnetic field H (closed symbols) measured on a Fe/FeF_2 thin film at 10 K after field cooling in 2 kOe magnetic field.

where $\mathbf{M}$ is the magnetization, $\mathbf{H}_{eff}$ is the effective field, γ is the Gilbert gyromagnetic ratio, α is the damping constant, and M_S is the saturation magnetization. Here, the effective field $\mathbf{H}_{eff}$ is defined as [70],

$$\mathbf{H}_{eff} = -\frac{\partial E}{\mu_0 \partial \mathbf{M}},$$

where the energy density E is a function of $\mathbf{M}$ specified by Brown's equations [71], including anisotropy, exchange, dipolar, applied field (Zeeman) terms, and in case of EB, interfacial coupling term. Brown's equations describe the equilibrium condition of the spin configuration as follows,

$$\begin{cases} \mu_0 M_s \mathbf{m} \times \mathbf{H}_{eff} = 0 \\ \frac{\partial \mathbf{m}}{\partial \mathbf{n}}|_{\partial\Omega} = 0 \end{cases},$$

where $\mathbf{m}$ is the local vector magnetic moment, with $\mathbf{n}$ being its unit vector.

OOMMF package developed by M. J. Donahue and R. D. McMichael at NIST provides an easy and flexible access to micromagnetic simulation [70]. There are two main solvers, mmSolve2D for 2D structures, and Oxsii for 3D simulation. mmSolve2D was used to simulate magnetic nanodots with diameters ranging from 100 nm to 600 nm, and thicknesses from 10 nm to 60 nm. We found magnetization reversal through either vortex or multi-domain state for dot sizes in this range.

To simulate exchange biased thin film or nanostructures, it is necessary to use Oxsii, and do a full 3-dimensional simulation that includes the coupling at the interface. It is not conceptually straightforward to simulate an AF, since micromagnetics is based on continuum theory, and does not allow drastic changes from one cell to another. Here, instead of directly simulating the AF, we emulate the effect of the AF on the FM with a single layer of pinned moments, which is exchange coupled to the bottom discretization layer of the FM (Fig. I.18). Therefore, the interfacial coupling Hamiltonian is $\mathcal{H}_{Int} = -J_{FM/AF} \sum_{i \in \{Interface\}} \vec{m}_i \cdot \vec{\sigma}_i$, where $J_{FM/AF}$ is the interfacial exchange constant, $\vec{m}_i$ is the FM moment in cell i, and $\vec{\sigma}_i$ is the interfacial pinned AF moments. This coupling is equivalent to

an effective magnetic field applied to the bottom FM layer. In OOMMF, this is implemented as a spatially variant *StageZeeman* term [70]. $J_{FM/AF}$ is adjustable usually around $J_{AF} = -0.45$ meV up to $2J_{AF}$ [61]. We introduced AF grains of average size 25×25 nm^2 to simulate the inhomogeneous interfacial coupling[72]. $\sigma_i = -\alpha_i S_i^{AF} p_j$ with $S_i^{AF} = 2$, consists of two random quantities: α_i denoting the *intergrain* variation, and p_j the *intragrain* variation. α_i varies as 1±0.35 between grains, while p_j varies as (10±3)% between cells. This 10% assumption is based on recent experiments which found net frozen AF interfacial moments with about 4% [37] to 7% [38] coverage that contribute to EB. Crucial parameters for the simulation include the product of the uncompensated moment coverage and interfacial coupling, and intergrain fluctuation. The former defines the effective coupling strength. The latter describes the interfacial inhomogeneity modulated over a length scale of the grain size (25 nm), comparable with the FM domain wall width 82 nm. This spatial modulation of σ_i leads to an inhomogeneous pinning on the FM, and is essential to explain reversal process revealed in the experiment. However, the intensity of the modulation is not essential: 20% to 50% standard deviation in α_i gives similar results. The resultant spatial variation of σ_i is shown in the inset of Figure I.19. With the addition of this interfacial coupling term, exchange bias effect can be simulated, and the result is in qualitative agreement with the experimental result (Sections II.F and III.H). In some model systems, even quantative agreement was found (Section III.B).

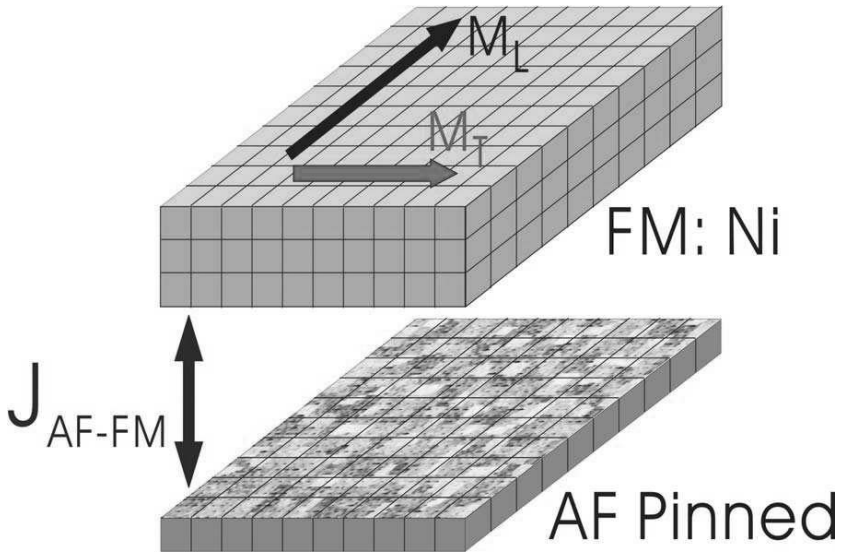

Figure I.18: Schematics of the implementation of EB effect in micromagnetic simulation. Here, M_L and M_T are longitudinal and transverse magnetization of the FM, with longitudinal orientation defined as the applied field direction. The color contrast in the AF pinning layer denotes the areal density of pinned moments

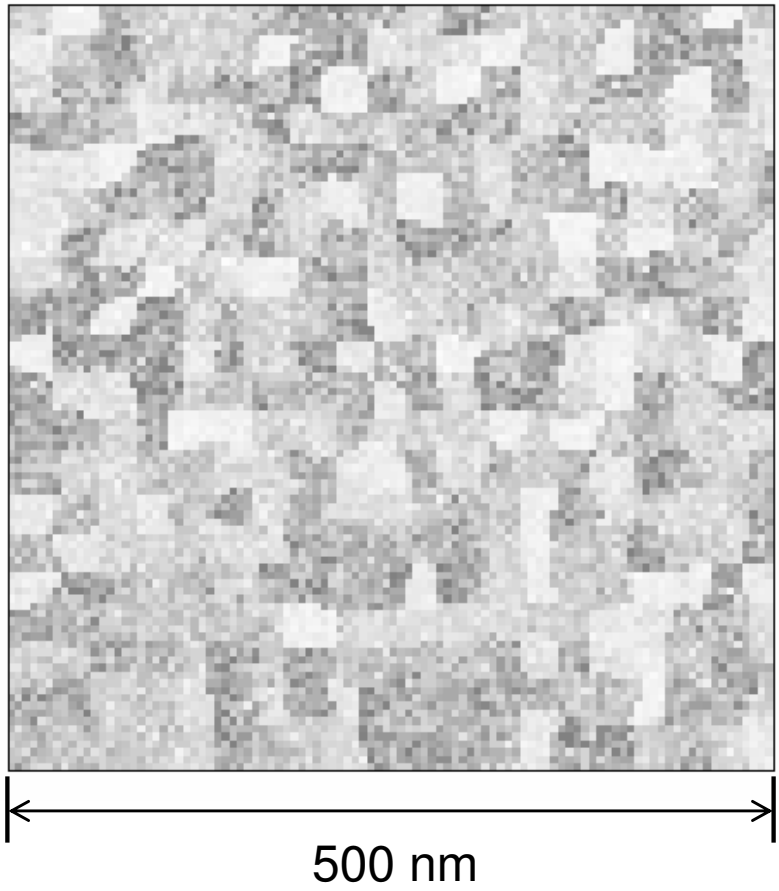

Figure I.19: Pinned interfacial AF moments that are coupled to the bottom FM discretization layer that measures 500×500 nm^2. The areal density of AF moments is color coded in gray scale, so that black and white correspond to maximum and zero uncompensated pinned AF moments, respectively.

II

Lateral Length Scale Relevance

II.A Introduction

Understanding the relevant length scales that characterize a particular phenomenon or type of interaction in a material is one of the most important issues in physics. This becomes less obvious and more intriguing when two dissimilar materials are in contact. In this chapter, the *lateral* length scale relevance in exchange bias (EB) is discussed.

In exchange bias, when the FM and AF interact with each other through exchange coupling across the interface, the relevance of different length scales in the FM and AF can give rise to a rich variety of phenomenon. In a FM, the most important length scale is its domain wall width. For a Bloch wall, the domain wall width is described by $\delta_{DW} = \pi\sqrt{A/K}$, where A and K are the stiffness and uniaxial anisotropy of the FM, respectively. In a single crystal Ni, for example, $\delta_{DW} \approx 82$ nm, and for Co, $\delta_{DW} \approx 14$ nm [73]. In an AF, the domain wall width can be similarly defined. However, since the anisotropy of FeF_2 is much bigger than that of the FM, with $K = 1.35 \times 10^4$ kJ/m^3, its domain wall width $\delta_{DW} = 0.95$ nm is much smaller than that of Ni or Co, thus becoming irrelevant in its coupling with the FM. We found that a more important length scale in FeF_2 is the AF "domain" size defined by the sign of the uncompensated moments, thus the sign of H_{EB}. It is

important to note that this "domain" is not the same as, and may be irrelevant with AF domains conventionally defined in terms of the AF order parameter, staggered magnetization. For the following description, quotation marks will be omitted for convenience, but it should not be confused with the conventionally defined concept of domains.

We believe that this AF domain size is related to the AF crystalline grain size. As we mentioned earlier, FeF_2 grows epitaxially twinned on MgO (100) substrates, and untwinned on MgF_2 (110) substrates. Twinned FeF_2 was found to have mosaicity grains of about 5-10 nm, while untwinned FeF_2 has a grain size about 28 nm. Due to the presence of twinning and worse crystalline quality on MgO compared with MgF_2 substrates, AF domains are more likely to be limited on a single grain, or a few grains. However, AF domains on untwinned FeF_2 can span over many grains, and the domain size can become much larger than its twinned counterpart. This hypothesis was confirmed experimentally in accordance with micromagnetic simulation.

When the FM is nanostructured, another FM length scale is introduced, the lateral size of the FM element. Nanostructures have been generally used to probe the importance of the FM and AF domain sizes, and test the validity of different models. Both enhancement and suppression of H_{EB} were found in the literature, and explained mainly in terms of the spin counting fluctuations, and related to the AF grain size [7, 74, 75, 41, 44, 76, 77]. Recently, it was found that the enhancement or suppression of H_{EB} can be tailored by varying the AF thickness [77]. This effect is ascribed to the limitation of AF domain size imposed the FM dot sizes, and the concomitant weakening of the pinning strength exerted by the AF during magnetization reversal of the FM.

In this chapter, I will discuss about how the length scale relevance drastically modifies the magnetization reversal behavior and especially the cooling field H_{FC} dependence of H_{EB}. We found two distinct types of transitions from negative (small H_{FC}) to positive (large H_{FC}) EB for an intermediate H_{FC}: for twinned

FeF_2, a continuous transition of H_{EB} was found, while coexistence of EB of both signs was observed for untwinned FeF_2 (Section II.B). Similar double hysteresis loops are also found when cooling down the sample in zero field and remanent state (Section II.C). In this case, using spatially resolved magneto-optical Kerr effect (MOKE), we found that sample indeed broke down into positive and negative biased regions, and confirmed that double hysteresis loops formed when cooling a magnetically saturated sample in an intermediate H_{FC} are also due to the AF breaking into domains. This result was further corroborated by vector magnetometry (Section II.D). We attribute this contrast between single vs. double hysteresis loops to the relevance of the FM domain wall width and AF domain size. For an intermediate H_{FC}, uncompensated AF moments form domains orienting either along or against H_{FC}. Due to the higher crystalline quality and absence of twinning in FeF_2 on MgF_2 substrates, these AF domains are also larger. Micromagnetic simulations show that when the AF domain size is much larger than the FM domain wall width, FM moments on each AF domain behave independently, thus allowing hysteresis of positive and negative EB to coexist (Section II.F). When the domain is much smaller, a single hysteresis with an averaged H_{EB} is shown. To probe the domain size, the FM was patterned into nanostructures ($\sim$100 nm) (Section II.E). The onset H_{FC} for positive EB significantly decreases with decreasing FM dot sizes. This is attributed to the importance of the FM dot sizes compared with the AF domain size ($\sim$500nm).

II.B Bi-domain State Established by Intermediate Field Cooling

Although singly shifted hysteresis loop was most widely observed in EB experiments, in several cases double-hysteresis loops were also reported. They were attributed to a coexistence of oppositely oriented interfacial AF moments in different mesoscopic regions. However, the way to prepare this state and hence

the underlying mechanisms involved can be very different. In several cases this coexistence was found after zero field cooling (ZFC) a demagnetized sample [56, 78, 24, 57]. Here the FM domain configuration was imprinted in the AF during cooling. In rare cases double loops were found after field cooling (FC) at intermediate fields [57, 79, 80]. Double hysteresis loops are also reported in measurements along the hard axis of the AF, which was attributed to an additional biquadratic AF-FM interaction [81, 82, 35]. In this section, I present a systematic and tunable shift from negative to double, and finally to positive EB in an AF/FM bilayer, FeF_2/Ni, with increasing cooling fields.

FeF_2 (83nm) / Ni(17nm) / Al(6nm) multilayers were grown on a single crystalline $MgF_2(110)$ substrate by e-beam evaporation. FeF_2 easy axis is in the sample plane, and was also found to be also the easy axis of the FM. The magnetization along the easy axis was measured using a SQUID magnetometer (Quantum Design). Since this system shows a very small coercivity 0.06 kOe, much smaller than the exchange bias field 0.9 kOe, it is ideal for studying this bi-domain state phenomenon.

Fig. II.1 shows the magnetization, M vs. H at $T = 10$ K after field cooling (FC) from 150 K in $H_{FC} = 0.5$ kOe (curve number 1), 0.75 kOe (2), 1 kOe (3), 1.25 kOe (4) and 2 kOe (5). For intermediate fields (0.75 kOe $\leq H_{FC} \leq$ 1.25 kOe) a double hysteresis loop is present with the EB and coercive fields of both subloops being almost identical, $|H_{EB}| \approx 0.9$ kOe and $|H_C| \approx 0.06$ kOe, respectively. Upon application of a smaller ($H_{FC} < 0.5$ kOe) or higher cooling field ($H_{FC} > 2$ kOe) only a single loop with negative or positive EB shift, respectively, is found. The dependence of H_{EB} as a function of H_{FC} is presented in the upper inset. A well-defined sharp crossover region with double hysteresis loops appears. The characteristic cooling field ranges depend on the material and the thickness of both FM and AF. For example, for the FeF_2(38 nm)/Co(4 nm) sample [Fig. II.4(b)], double loops were observed for cooling fields between 0.1 kOe and 30 kOe.

This shows that there are two spatially separated subsystems (bi-domain)

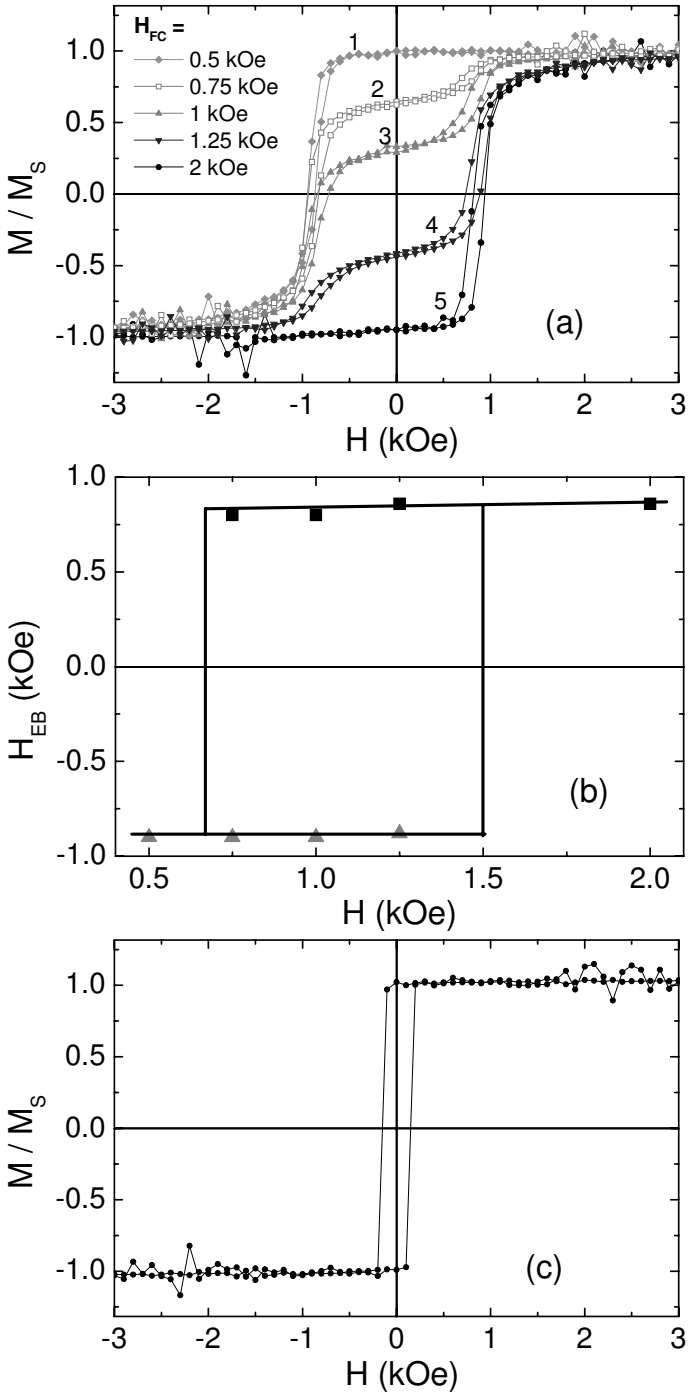

Figure II.1: (a) $M(H)$ at $T = 10$ K after field cooling in $H_{FC} = 0.5$ kOe (curve number 1), 0.75 kOe (2), 1 kOe (3), 1.25 kOe (4) and 2 kOe (5). (b) Extracted EB field H_{EB} vs. FC field H_{FC}. The field region, where double hysteresis loops (DHL) occur is denoted by two vertical lines. (c) $M(H)$ at $T = 90$ K $> T_N$. Solid lines are guides to the eye.

in the AF, each with a net frozen AF interfacial moment pointing parallel or antiparallel to the FC direction. Hence, each AF subsystem, or domain as defined in the introduction, gives rise to local EB on the FM [57, 79], exactly opposite to each other [56, 78, 24, 57, 79, 80, 81, 21]. The origin of the net AF interfacial moment is possibly due to a fraction of locked interfacial Fe^{2+} moments of the FeF_2 [37, 38]. The crossover from negative to positive EB (for a small or large H_{FC}, respectively) originates from the competition between the Zeeman energy of uncompensated AF moments and AF/FM exchange coupling energy during FC as reported in Ref. [52]. Positive EB arises when the interfacial AF moment freezes in the magnetic field direction under a cooling field large enough to overcome the AF interfacial coupling [8]. When the interfacial coupling dominates AF Zeeman energy for a small H_{FC}, the uncompensated AF moment orients opposite to the field and gives rise to negative EB. At an intermediate H_{FC}, it was found in twinned FeF_2 systems, a gradual shift from negative to positive EB is encountered accompanied by an enhanced coercivity, as shown in Fig. II.2 [60, 8]. This unexpected phenomenon was attributed to the spatial inhomogeneity at the interface that causes regions of uncompensated moments pointing either directions. However, in our case here, positive and negative EB with similar absolute values coexist (see upper inset of Fig. II.1). The difference must be due to the fact that in our samples the FM does not experience an average AF moment, S_{AF} [83], but rather two independent coexisting, mesoscopic AF/FM subsystems [24, 57, 79, 80]. The AF domain size has to be larger than the minimum domain size of the FM in order to avoid averaging. This coexistence of biasing directions can be explained either by a mesoscopic variation of the coupling strength, J_{AF-FM}, over the AF-FM interface or a third energy term being due to piezomagnetic or more generally magneto-elastic contributions [21]. The reason that an enhanced coercivity was observed in twinned FeF_2 systems as in Ref. [60], is due to the fact that averaging of AF domains of different biasing directions frustrates the FM. However, in our case, when the AF domain size is much larger than the FM, the FM behaves independently on each

AF domain, and no enhanced coercivity was observed.

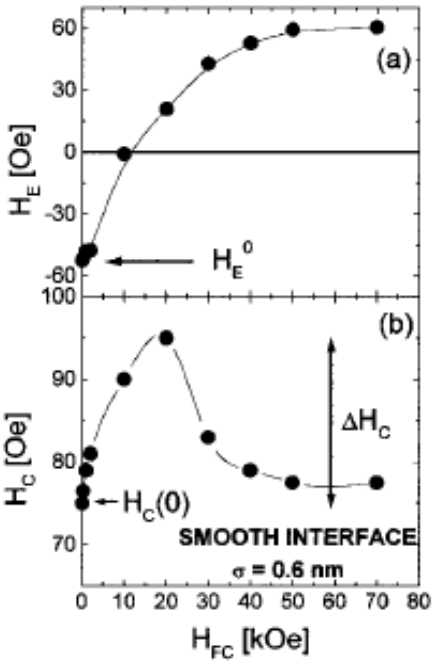

Figure II.2: This figure is cited from Ref. [60]. (a) Exchange bias field H_{EB} and (b) coercive field H_C vs. cooling field H_{FC}. The sample is a twinned-FeF_2/Fe bilayer on a MgO substrate.

The lower inset of Fig. II.1 shows a hysteresis loop measured at $T = 90$ K (above T_N). It displays a coercive field of $H_C \approx 0.15$ kOe and saturation at 0.25 kOe. Hence, all H_{FC} used in this study are larger than the saturation field at and above 90 K. This differs from several studies, where a double loop can only be found after demagnetizing the FM [56, 78, 24]. One should also note, that no perpendicular coupling is observable, as evidenced from measurements along the hard axis (data not shown). Interestingly, the Ni layer shows an easy axis along [001] even above T_N at 150 K (data not shown), although the X-ray diffraction data indicate a polycrystalline Ni layer. This may be due to a growth-induced anisotropy in the FM or an induced anisotropy by the interaction with the FeF_2 [84, 85].

The idea of two oppositely oriented AF domains is confirmed by another set of experiments, where the domain boundaries are moved by a field step. Fig. II.3

shows $M(H)$ curves of the same sample at $T = 10$ K after two different FC procedures: (i) FC from 150 to 10 K in either $H_{FC1} = 0.5$ kOe (single negatively shifted loop) or 2 kOe (single positively shifted loop), or (ii) first FC from 150 to 10 K in $H_{FC1} = 0.5$ kOe (1), followed by field heating from 10 K to T_S in 0.5 kOe (2), then change the field to 2 kOe at T_S (3) and finally FC from T_S to 10 K in $H_{FC2} = 2$ kOe (4) (inset of Fig. II.3). The data obtained from the FC protocol (i) is shown as solid symbols. The curves measured after the FC protocol (ii) are shown with open symbols. For $T_S = 81$ K no effect of the field change is observed. However, at a slightly higher $T_S = 82$ K a double loop is found and, finally, for $T_S = 83$ K virtually only a single positively shifted loop is encountered. Interestingly, a small signature of the negatively biased loop remains even at $T_S = 120$ K (data not shown). Hence, the AF bi-domain structure remains stable above the bulk Néel temperature of $T_N = 78$ K, although no bulk long range order is present. This is either a consequence of a broad distribution of blocking temperatures [85, 86] or a strain-induced enhancement of the AF/FM exchange coupling [72] and therefore an interfacial stabilization of the AF by the FM.

In summary, in this section, I showed that untwinned FeF_2/Ni exhibits a tunable double hysteresis loop for intermediate H_{FC}, and hence two oppositely biased subsystems (bi-domain state). This behavior is distinctively different from twinned FeF_2 exchange bias systems, where a gradual shift from negative to positive EB was found. Movement of the AF domain walls can be also induced by a field step through thermal activation. We argue that the criterion for obtaining independent subsystems is that the AF domain size must be larger than the minimum domain size (domain wall width) of the FM. This is confirmed in later sections where the AF domain size are probed by nanostructuring the FM (Section II.E), and micromagnetic simulation (Section II.F).

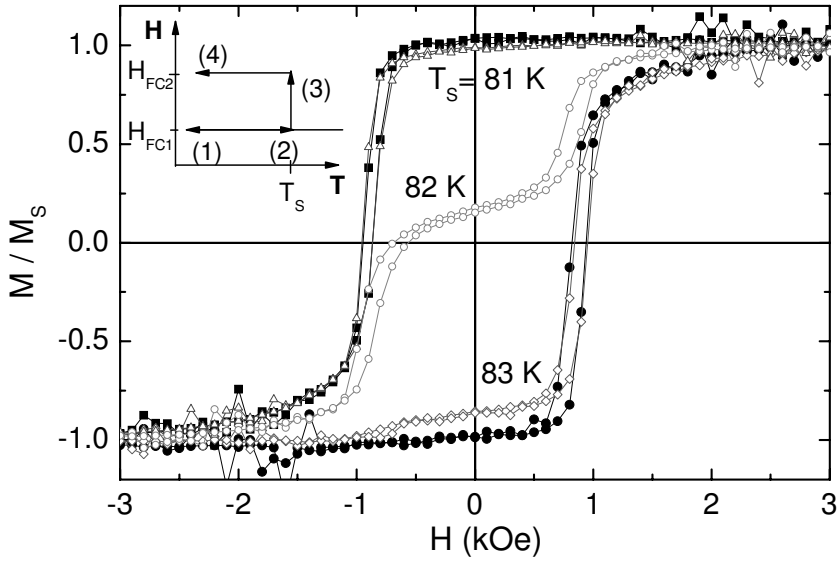

Figure II.3: $M(H)$ at $T = 10$ K after two different FC protocols. (i) FC in $H_{FC} = 0.5$ kOe (solid squares) and 2 kOe (solid circles) and (ii) FC as the schematic in the inset shows, where a field step is applied (see text) at $T_S = 81$ K (open triangles), 82 K (open circles) and 83 K (open diamonds), and $H_{FC1} = 0.5$ kOe and $H_{FC2} = 2$ kOe. Lines are guides to the eye.

II.C Comparison with Zero Field Cooling in Remanent State

As mentioned earlier, double hysteresis loops have been observed in exchange biased systems by zero field cooling (ZFC) after demagnetized above T_N [56, 78, 24]. In Ref. [78], the authors imaged the two independent and successive magnetization reversal processes at different regions of the FM, presumably corresponding to the initial demagnetized state of the FM. This result is not surprising, considering the fact that the demagnetized FM locally defines the orientation of the interfacial uncompensated AF spins. In this section, the same double hysteresis loop were reproduced by ZFC under equivalent conditions as found in the previous section by FC, and the same temperature evolution with the FC case was also found. Spatially resolved MOKE was performed and shows that the sample indeed break down into regions of positive or negative biasing directions.

Untwinned FeF_2 (50 nm)/ Co (4 nm) / Al (3 nm) grown on a MgF_2 (110)

substrate was studied for this purpose. The in-plane sample magnetization was measured by a SQUID magnetometer and magneto-optical Kerr effect (MOKE). Typical non-biased single hysteresis loop was found for all samples above T_N.

In the ZFC experiment, the sample was first demagnetized at 300 K to a chosen value of the remanent magnetization along the easy axis, M_R, between 0 and the saturation magnetization M_S. This leads to the formation of FM domains with the magnetizations in opposite directions along the easy axis. The balance between the magnetization of the two types of domains determines the resultant magnetization of the sample. After the sample is cooled in zero magnetic field below T_N, the magnetic moment is measured as a function of applied magnetic field at various temperatures. The sample cooled from full remanent magnetization, $M_R \approx M_S$ shows single hysteresis loops exchange biased to negative fields by $H_{EB}(T)$ [Fig. II.4(a)]. In contrast, the sample cooled with a reduced remanent magnetization shows double hysteresis loops (*e.g.* Fig. II.4(a) for $M_R \approx 0.5M_S$ and $M_R \approx 0$). Each loop is shifted along the magnetic field axis by the same absolute value of temperature-dependent $H_{EB}(T)$, but in the opposite directions. The loop height ratio is set by the remanent state, in which the sample was cooled, and it is equal to the magnetization ratio of the two types of domains in that state. Thus, the system "remembers" the remanent magnetization state above T_N.

Similar to the previous section, the same sample was also field cooled (FC) below T_N at various H_{FC} [Fig. II.4(b)]. Negative EB, coexistence of both signs, and positive EB were found for 0.1 kOe, 2 kOe and 30 kOe, respectively. It is remarkable that positive and negative $H_{EB}(T)$ of equal absolute value are found at all temperatures below T_N (Fig. II.5). At any particular temperature, the width of both loops is equal to that of the single hysteresis loop (twice the coercive field, $2H_C$). When rescaled vertically, both the single loops and each of the double loops have nearly identical the same shape and temperature evolution. Thus, two types of independent regions are formed with identical properties, one positively and the other negatively exchange biased.

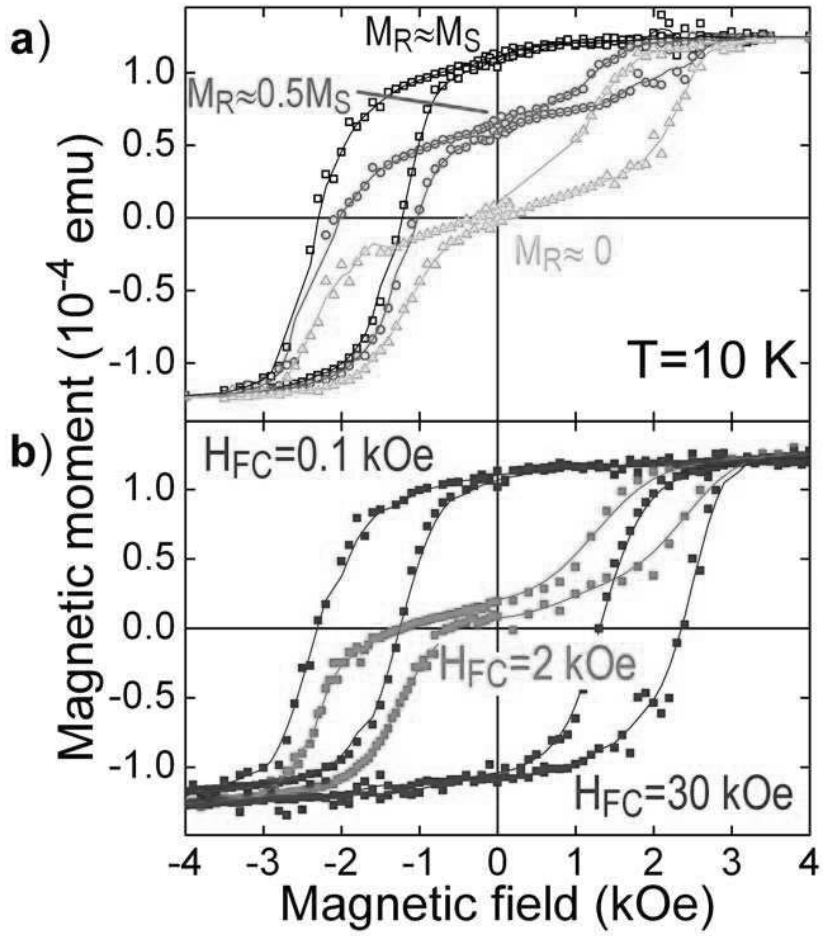

Figure II.4: Easy axis magnetization loops for the FeF_2(38 nm)/Co(4 nm) sample below T_N, at 10 K, (a) ZFC with three values of the remanent magnetization, M_R: M_S, $0.5M_S$, 0, and (b) FC in various fields: H_{FC} = 0.1 kOe, 2 kOe, 30 kOe.

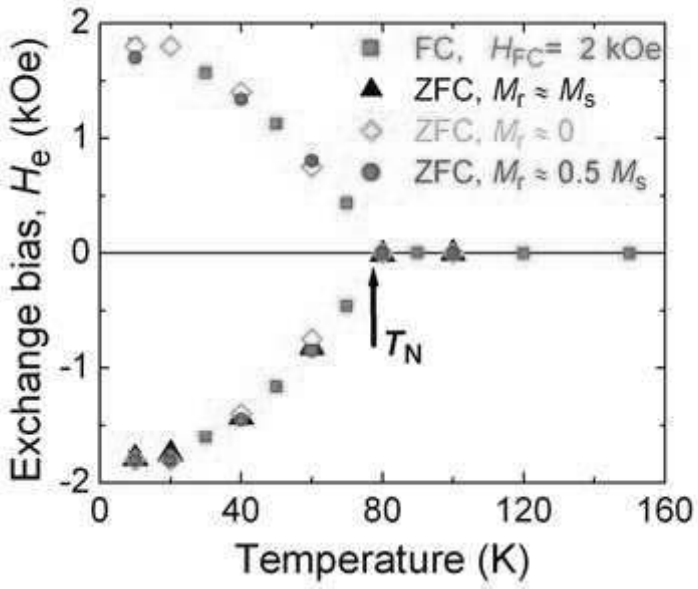

Figure II.5: Temperature dependence of the exchange bias field, H_{EB}, (magnetization loop shift) for the single and each of the double loops presented in fig. II.4.

Spatially resolved MOKE was performed to probe the two biasing regions. For this experiment, a $5mm \times 5mm$ FeF_2(70 nm)/Ni(70 nm)/Al(4 nm) sample was first demagnetized above T_N and then cooled below T_N in a zero magnetic field as done in the ZFC case. First, the MOKE signal as a function of applied magnetic field was collected from the entire sample surface area, illuminated with a wide beam. The curve consists of a double hysteresis loop [Fig. II.6(b)]. Without any change in the experimental conditions, MOKE measurements are performed using a $\sim$ 500 μm diameter laser beam at 16 spots arranged in a 4×4 matrix, in the positions shown in the Fig. II.6(a). The resultant signal [Fig. II.6(a)], which is proportional to the magnetization, varies spatially: on one side of the sample the single loop is negatively shifted, on the other side - the single loop is positively shifted, and in between - double hysteresis loops are found. The normalized sum of these 16 curves [green triangles in Fig. II.6(b)] is in good agreement with the hysteresis curve obtained from the entire sample (black circles). The slight difference between the two curves is due to incomplete coverage of the surface area by

the 16 measured spots.

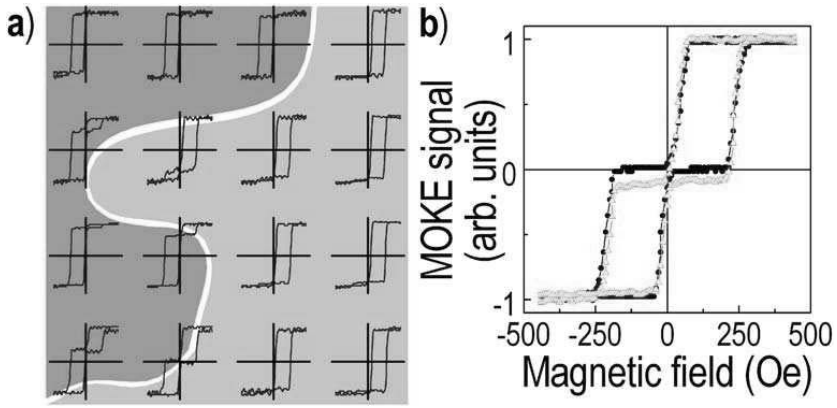

Figure II.6: Magnetic hysteresis loops along the easy axis, measured with MOKE on a 5 mm × 5 mm sample: (a) at different parts of the sample as indicated on the figure, with a $\sim$ 500 μm laser spot, (b) from the entire sample surface area (black circles), and the average of the 16 curves in (a) (gray triangles). The background color in (a) represents the local direction of the EB: dark gray - negative, gray - positive.

This experiment confirms that the sample has two types of areas; single hysteresis loops exhibit the same H_{EB}, positively in one area, and negatively in the other. When the laser beam covers parts of both areas, the magnetization curve consists of two loops shifted in opposite directions, with their relative heights determined by the ratio of the two areas.

Similar attempt was also made for the FC case. Small spatial variations were also found, but it was not possible map out the positively / negatively regions. We attribute this failure to the much smaller AF domain size than the size of the laser probe in the FC case. The $\sim$1 mm^2 AF domain size in the ZFC case is defined by the size of FM domains created in the demagnetization process above T_N, while in the FC case, AF domains form spontaneously most likely due to interfacial inhomogeneity, thus its size is linked to some intrinsic length scale of the inhomogeneity. It is possible to probe this length scale by patterning the FM into sub-micron structures ($\sim$ 100 nm). As will be shown in section II.E, the relevance of the AF domain size with dot sizes gives rise to strong changes in the cooling field dependence. In the next section, the two-step magnetization reversal

process in the FC case was studied by vector magnetometry.

II.D Magnetization Reversal in Double Hysteresis

The same sample as in section II.B (Al (7.6 nm) / Ni (21 nm) / FeF_2 (50 nm) on MgF_2 (110)) was studied. The same structure was also deposited by e-beam evaporation on single crystal MgO (100) and Si (100) substrates when FeF_2 was respectively twinned (110) and polycrystalline FeF_2 in comparison with untwinned FeF_2 [8, 87, 35, 57]. Field cooling and magnetic measurements have been performed in a vibrating sample magnetometer (VSM). The same FC procedure were applied to all samples. Both longitudinal moment ($m_{//}$, the component parallel to H) and transverse moment ($m_{\perp}$, the component in the film plane but perpendicular to H) have been measured with vector detection coils. At 15 K, the polycrystalline sample has an exchange field H_{EB} of about -0.3 kOe, with no appreciable dependence on H_{FC}. The twinned film displays a larger H_{EB} of -0.7 kOe in H_{FC} =1 kOe and -0.6 kOe in H_{FC} =15 kOe (measured with the field along MgO [001]). Below we concentrate on the Ni/epitaxial-FeF_2.

The magnetic hysteresis loops of the longitudinal (solid circles) and transverse (open circles) moments under different H_{FC} are shown in Fig. II.7. At H_{FC} = 2 kOe, a single longitudinal loop was found, negatively biased with a $H_{EB} \approx -1$ kOe (Fig.
refKaiFig1(a)) which is larger than that in Ni/twinned-FeF_2. As H_{FC} is increased (2 kOe < H_{FC} < 15 kOe), double hysteresis loops were encountered. Finally at H_{FC} = 15 kOe, the loop is completely positively shifted with $H_{EB} \approx +1$ kOe.

The transverse loops show peaks at the fields corresponding to the switching fields of the longitudinal (sub)loops. We will use "upward" and "downward" to represent directions in the film plane that are perpendicular to the applied field, corresponding to positive and negative transverse moment, respectively. For H_{FC} = 2 kOe, the transverse loop shows two positive peaks at $H \approx -1$ kOe - one for

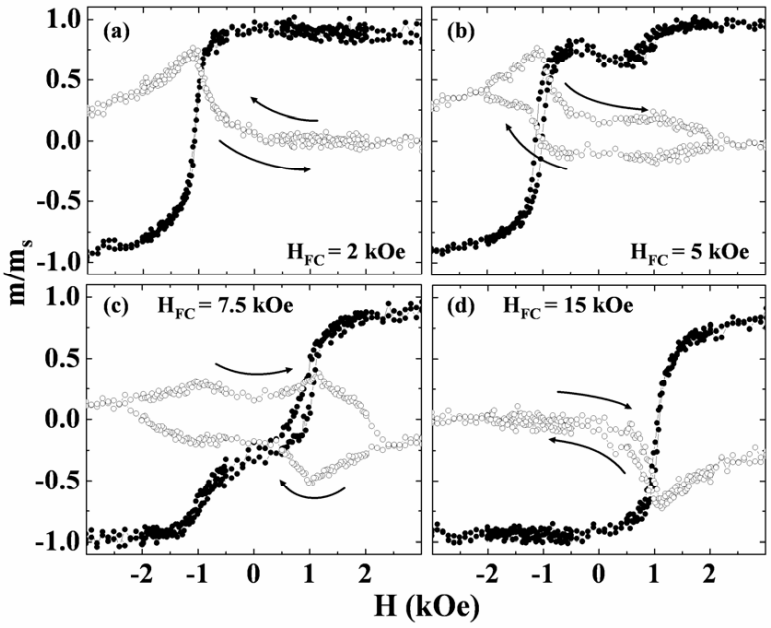

Figure II.7: Longitudinal ($m_{//}$, solid circles) and transverse ($m_{\perp}$, open circles) magnetic hysteresis loops of Ni/FeF_2 field cooled in H_{FC} of (a) 2 kOe, (b) 5 kOe, (c) 7.5 kOe, and (d) 15 kOe. The moments are normalized to the saturation moment m_s. Arrows indicate the field-cycle sequence for the transverse loop.

each branch of the field cycle (Fig. II.7(a)). Both peaks have large magnitudes, ∼82% of the saturation moment, m_s. This indicates that most of the sample reverses its magnetization via rotation, as opposed to domain nucleation and motion. In films with twinned and polycrystalline FeF_2, we usually observe a smaller transverse peak, ∼ 10-60% of the total magnetization. As H_{FC} is increased, a pair of peaks at $H \approx \pm 1$ kOe is observed for each field-sweep direction (Fig. II.7(b) and (c)). For the decreasing-field branch, the transverse moments point downward while those in the increasing-field branch point upward. Note that once the positively biased sub-loop appears, magnetization reversal from positive saturation changes from upward (Fig. II.7(a)) to downward rotation (Figs. II.7(b)-(d)). For different H_{FC}, the transverse peak locations stay constant; only the peak magnitudes change. Finally, for $H_{FC} = 15$ kOe, the transverse hysteresis loop shows two peaks at $H \approx +1$ kOe - again one for each field sweep branch (Fig. II.7(d)). The moments always point downward (negative), whose maximum magnitude is also $\sim 82\% m_s$.

The behavior of the longitudinal (sub)loops and transverse peaks can be attributed to the existence of two regions of FM domains, FM-A and FM-B, which respectively correspond to the negatively and positively biased sub-loop. The sizes, or fractions, of each region are apparent in both the longitudinal and transverse loops. In the longitudinal direction, the domain fraction can be defined as

$$m^A_{//}\text{fraction} = |m^A_{//}|/2m_s \tag{II.1}$$

$$m^B_{//}\text{fraction} = |m^B_{//}|/2m_s \tag{II.2}$$

where $m^A_{//}$ and $m^B_{//}$ are the moments associated with the sub-loops, as schematically shown in Fig. II.8 (a). In the transverse direction, the domain fraction can be defined as

$$m^A_{\perp}\text{fraction} = |m^A_{\perp}|/2m_s \tag{II.3}$$

$$m^B_{\perp}\text{fraction} = |m^B_{\perp}|/2m_s \tag{II.4}$$

where $m_{\perp}^{A}$ and $m_{\perp}^{A}$ are the local maximum (peak) moment value near $H = \pm 1$ kOe, as schematically shown in Fig. II.8(b).

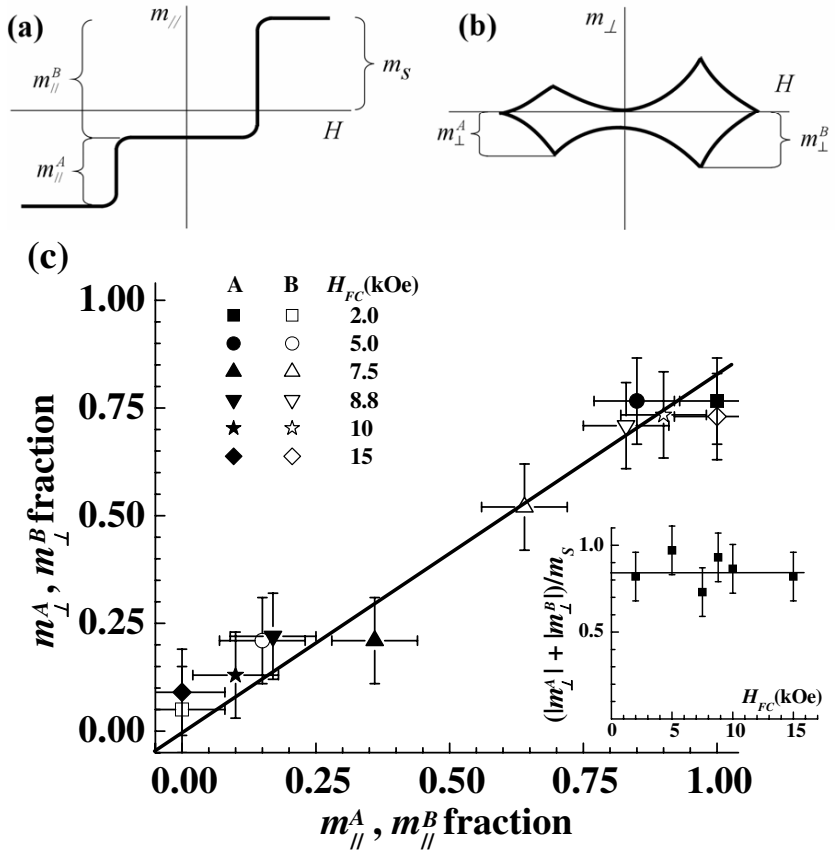

Figure II.8: Illustrations of the determination of (a) longitudinal and (b) transverse domain fractions, as defined in Eqn. 1-4 in the text. The asymmetric transverse peaks are caused by a misalignment between the magnetic field and the anisotropy axis, as explained in the text. (c) Correlation between the longitudinal and transverse domain fractions, for all cooling fields. Solid and open symbols represent domain A and B, respectively. Solid line is a guide to the eye with a slope of 0.85. The inset of (c) shows the sum of $m_{\perp}^{A}$ and $m_{\perp}^{B}$ fractions, where the horizontal line indicates about 85% of the FM reverse by rotation.

As shown in Fig. II.8(c), there is a clear one-to-one correlation between the domain fractions in longitudinal and transverse loops. At $H_{FC} = 2$ kOe, there is no kink in the longitudinal loop, thus the $m_{//}^{A}$ fraction is 1.00, and the corresponding $m_{\perp}^{A}$ fraction is 0.82. At $H_{FC} = 15$ kOe, similar $m_{//}^{B}$ and $m_{\perp}^{B}$ fractions are observed. Between 2 and 15 kOe, with increasing H_{FC}, the FM-B fraction

gradually increases at the expense of FM-A. This is manifested in the longitudinal loop as the middle plateau sweeps downward, and in the transverse loop as the negative $m_\perp$ peak at $H \sim +1$ kOe grows in size. It is interesting to note that $|m_\perp^A|+|m_\perp^B|$ is ~85% m_s, as shown in Fig. II.8(c) inset. The correlation demonstrates that at any H_{FC}, ~85% of the FM reversal is by rotation, either in one step or by two successive rotations!

This FM reversal process can be consistently explained by the aforementioned AF domains formed during FC process (Fig. II.9). As shown in Fig. II.9(a), the applied field is pointing to the right, defined as the positive direction for longitudinal moment $m_{//}$; 90° counterclockwise is defined as the positive (or upward) direction for the transverse moment $m_\perp$. Also shown is an inevitable but exaggerated misalignment between the anisotropy directions and the applied field (dashed lines) during cooling and measurement. At $H_{FC} = 2$ kOe, domain A is favored. Its unidirectional exchange anisotropy H_{EB}^A has a small upward component due to the aforementioned misalignment. This component then guides the magnetization to rotate upward during reversal from $+H$ to H_{EB}^A and $-H$, as illustrated in Fig. II.9(b), and then $-H$ to H_{EB}^A and $+H$ during the returning path, leading to the positive m peaks at $H \sim$ -1 kOe. Since H_{EB}^A is in close alignment with $+H$, as opposed to $-H$, the reversal from/to positive saturation is always sharper than that from/to negative saturation, as seen in Fig. II.7(a). Similarly, at $H_{FC} =$ 15 kOe, domain B is favored. Its unidirectional anisotropy H_{EB}^B has a downward component, forcing downward magnetization rotation from $+H$ to H_{EB}^B and $-H$ (Fig. II.9(c)) and resulting in the negative peak at $H \approx +1$ kOe in the transverse loop.

At $H_{FC} = 5$ and 7.5 kOe, both types of domains are present in the AF layer. At large applied fields, the FM layer is single-domained. As the field is reduced, the AF domain structures break the FM layer into domains where the FM reversal is dictated by the first FM domain to rotate in each field sweep direction. Along the decreasing-field sweep, the positively shifted sub-loop associated with

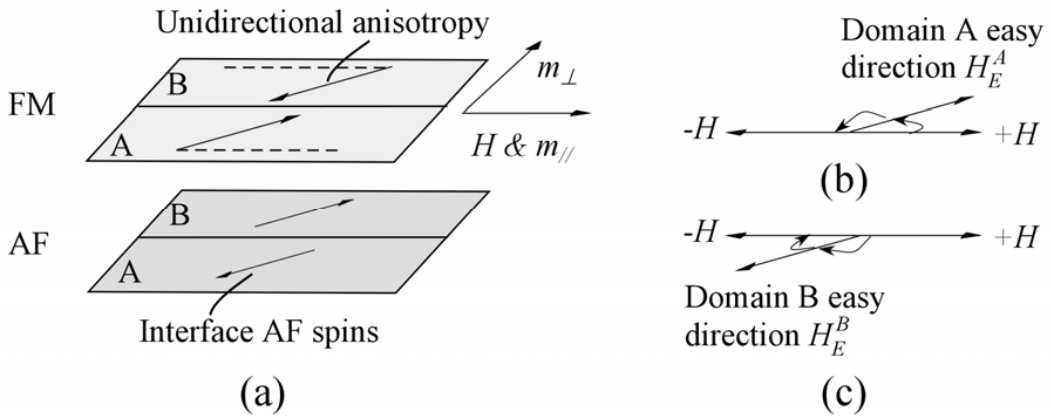

Figure II.9: (a) Schematic of the two regions of large FM/AF domain structures, with respect to the applied field H direction. A misalignment between the anisotropies and the field direction, illustrated by the dashed lines, is exaggerated. The orientation of the easy direction in (b) domain A and (c) domain B differentiates the magnetization rotation direction.

domain B experiences reversal first. The downward rotation leads to a negative m peak at $H \approx +1$ kOe. As H continues to decrease, the FM-A spins start to rotate. The small upward component of H_{EB}^A alone would pull the moments to rotate upward to form a positive $m_\perp$ peak at $H \approx -1$ kOe. However, the already rotated FM-B now drag the FM-A spins to rotate in the same orientation, so as not to create a domain wall that is over 180 degrees. Eventually both domains are saturated along $-H$. In the increasing-field sweep, FM-A spins are the first to reverse at -1 kOe. Now the small upward component of H_{EB}^A indeed pulls the FM spins to rotate upwards, which in turn drag FM-B spins to also rotate upward (rather than downward) at + 1 kOe. Hence, the $m_\perp$ peaks in general are both negative and both positive for the decreasing- and increasing-field sweep, respectively [88].

It is interesting to note that the exchange field is larger in Ni/untwinned-FeF_2 than in twinned or polycrystalline FeF_2, where the latter is expected to have a smaller AF domain size. This difference in H_{EB} actually can be accounted for by the angle between the AF easy axis and the applied field. This gives a factor $\cos 45^\circ = 0.7$ in case of twinned FeF_2, and $\int_0^\pi \cos\theta d\theta = 0.5$ in case of polycrystalline

FeF_2 [89]. Therefore, the exchange bias field is actually not sensitive to the AF domain size in this system. This is opposite to some of the theoretical predictions [11, 19, 18, 16, 31, 90] as well as experimental results in $Co/LaFeO_3$ [91].

II.E Probing AF Domain size by Nanostructuring FM

In this section, the FM was patterned on top of a continuous AF thin film in order to probe the AF domain size, especially in untwinned FeF_2 on MgF_2 substrates. By varying the FM dot size, we found H_{FC} dependence of EB can be strongly modified, while H_{EB} remains unchanged. We ascribe this behavior to the relevance of FM dot sizes with the AF domain size, estimated to be around 500 nm.

Ni(30 nm)/FeF_2(30 nm) bilayer capped with 4 nm Al was deposited on a MgF_2 (110) single crystal substrate by e-beam evaporation [55]. FeF_2 grows epitaxially untwinned in (110) orientation, whereas the Ni layer is polycrystalline. FeF_2 is an AF with $T_N = 78$ K. Subsequent e-beam lithography followed by Ar^+ milling patterned the Ni layer into circular sub-micron dot arrays. Two groups of arrays were made. For the first group, the dot diameters are $d = 400$ and 700 nm with periodicity $D = 600$ and 1200 nm, respectively, measured by atomic force microscope (AFM) (Fig. II.10). The second group keeps the periodicity constant $D = 300$ nm, while varying the dot diameter $d = 120$, 170 and 180 nm. A second sample with 30 nm thick Fe dots on top of a continuous FeF_2(30 nm) thin film was made on a MgO (100) single crystal substrate as a comparison. The dot diameters are $d = 100$, 300 and 600 nm with $D = 2d$. FeF_2 grows twinned in (110) orientation on MgO (100) substrates. Single and double hysteresis loops for intermediate H_{FC} have been observed in unpatterned samples on MgO and MgF_2 substrates, respectively [8, 57]. Magnetic measurements were made using magneto-optical Kerr effect (MOKE) at $T = 10$ K below the Néel temperature, after cooling down at various H_{FC}. Superconducting quantum interference device

(SQUID) was used to measure unpatterned thin films.

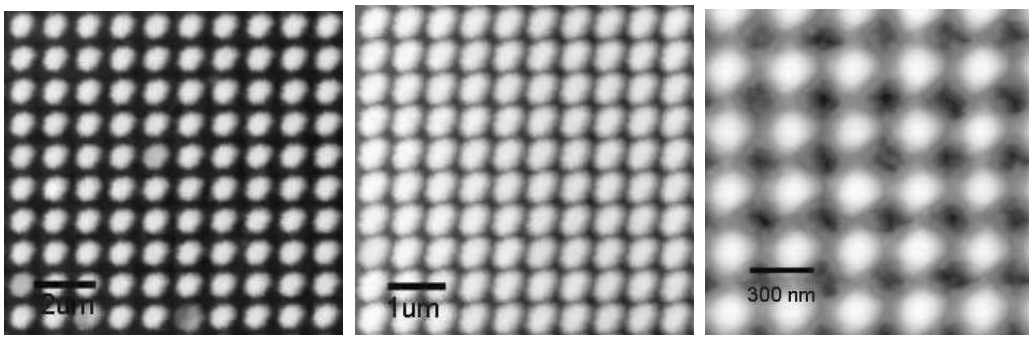

Figure II.10: Atomic force microscope images of the Ni dots on top of a continuous FeF_2 thin film on a MgF_2 substrate. The images from top to bottom show dots of diameters $d = 700$, 400 and 120 nm and periodicities $D = 1200$, 600 and 300 nm, respectively.

SQUID measurement of the Ni/FeF_2 unpatterned thin film on a MgF_2 substrate shows typical results as observed before. Negative and positive EB was observed for $H_{FC} < 10$ kOe and $H_{FC} > 40$ kOe, respectively, with $H_{EB} = \pm 1.1$ kOe. Coexistence of negative and positive EB was observed when 10 kOe $\leq H_{FC} \leq 40$ kOe. For patterns of all sizes and periodicities, no significant changes in $|H_{EB}|$ were observed. This is in contrast with most observations in the literature, where both enhancement [41, 77, 76] and suppression [74, 75, 44, 77, 92] of H_{EB} were observed. However, the H_{FC} dependence of H_{EB} is strongly dependent on the dot size. For example, Fig. II.11 shows the hysteresis loops of the dots with $d = 120$ nm and $D = 300$ nm with $|H_{EB}| = 1.2 \pm 0.1$ kOe for different H_{FC}. In this case, fully positive EB was encountered for H_{FC} as low as 5 kOe, which is nearly an order of magnitude lower than the smallest $H_{FC} = 40$ kOe for fully positive EB when it is unpatterned. Fig. II.12 shows the occurrence of negative, positive EB or coexistence of both as a function of H_{FC} and dots sizes for two groups of patterns. Similar trend was found for both groups, where the onset H_{FC} for positive EB decreases with decreasing dot sizes.

In comparison, Fe dots on top of twinned FeF_2 continuous thin films were also measured. The unpatterned film does not show positive EB as expected, even

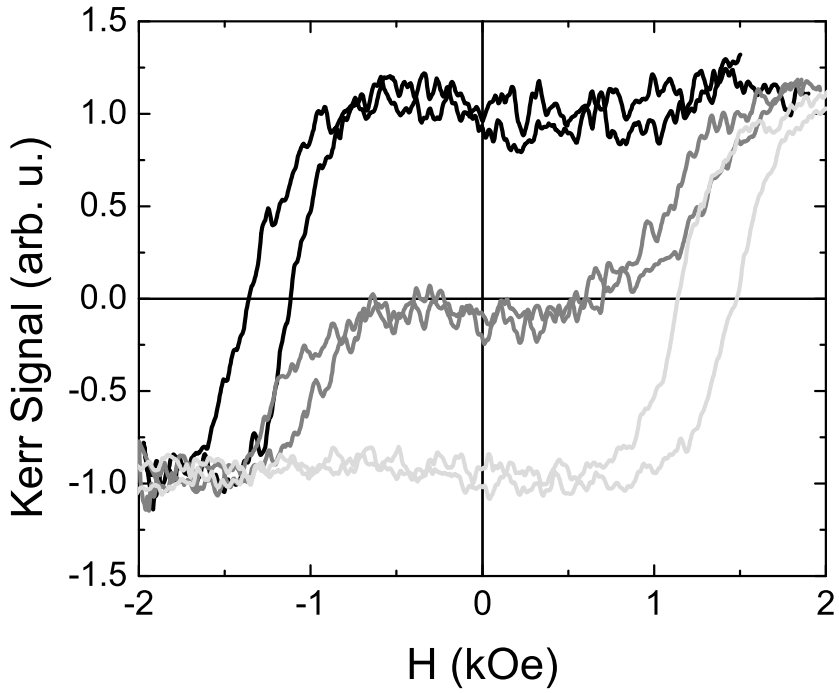

Figure II.11: Hysteresis loops for dots of diameter $d = 110$ nm and periodicity $D = 300$ nm measured at $T = 10$ K with cooling fields $H_{FC} = 2$ kOe (black), 3 kOe (gray) and 5 kOe (light-gray).

with $H_{FC} = 70$ kOe. Only a small increase of H_{EB} was observed, from -100 Oe for $H_{FC} = 5$ kOe to -70 Oe for $H_{FC} = 70$ kOe. Table II.1 shows the dot size dependence of H_{EB} for $H_{FC} = 5$ and 70 kOe, and the change of the exchange bias field ΔH_{EB}. The non-monotonic dot size dependence of H_{EB} at $H_{FC} = 5$ kOe has been attributed to the occurrence of vortex state in dots of $d = 300$ nm. The dot size dependence of ΔH_{EB} shows that large H_{FC} shifts H_{EB} more strongly toward positive EB for smaller dots. This result is consistent with the trend found in untwinned FeF_2/Ni.

It is worth noting that the interdot dipolar interaction has negligible effect on the sign of H_{EB}, because it is determined by the sign of uncompensated AF moments frozen in the cooling process when all FM dots are saturated.

The sign of EB was attributed to the competition between the Zeeman energy of uncompensated AF moments and the antiferromagnetic interfacial coupling [8]. For a small H_{FC}, the antiferromagnetic interfacial coupling dominates

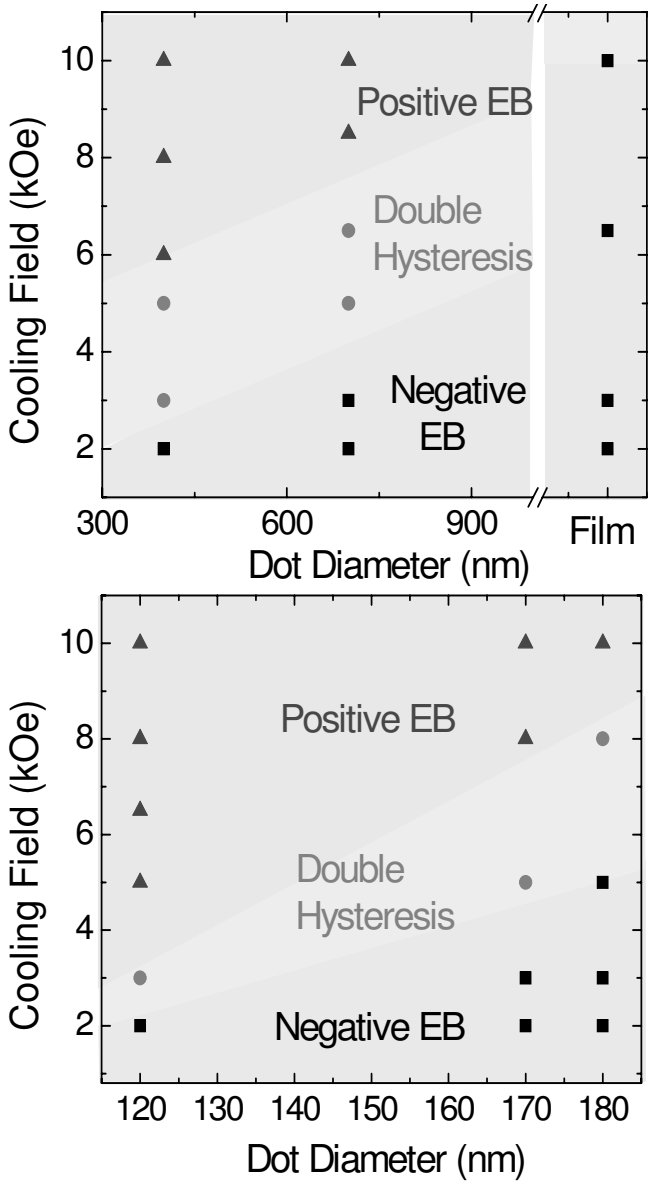

Figure II.12: The occurrence of negative (squares), positive EB (triangles) or coexistence of both (circles) as a function of cooling fields and dot sizes on the same sample. The top panel shows the result on dots with diameters d=400 and 700 nm and the unpatterned film. The bottom panel shows the result of dots with diameters d=120, 170 and 180 nm. The different shades of gray in the figures are a guide to the eye for regions of negative, positive EB and coexistence of both.

Table II.1: Exchange bias measured at $T = 10$ K for different cooling fields H_{FC} and dot diameters of Fe dots/twinned FeF_2. H_{EB1} and H_{EB2} refer to the exchange bias after cooling down at $H_{FC} = 5$ and 70 kOe, respectively, and $\Delta H_{EB} = H_{EB2} - H_{EB1}$ is their difference.

Diameter (nm)	H_{EB1} (Oe)	H_{EB2} (Oe)	ΔH_{EB} (Oe)
100	-185	-20	165
300	-55	30	85
600	-110	-30	80
Film	-100	-70	30

the AF Zeeman energy, orienting uncompensated AF moments in the negative direction, and leading to negative EB. However, a large H_{FC} aligns AF uncompensated moments in the positive direction, and results in positive EB. In case of a patterned FM, the competition becomes more complicated since AF domains are not fully covered by FM dots(Fig. II.13). For AF domains not covered by the FM, the uncompensated AF moments are aligned by H_{FC} without the interfacial coupling. For AF domains partially covered by the FM, the interfacial coupling contributes only partially to the competition with H_{FC}. Therefore, a lower H_{FC} would be expected to align the uncompensated AF moments with the field in these domains than to align those in fully covered AF domains. Since these partially covered AF domains occur around the edge of FM dots, they become more and more significant as the dot size decreases. Therefore, smaller dots are or tend to be driven into positive EB at lower H_{FC}, as observed in samples with twinned and untwinned FeF_2.

A quantitative evaluation can be made to estimate the domain size of untwinned FeF_2. The unpatterned thin film starts to show positive EB at $H_{FC} =$ 10 kOe. Thus, for that part of the sample that shows positive EB, the interfacial coupling energy, noted as $\mathcal{H}_{I0}$, is equal to the Zeeman energy $\mathcal{H}_{Z0}$ of the uncompensated AF moments, or $\mathcal{H}_{I0} = \mathcal{H}_{Z0}$. Assuming the AF domain size x is smaller than half of the periodicity so that FM dots are independent of each

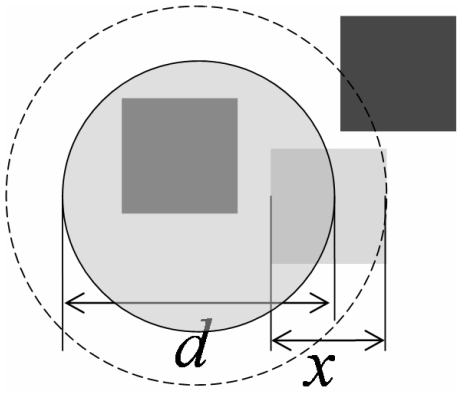

Figure II.13: A schematic of AF domains (denoted by squares), either not covered (black), partially covered (gray) or fully covered (dark-gray) by a FM dot (solid circle). AF uncompensated moments inside the dash-line circle are effectively involved in the competition with the interfacial coupling (see text).

other on average, the interfacial coupling energy is proportional to the area of a FM dot $\pi d^2/4$, while the effective AF Zeeman energy is proportional to an area with its diameter increased by x, thus $\pi(d+x)^2/4$. Therefore, the effective contribution of AF Zeeman energy to the competition is increased by a factor of $(\pi(d+x)^2/4)/(\pi d^2/4) = (d+x)^2/d^2$ (Fig.II.13), compared with an unpatterned film. For dots with $d = 700$ nm, (3.5 ± 1) kOe is necessary to induce positive EB. Therefore, the Zeeman energy of AF uncompensated moments is reduced to $0.35(d+x)^2/d^2\mathcal{H}_{Z0}$. Therefore, we have $0.35(d+x)^2/d^2\mathcal{H}_{Z0} = \mathcal{H}_{I0}$, that is, $0.35(d+x)^2/d^2 = 1$, or $x = (500 \pm 200)$ nm. For smaller dots, the above assumption that $x < D/2$ becomes invalid. However, if applying the above calculation to 400 nm dots, one will get $x = (400 \pm 150)$ nm, slightly larger than half of the periodicity, consistent with the above estimate. This estimate of AF domain size $x \approx 500$ nm is consistent with previous prediction, that double hysteresis loops occur when AF domain size is much larger than the FM domain wall width [55], which is about 80 nm for Ni [73]. For dots with $D = 300$ nm, the cooling field dependence can be explained with the reduced uncovered AF surface with increasing dot sizes, thus larger H_{FC} necessary for positive EB. For example, for $d = 120$ nm, the ratio of the AF surface covered by the FM dot is $(\pi d^2/4)/D^2 = 0.13$. Since

the onset H_{FC} for positive EB in an unpatterned film is 10 kOe, the onset H_{FC} for 120 nm dots should be 1.3 kOe, reasonably close to what is fond experimentally, $H_{FC} = 2$ kOe.

In summary, we have observed a strong cooling field dependence of exchange bias in sub-micron circular dots. With decreasing dot sizes, the FM becomes more strongly influenced by the cooling field. In case of the untwinned FeF_2 sample, positive EB was observed with cooling fields an order of magnitude smaller than what is necessary for the unpatterned sample. This unexpected behavior is attributed to the lateral length scale relevance of the FM dot size and the AF domain size, which is estimated to be around 500 nm in untwinned FeF_2.

II.F Micromagnetic Simulation

In order to investigate the origin of double hysteresis loops and verify the role of the AF domain size compared with the FM domain wall width, micromagnetic simulations of a polycrystalline Ni layer of 20 nm thickness and lateral size 500×500 nm^2 were performed using the OOMMF micromagnetic simulation package [70]. We assumed 10% of randomly distributed, rigid, uncompensated AF interfacial moments, S_{AF}, being exchange coupled to the bottom layer of the FM [93, 94]. The interfacial coupling strength was taken to be twice the exchange constant in bulk FeF_2 [95, 96] i.e. $J_{AF/FM} = -0.90$ meV. Apart from micromagnetic parameters for Ni, we also included the demagnetizing effect by a shape anisotropy constant, $K_d = -(\mu_0/2)M_S^2 = -148$ kJ/m^3, forcing the spins to be oriented in-plane. During the simulation, no dipolar energy was taken into account to avoid artifacts due to the simulation boundary, especially curling of spins along the the boundary. A uniaxial anisotropy constant, $K_u = -15$ kJ/m^3 introduces an in-plane easy-axis, qualitatively similar to the experimental situation. The bi-domain state of the AF was modeled by laterally dividing the system in areas of size D_{AF} in the x-y-plane with two opposite orientations of the rigid AF moments

along the easy-axis. Both D_{AF} and the areal ratio of the two opposite biasing directions were varied. The external magnetic field is applied parallel to the easy axis. Fig. II.14 shows the spatial distribution of the pinning field for D_{AF} = 250, 125, 60, 30 nm, with equal coverage of two types of domains.

Fig. II.15 (a) shows the calculated hysteresis loops, $M(H)$, for different AF subsystem sizes, D_{AF}. A transition from one broad loop (D_{AF} = 30 nm) to two separated subloops (D_{AF} = 250 nm) is found. The curves for D_{AF} = 30 and 60 nm exhibit a slight EB shift due to a statistical imbalance of the randomly chosen frozen AF moments. The value for D_{AF} necessary to produce double loops has to be compared to the domain size of Ni, whose lower limit is determined by the domain wall width, δ_{DW}. This value reflects the length scale over which the FM averages the exchange interaction with the interfacial AF uncompensated moments [57, 79]. Using the formula for a Bloch wall width $\delta_{DW} = \pi\sqrt{A/(K_1 + K_u)}$ and the values mentioned above for K_1 and K_u one arrives at δ_B = 41 nm. The simulation proves that double hysteresis loops are observed, when the criterion, $D_{AF} >> \delta_{DW}$, is fulfilled as in cases of D_{AF} = 125 and 250 nm. In addition, spin structures of the top and the bottom layer at remanence (H = 0) for D_{AF} = 30 and 250 nm are shown in Fig. II.15 (b). One clearly observes an averaging effect for the 30 nm subsystem size. While the bottom layer still reflects the topology of opposite orientations of the subsystems, the top layer is virtually only positively magnetized. However, for D_{AF} = 250 nm both the top and bottom layer show clearly separated regions with opposite magnetization directions.

To compare in greater details the two extreme cases with D_{AF} = 250 and 30 nm, where double and single hysteresis are encountered, respectively, the ratio of positive bias is varied between 0 and 1. As shown in Fig. II.16(a), when D_{AF} = 250 nm, the FM always reverses through a two-step process, with the ratio of the two steps varying according to the coverage ratio of the two biasing directions, just as we observed experimentally (Fig. II.1). When D_{AF} = 30 nm, the FM exhibits a singly shifted hysteresis with increasing exchange bias field

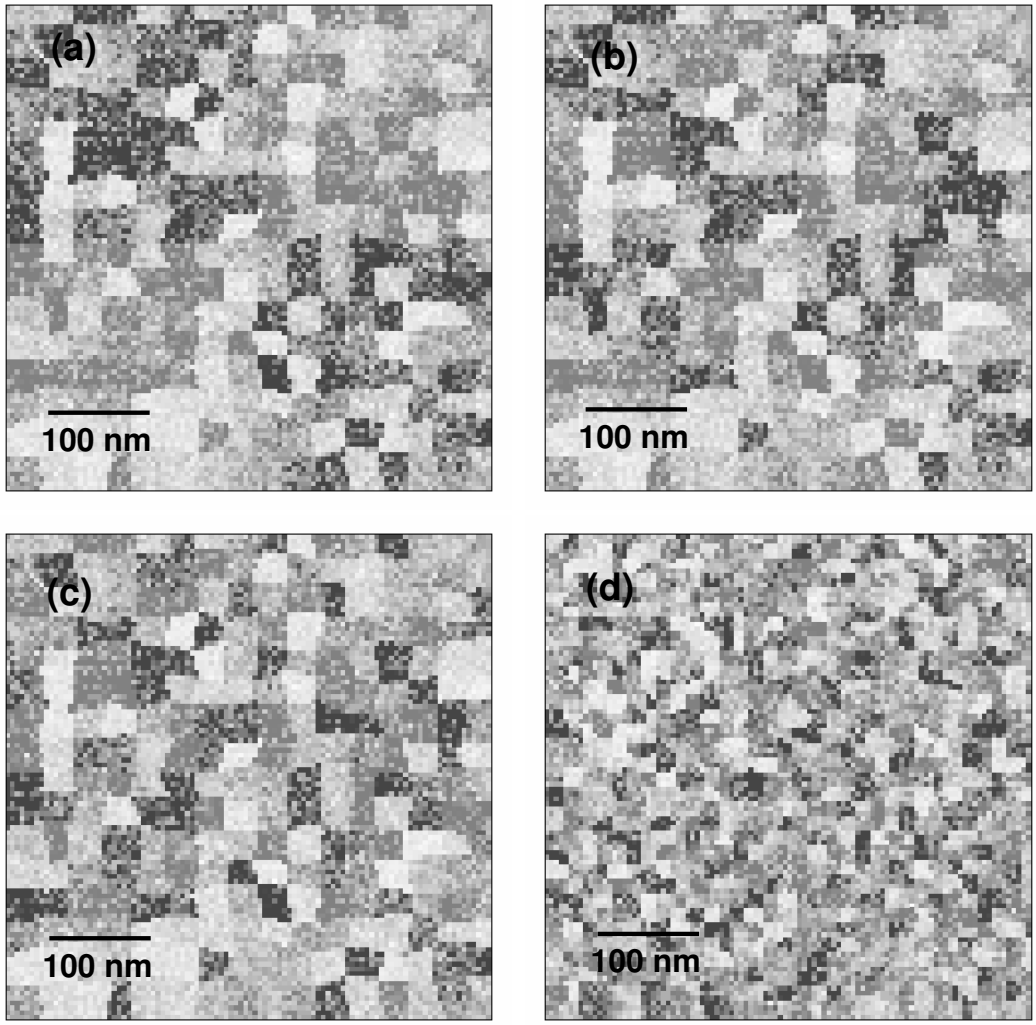

Figure II.14: Spatial distributions of the AF pinning field that measures 500 × 500 nm^2 on the bottom layer of Ni for AF domain size D_{AF} = 250 (top left), 125 (top right), 60 (bottom left), 30 (bottom right). The gray scale represents the x component of the pinning field, and is coded as gray-white-black for 1 - 0 - (-1). The spatial inhomogeneity within each domain was generated as introduced in section I.D of chapter I.

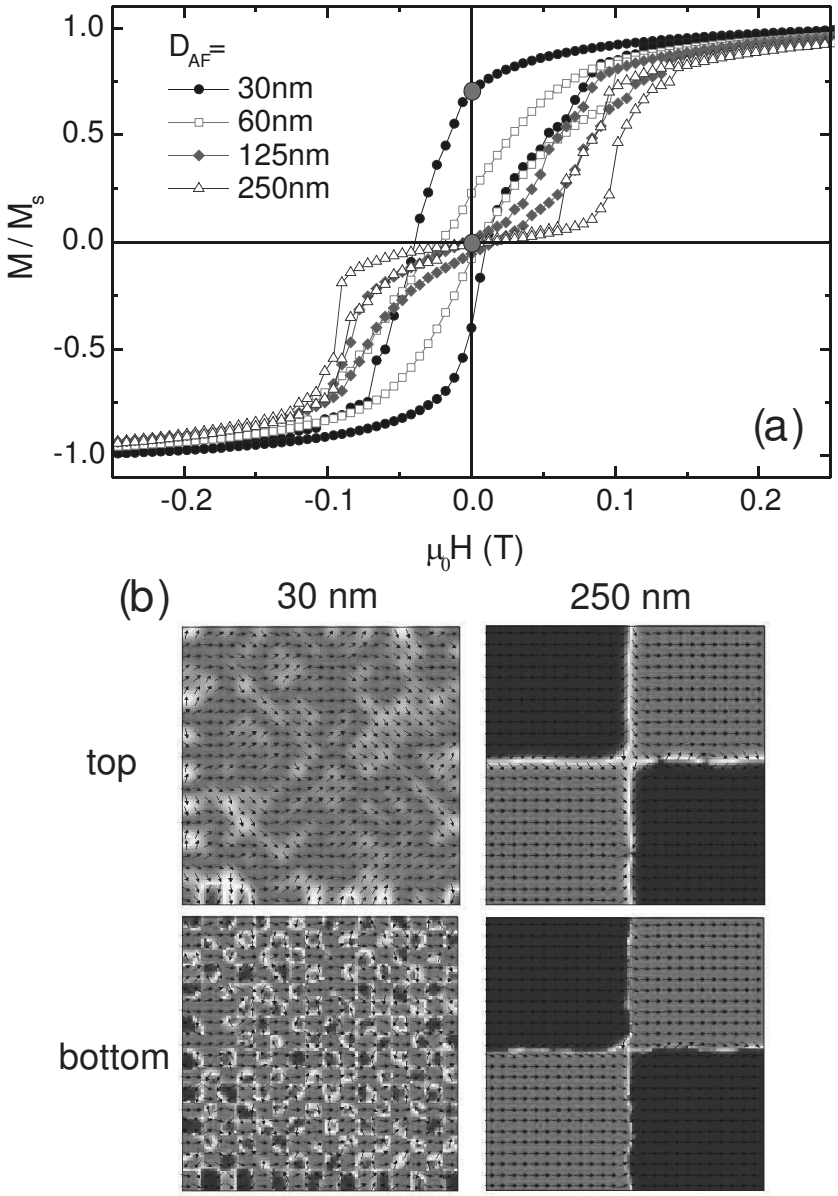

Figure II.15: (a) $M(H)$ from simulations of a Ni layer, where a constant random-site field acts on the bottom layer. Two opposite orientations of the random-site field are used with the domain size varied: D_{AF} = 30, 60, 125, and 250 nm as indicated in the legend. Lines are guides to the eye. (b) Spin structures of top and bottom layer at $H = 0$ (red circles in (a)) for D_{AF} = 30 and 250 nm. The color code 'light gray-white-dark gray' indicates 'positive-zero-negative' magnetization along the easy axis.

(Fig. II.16(b)). When the exchange bias is zero, the coercivity of the system reaches a maximum, as found experimentally in Ref. [60] (Fig. II.16(c) similar to Fig. II.2).

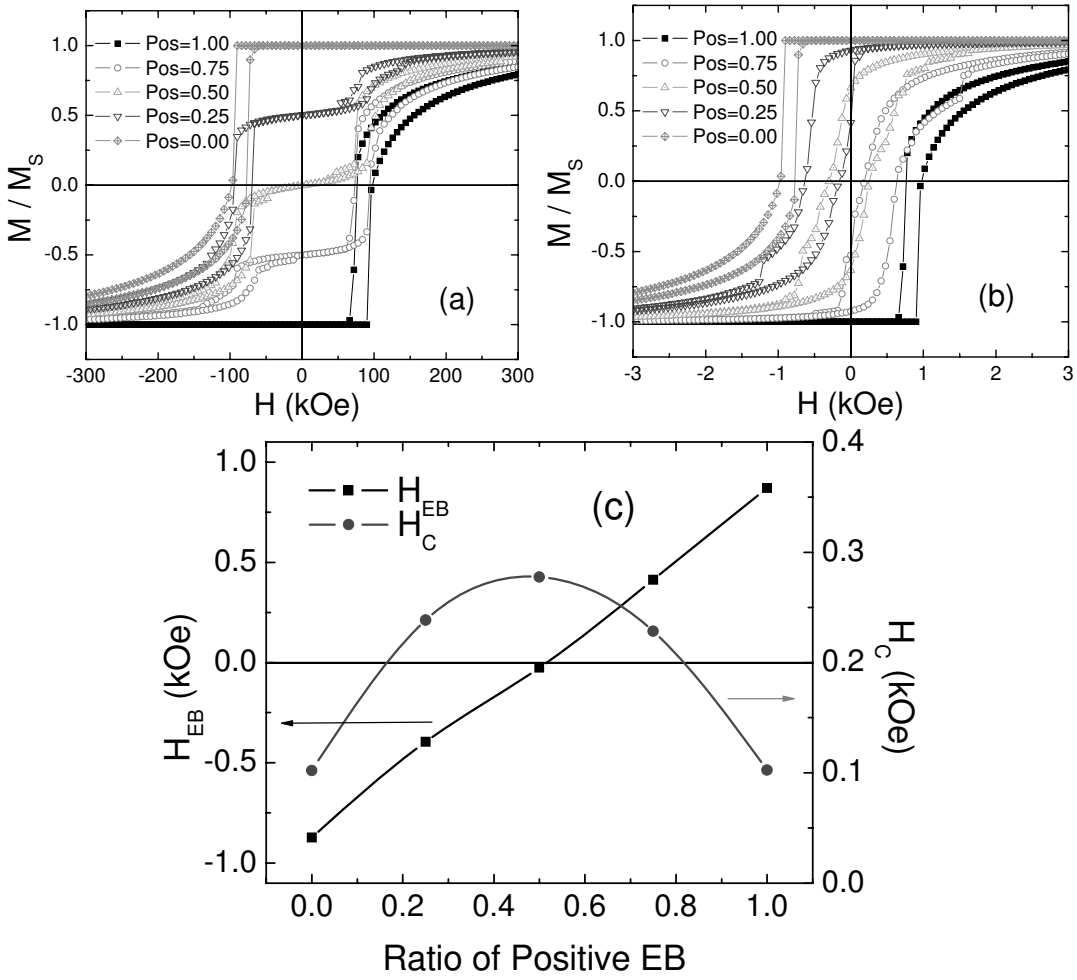

Figure II.16: (a, b) $M(H)$ from simulations of a Ni layer coupled to an AF pinning layer with domain sizes (a) $D_{AF} = 250$ nm and (b) 30 nm. The coverage of positive biased regions is varied as 100% (diamond), 75% (upside-down triangles), 50% (triangles), 25% (circles), and 0 (squares). Lines are guides to the eye. (c) Exchange bias field (squares) and coercivity (circles) vs. coverage of positive biased regions when $D_{AF} = 30$ nm.

This proves our speculation of how the lateral length scale relevance gives rise to either single or double hysteresis. In case of small AF domain sizes compared with the FM domain wall width, the FM senses an averaged exchange bias field, and a single hysteresis with an enhanced coercivity was found in the simulation.

In the opposite limit with the AF domain size much larger than the FM domain wall width, the system behaves like independently exchange biased samples put side by side, and a double hysteresis loop was found. This suggests that FeF_2 on MgF_2 and MgO substrates indeed correspond to large and small AF domains, respectively, resulting in double and single hysteresis, respectively.

II.G Summary

In this chapter, doubly shifted hysteresis in untwinned-FeF_2/FM systems grown on MgF_2 substrate was discussed. The occurrence of double hysteresis loops suggests the coexistence of both biasing directions in the AF. Methods to create double hysteresis loop in this system fall into two categories: First, imprinting FM domains onto the AF; second, the AF spontaneously breaks into subsystems during the cooling process. It is surprising that these two totally different ways of creating double hysteresis loops give nearly identical the same shape and temperature evolution, suggesting similar underlying AF domain structures. The FM domain imprinting was achieved by zero field cooling the system when the FM in a remanent state. When the FM is fully demagnetized, FM domains form and the orientation of FM spins in each domain locally determines the sign of the exchange bias, which gives rise to double hysteresis loop. This was confirmed by our spatially resolved MOKE measurement. Spontaneous breakdown of the AF into domains was achieved by cooling down the system at intermediate cooling fields, above or below which only positive or negative EB was found. This can be also achieved by first cooling down at a small cooling field that gives a negative bias, then warming up to around the Néel temperature of the AF, and finally cooling down at a large cooling field which would usually correspond to positive bias.

The spontaneous breakdown of the AF into domains has been proposed before [60], to account for the gradual shift of exchange bias from negative to positive with increasing cooling fields in twinned FeF_2/FM systems, and concommitent

coercivity enhancement when $H_{EB} = 0$. The difference between this case and double hysteresis loop found in FC lies in the averaging and lack thereof among AF domains due to different AF domain sizes.

This hypothesis is confirmed both experimentally by patterning the FM probing the AF domain size, and micromagnetic simulation. Patterning the FM into small structures leads to strong changes in the cooling field dependence of exchange bias. The lower limit of cooling fields necessary for positive exchange bias in patterned structures is an order of magnitude smaller than that of unpatterned ones when FeF_2 is untwinned. In samples with twinned FeF_2, increasing cooling fields leads to a larger increase of exchange bias field in smaller dots. This behavior is attributed to the relevance of the FM dot size with the antiferromagnet domain size. Rough stimate gives AF domain size in untwinned FeF_2 around 500 nm, much larger than the domain wall width of Fe, Ni, and Co.

In the simulation, both the AF domain size and coverage ratio of positive/negative AF domains are varied. The result nicely reproduced most of experimental features. For FM domain wall width around 40 nm in the simulation, transition from single to double hysteresis loop was found when the AF domain size is varied from 30 nm up to 250 nm. Enhanced coercivity was also found in systems with AF domains of 30 nm. The above result shows that lateral length scale relevance is a key aspect in understanding the interaction of two dissimilar materials coupled together. In the next chapter, the influence of the length scale on the asymmetric magnetization reversal will also be discussed.

II.H Acknowledgement

Chapter II, in part, is a reprint of the material as it appears in Oleg Petracic, Zhi-Pan Li, Igor V. Roshchin, M. Viret, R. Morales, X. Batlle, and Ivan K. Schuller, "*Bi-domain state in the exchange bias system FeF_2/Ni*," Appl. Phys. Lett. **87**, 222507, © 2005 American Institute of Physics, where the dissertation

author was the second author, Igor Roshchin, Oleg Petracic, Rafael Morales, Zhi-Pan Li, X. Batlle and Ivan K. Schuller, "*Lateral length scales in exchange bias*," Europhys. Lett., **71**, 297, © 2005 Institute of Physics, where the dissertation author was the fourth author, and Justin Olamit, Elke Arenholz, Zhi-Pan Li, Oleg Petracic, Igor V. Roshchin, R. Morales, X. Batlle, Ivan K. Schuller, and Kai Liu, "*Loop Bifurcation and Magnetization Rotation in Exchange Biased Ni/FeF_2*," Phys. Rev. B **72**, 012408, © 2005 The American Physical Society, where the dissertation author was the third author. The co-authors in this publication directed, supervised, and co-worked on the research which forms the basis of this chapter.

III

Asymmetric Magnetization Reversal

III.A Introduction

In most magnetic systems, the time reversal symmetry is manifested by a symmetric magnetization curve relative to the origin. This symmetry also requires identical magnetization reversal processes between positive to negative saturation. However, in a FM/AF system, exchange bias (EB) develops below the AF Néel temperature T_N producing a shift (H_{EB}) of the hysteresis loop along the magnetic field axis [1]. Therefore, with the shift breaking the time reversal symmetry, magnetization reversal symmetry is no longer required. In fact, asymmetric reversal was observed by polarized neutron reflectometry (PNR) [5], photoemission electron microscopy (PEEM) [40], magneto-transport [41], magneto-optical indicator film (MOIF) [43], and magneto-optical Kerr effect (MOKE) [44]. In some systems the reversal along the decreasing branch is dominated by transverse magnetic moments, a phenomenon that was interpreted as due to coherent magnetic rotation. The absence of transverse moments in the increasing branch reversal was interpreted as domain wall propagation [5, 40]. Different, even opposite scenarios were also found [44, 45], for example, asymmetrically kinked hysteresis [46], train-

ing induced reversal asymmetry [47], etc. With the well established experimental evidence, theoretical models using Monte-Carlo simulation [48], Stoner-Wolfarth calculation [49], or micromagnetic simulation were also proposed [50]. The most convincing argument thus far has been the competition of uniaxial and unidirectional anisotropies [49], but how they compete with each other and result in the reversal asymmetry was still not clear. The origin of the magnetization reversal asymmetry in exchange bias systems remains a controversial and highly debated issue, and a unified and general understanding is lacking. On the other hand, the hotly debated issue over the asymmetric reversal process over the past 5 years solely focused on lateral FM domains. FM parallel domains were predicted [16, 17]. However, they were not confirmed experimentally. They were mostly ignored in microscopy studies [40] and simulations generally assuming the FM to be a single moment [49] or one monolayer [48]. This situation may be mostly due to the weak coupling at the FM/AF interface, and limitations of different experimental and modeling techniques. This situation is further complicated by the lack of knowledge of the interface, crystal imperfections, complex FM and AF anisotropy energies, and training effect. While these factors are important for each individual system, the fundamental connection of the reversal asymmetry to the broken symmetry intrinsic in the inhomogeneous system is overlooked.

In this chapter, I will address two key mechanisms for asymmetric magnetization reversal. When the unidirectional anisotropy dominates the uniaxial anisotropy, using vector magnetometry and micromagnetic simulation, we found that the FM reverses by winding and unwinding incomplete domain walls parallel to the interface, which leads to highly asymmetric hysteresis loops (Section III.B)[93]. To further confirm these observations, Py (70 nm) / FeF_2 (70 nm) was measured by magneto-optical Kerr effect (MOKE) from the front and back side of the sample (through the optically transparent substrate and AF), noting the skin depth of the HeNe laser in Py is about 30 nm. Probing the FM/AF interface yields a more gradual and asymmetric reversal than the FM/air surface. The dif-

ference of the MOKE hysteresis from two interfaces decreases as the FM is changed from Py to Ni and Fe with decreasing FM domain wall widths, and disappears as the sample were heated above T_N. Our recent polarized neutron scattering experiments show reduced FM moments near the interface [59], which could be well accounted by the incomplete FM domain wall. All the experimental evidence and simulation unambiguously shows the existence of a FM parallel domain wall and its importance in asymmetric magnetization reversal.

However, the experimentally observed reversal asymmetry between coherent rotation and domain wall motion [5, 40] arises from the cooperation and competition between the unidirectional and uniaxial anisotropies of comparable magnitudes (Section III.D). For the decreasing field branch, these two anisotropies cooperate with each other, and the FM reveres by enhanced rotation, while for the reverse branch, they compete with each other and result in frustrated rotation, or domain wall motion. By micromagnetic simulation, we clearly demonstrated this behavior from the evolution of the spin configuration with the magnetic field.

Lateral length scales also plays an important role in the asymmetric magnetization reversal (Section III.E). It has been observed in FeF_2/Fe systems that the asymmetric relative peak heights of the transverse magnetic component in reversal are sensitive to the sample's alignment with the magnetic field. For example, for a certain alignment, the transverse component only shows in the decreasing field branch. After rotating the sample by only 5 degree, the decreasing field branch shows zero transverse component, while there is a significant transverse peak in the increasing field branch [97]. While the literature has attributed this behavior to the existence of a large 4-fold anisotropy, we believe that this is due to the small AF domain size compared with the FM domain wall width.

Asymmetric magnetization reversal in nanostructured exchange bias systems was also studied (Section III.G and III.H) [44, 92]. Magneto-static interaction was found to be crucial to asymmetric reversal mechanisms in patterned structures [44]. When the dot geometry favors the formation of vortex, exchange bias field

also decreases [92].

III.B FM Local Incomplete Domain Wall

In this section, by investigating a simple model system using a variety of experimental techniques combined with numerical simulations, we establish a critical link between magnetization reversal asymmetry and the time reversal asymmetry in these systems. Namely, the observed asymmetry originates from *local incomplete domain walls* parallel to the interface when the FM reverses to negative saturation. Magneto-optic Kerr effect (MOKE) unambiguously confirms such an asymmetric reversal and a depth-dependent FM domain wall in accord with the magnetometry and simulations.

FeF_2/(Ni, Py) bilayers were prepared for this study. As mentioned earlier, FeF_2 has a large uniaxial anisotropy $K_u = 1.35 \times 10^4$ kJ/m^3 along [001] direction, hence can be considered as a model Ising system [61, 62], with the AF spins frozen along [001] at low temperatures [63]. The Ni or Py ($Ni_{81}Fe_{19}$) is polycrystalline with a negligibly small crystalline anisotropy, except for a small growth-induced uniaxial anisotropy along FeF_2 [001] [55]. This system is thus in close approximation with simple theoretical assumptions.

Vector vibrating sample magnetometry (VSM) of FeF_2 (50 nm) / Ni (21 nm) / Al (7.6 nm) was used to measure the in-plane longitudinal (parallel to the magnetic field) and transverse (perpendicular to the magnetic field) magnetic moments [79, 98]. The magnetic field is applied along the FeF_2 easy axis [001] with a small misalignment that defines the sign of the transverse component during reversal [79, 97]. Square hysteresis loops are found above T_N along [001] [55]. Cooling the sample in a field H_{FC} = 2 kOe from T = 150 K to 15 K yields an EB field H_{EB} = -1 kOe (Fig. III.1a) and virtually no coercivity. Both longitudinal and transverse hysteresis loops exhibit a clear asymmetry. Starting from positive saturation, the reversal occurs with a sharp corner in the longitudinal component

and an abrupt increase in transverse component to over 75% of the saturation magnetization. Then the FM *gradually* approaches negative saturation, evidenced by the long tail in both components. A significant non-zero transverse component is found even at H = -5 kOe. In the increasing field sweep, Ni is saturated almost *immediately* after the reversal. The asymmetry of the two FM orientations, especially the long tail around negative saturation, is key to understanding the asymmetric reversal.

We modeled the asymmetric reversal process with micromagnetic simulations [70] using a 20 nm thick Ni layer with lateral size 500×500 nm^2, discretized into 5×5×2 nm^3 cells. The Hamiltonian $\mathcal{H}$ of the system is given by,

$$\begin{aligned}\mathcal{H} =& A \sum_{i\in\{FM\}} [(\nabla \widehat{m}_{ix})^2 + (\nabla \widehat{m}_{iy})^2 + (\nabla \widehat{m}_{iz})^2]\Delta V \\ & - \sum_{i\in\{FM\}} (K_u \widehat{m}_{ix}^2 \Delta V + K_d \widehat{m}_{iz}^2 \Delta V + \vec{H}\cdot\vec{m}_i) \\ & - J_{FM/AF} \sum_{i\in\{Interface\}} \vec{m}_i \cdot \vec{\sigma}_i,\end{aligned}$$

where the three summed terms include FM exchange energy, FM anisotropy and Zeeman energy, and FM/AF interfacial interaction, respectively. The AF is assumed to be frozen during the hysteresis cycle, thus its energy contribution remains constant and is not considered in the Hamiltonian above. $\vec{H}$ is the magnetic field applied along the $\hat{x}$ axis with 0.5° misalignment similar to the experiment. $\vec{m}_i$ and ΔV are the magnetic moment and volume of each cell, respectively. The reduced moment $\widehat{m}_i$ is defined by $\widehat{m}_i = \vec{m}_i/M_S$. Micromagnetic parameters of Ni used here are tabulated in Table A.2. The small growth-induced anisotropy of the Ni layer is taken into account by a uniaxial anisotropy along the $\hat{x}$ axis with $K_u = 5$ kJ/m^3 obtained from measurements along the hard axis above T_N. The dipolar interaction is approximated by a shape anisotropy along the $\hat{z}$ axis (out-of-plane) with $K_d = -(\mu_0/2)M_S^2 = -150$ kJ/m^3, which keeps the moments in the sample plane and avoids boundary effects.

The AF is modeled by a monolayer of spatially inhomogeneous frozen moments, $\vec{\sigma}_i$, exchange coupled to the bottom layer of the FM with an adjustable interfacial coupling from $J_{FM/AF} \sim J_{AF} = -0.45$ meV up to $2J_{AF}$ [61] (Table A.3). We introduced AF grains of average size 25×25 nm^2 to simulate the inhomogeneous interfacial coupling [72]. $\sigma_i = -\alpha_i S_i^{AF} p_j$ with $S_i^{AF} = 2$, consists of two random quantities: α_i denoting the *intergrain* variation, and p_j the *intragrain* variation. α_i varies as 1 ± 0.35 between grains, while p_j varies as $(7\pm2)\%$ between cells. This 7% assumption is based on recent experiments which found net frozen AF interfacial moments with about 4% [37] or 7% [38] coverage that contribute to EB. Crucial parameters for the simulation include the product of the uncompensated moment coverage and interfacial coupling, and intergrain fluctuation. The former defines the effective coupling strength. The latter describes the interfacial inhomogeneity modulated over a length scale of the grain size (25 nm), comparable with the FM domain wall width 82 nm. This spatial modulation of σ_i leads to an inhomogeneous pinning on the FM, and is essential to explain reversal process revealed in the experiment. However, the intensity of the modulation is not essential: 20% to 50% standard deviation in α_i gives similar results. The resultant spatial variation of σ_i is shown in the inset of Figure III.1.

The simulation (Fig. III.1) matches well both the longitudinal and transverse hysteresis loops exhibiting the same asymmetry as the experiment [99]. The bottom and side view of the FM spin configuration during the hysteresis (Figure III.2) shows domains evolving both laterally and in the depth. In positive saturation, the FM is uniformly magnetized throughout the thickness because both the applied magnetic field and interfacial coupling favor this orientation. As the magnetic field decreases, the reversal is initiated from the top of the FM far away from the interface while the bottom pinned by the AF remains in the positive direction. An incomplete (non-180°) FM domain wall (IDW) is thus formed parallel to the interface. As the field decreases further, these FM IDWs slowly shrink laterally and squeeze close to the interface. Even at H = -8 kOe, the FM is not

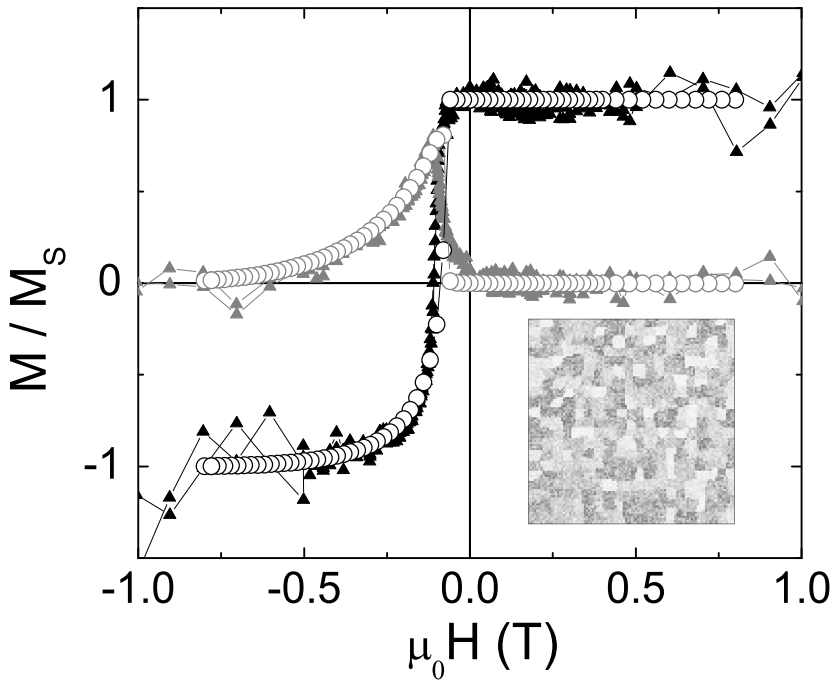

Figure III.1: (a) Vector VSM measurement (solid symbol) and micromagnetic simulation (open symbol) of FeF_2(50 nm)/Ni(21 nm) at 15 K after field cooling in a 0.2 T field. Both longitudinal and transverse components are measured and simulated. The micromagnetic simulation was performed assuming the FM interfacial layer is coupled to spatially inhomogeneous uncompensated frozen AF spins, whose distribution is shown in the inset (500×500 nm^2). The gray scale refers to the magnitude of local uncompensated frozen AF moments with white corresponding to zero local density.

saturated at some interface regions. This lateral domain formation is the result of the spatially varying σ_i. The regions in the FM most resistant to reversal are where the strongest local interfacial pinning is found. As the field increases, these regions become nucleation sites for the development of *local* IDWs both laterally and in the depth. Therefore, these local IDWs result from the competition between inhomogeneously distributed interfacial pinning and the magnetic field. Due to the unidirectional nature of the AF pinning field, it only competes with the Zeeman energy in approaching negative saturation, while they both stabilize the FM when positively saturated. This simulation demonstrates that the local development of IDWs constitutes the dominant asymmetric reversal mode. Although similar exchange spring is claimed in hard/soft magnetic structures [29, 30], it does not lead to asymmetric reversal [100]. In addition, this incomplete domain wall is unusual in EB because the interfacial coupling energy is much weaker than that in a conventional exchange spring, thus it was never convincingly observed and was overlooked in most EB studies.

When a finite anisotropy of pinned AF moments is included in the simulation, the IDW is pushed into the AF forming a hybrid domain wall across the interface, but the main features of the reversal process remain unchanged. Since the anisotropy of the FM is usually much smaller than that of the AF, the FM-side of domain wall dominates the reversal.

The result implies several important features of the local IDW reversal process. First, the FM domain wall depth-dependence is crucial for the asymmetric reversal process. An important signature of this behavior is the asymmetric development of transverse magnetic moments. This behavior tends to be smeared out by AF twinning or polycrystallinity, and/or more complicated FM or AF anisotropy energy terms. It is worth noting that this asymmetry of approaching two saturated states may seem different from the asymmetry of two field sweep branches observed before in other systems, where a sharp corner is found in the decreasing branch and a rounded one for the increasing one [44, 41]. However, they are essentially

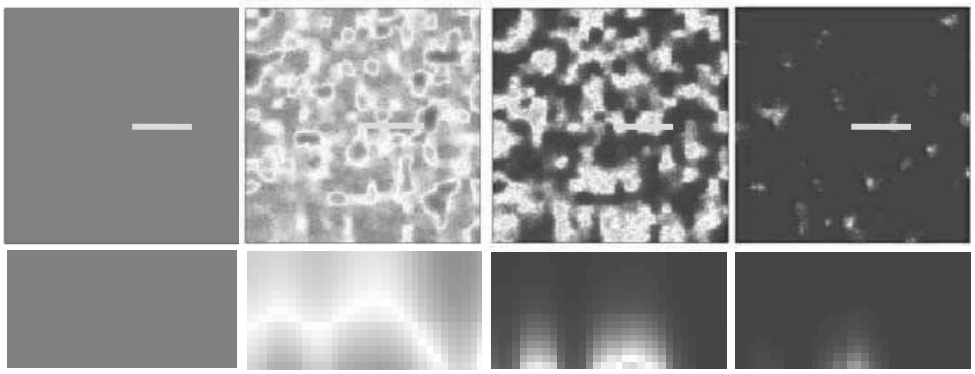

Figure III.2: Images in the first row from left to right are the simulated FM spin configurations (500×500 nm^2) at the FM/AF interface at 0.8, -0.08, -0.36, and -0.8 T, respectively; the second row shows the simulated FM depth profiles (125×20 nm^2), the bottom edge referring to the FM/AF interface) for the same corresponding field cross sectioned at the thick gray lines. black, white and dark-gray corresponds to M_x/M_s = 1, 0, -1, respectively, with x being the magnetic field direction.

the same except for the small FM uniaxial anisotropy, thus negligible coercivity in our system. If the FM uniaxial anisotropy is increased to K_u = 50 kJ/m^3 and a 0.5° fanning of the AF pinning moment in the sample plane is included, the simulated hysteresis loop displays the same asymmetry as observed before together with an irreversible transverse loop (Fig. III.3) [44, 41]. Second, the *local* nature of the IDW due to the interfacial inhomogeneity is crucial in the model. It leads to asymmetric lateral domains due to unsynchronized winding of DW in the depth, and may clarify the present confusion and debate based on lateral multi-domain observations. It also explains the long tail of the hysteresis loops, which would otherwise disappear if α_i is not included as in Kiwi's model (Fig. III.3 inset) [16]. Since a square hysteresis loop is observed above T_N, this low temperature behavior must arise from the interfacial inhomogeneity.

So far we demonstrated that the local IDWs nucleated in approaching the negative saturation cause the asymmetric reversal. This result is unambiguously confirmed by MOKE experiments probing the FM-air and FM-AF interfaces independently. In this experiment, a sample with MgF_2 (110) / FeF_2 (50 nm) / Py

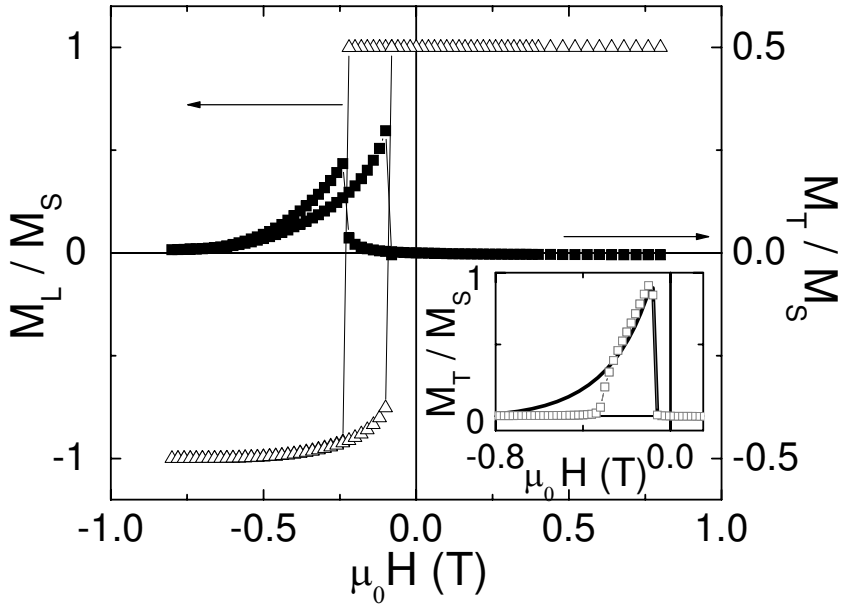

Figure III.3: Simulation of the longitudinal (open symbols) and transverse (filled symbols) hysteresis loop considering 50 kJ/m^3 in-plane uniaxial anisotropy and 0.5° fanning of AF uncompensated moment orientation. (Inset) Simulated transverse hysteresis loops with uniform (open symbols) and inhomogeneous (thick black line) interfacial coupling.

(70 nm) / Al (4 nm) is cooled below T_N in $H_{FC} = 0.2$ kOe, and MOKE is performed on both the top and bottom surfaces of the sample with HeNe laser ($\lambda = 632.8$ nm) at 45 degree incidence (Fig. III.4 inset (c)). Probing the depth dependence of the FM domain structure is possible because the 28 nm penetration depth of the light [68] is less than half of the Py thickness, and both MgF_2 and FeF_2 are transparent. A clear difference is seen between the two MOKE measurements (Fig. III.4). Probing the FM-AF interface shows a much more rounded and longer tail compared with the one from FM-air interface, confirming the existence of domain structures in the depth. The sample was also measured using SQUID magnetometry to which the entire sample contributes equally. The resultant hysteresis loop lies between the two MOKE loops.

We also performed micromagnetic simulations under identical assumptions using the same parameters as above to generate the random frozen AF moments [101]. Fig. III.5 shows the hysteresis loop of each discretization layer in the

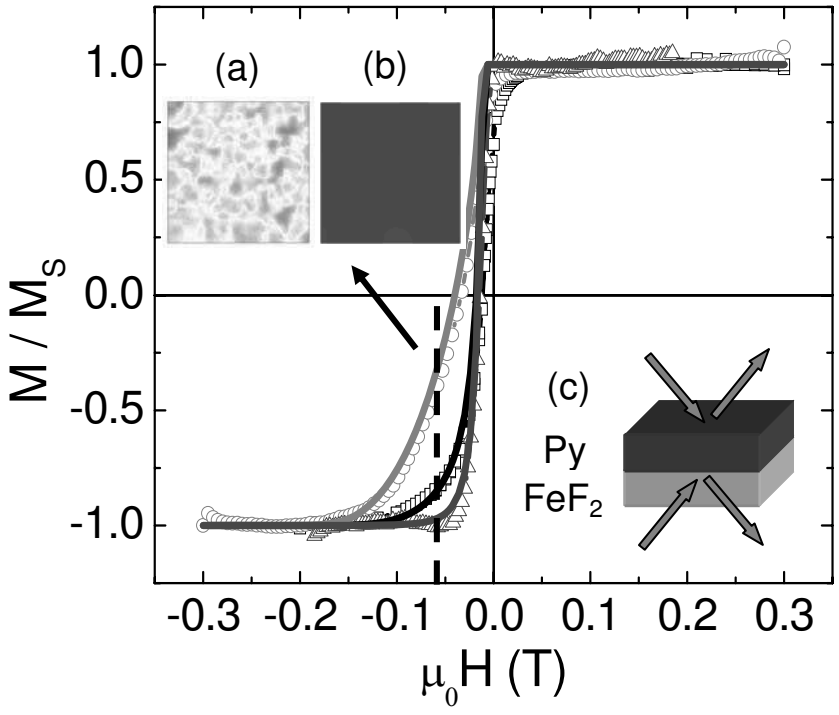

Figure III.4: Experiment (open symbol) and micromagnetic simulation (solid line) on FeF_2 (70 nm) / Py (70 nm) at 10 K after field cooling in a 0.02 T field. Experimental curves obtained from MOKE measurement from the FM-air (triangle) and FM-AF (circle) interface and SQUID magnetometry (square). The schematic of the MOKE experiment is shown in inset (c). The upper-left inset shows the simulated FM spin configuration (500×500 nm^2) at the FM-AF (a) and FM-air (b) interface at $H = -0.6$ kOe.

depth (10 layers in total). The hysteresis becomes more and more asymmetric as it approaches the FM/AF interface, and the extended tail around negative saturation becomes more and more pronounced. The exponential decay of MOKE in the FM is simulated by giving each FM discretization layer in the depth an appropriate weight according to the Py 28 nm penetration depth. A very good agreement is obtained for all three hysteresis loops simultaneously with a slight adjustment of the interfacial coupling [102]. At H = -0.6 kOe, a large difference between the two MOKE measurements is observed. The simulated spin configuration at this field shows that the FM close to the FM-AF interface is only partially reversed forming lateral domain patterns, while at the FM-air interface the FM is fully reversed (inset (a) and (b) of Figure III.4). This confirms that the local IDW model leads to asymmetrically rounded hysteresis loops. A reduced magnetization near the interface was also observed in our latest neutron scattering experiment, which will be published elsewhere.

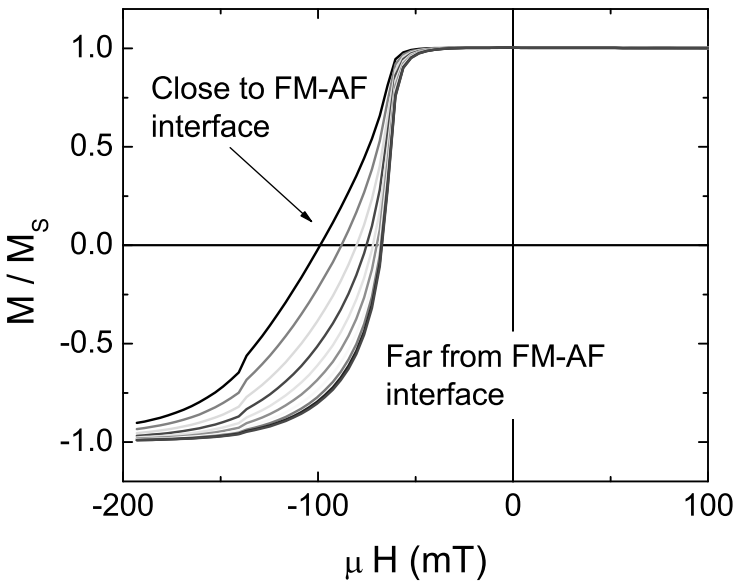

Figure III.5: Simulated M vs. H hysteresis loops of different discretization layers in the depth (10 curves in total). The topmost and bottommost curves are the ones closest and farthest to the interface with the pinning layer, respectively.

In summary, we found strongly asymmetric hysteresis loops in a simple model exchange bias system untwinned-FeF_2/(Ni, Py). By combining vector magnetometry, MOKE with micromagnetic simulation, we clearly showed that the asymmetric reversal directly results from the FM domain structure in the depth due to the broken symmetry at the interface. The hotly debated issue over the asymmetric reversal process over the past 5 years solely focused on lateral FM domains, and its origin was controversial until now. FM parallel domains were predicted [16, 17]. However, they were not confirmed experimentally. They were mostly ignored in microscopy studies [40] and simulations generally assuming the FM to be a single moment [49] or one monolayer [48]. This situation was mostly due to the weak coupling at the FM/AF interface, and limitations of different experimental and modeling techniques. Dispersions in AF crystallinity and anisotropy also smear out manifestations of parallel domain walls. Our study of a simple EB model system, combining different experimental and simulation techniques, unambiguously demonstrates the presence of such domains and their dominant role on the asymmetric reversal. Further research involves Monte-Carlo simulation to study how detailed AF structures lead to pinned interfacial moments, and the FM incomplete domain wall [103].

III.C Comparison of FeF_2/(Fe, Ni, Py)

In order to further confirm that the difference between the two hysteresis loops from two sides of substrates indeed arises from the FM parallel domain walls, samples with Fe and Ni as the FM instead of Py were also similarly deposited and measured by MOKE and SQUID. Since the domain wall width of Fe and Ni are smaller than that of Py [104], smaller differences should be expected between the MOKE hysteresis measured from the front and back side the sample. When heating up to above T_N of the AF, the difference should dissapear. In addition, the reversibility of the magnetization has also been studied by SQUID minor hysteresis

loops. All samples exhibit a well defined uniaxial anisotropy above T_N with the easy axis along FeF_2 [001], in the sample plane.

The sample with largest crystalline anisotropy, FeF_2/Fe bilayer, exhibits virtually no difference in SQUID and MOKE loops measured on both FM interfaces at 10 K, revealing no evidence of depth-dependent magnetic structure [Fig. III.6(a)]. The reversal from positive to negative saturation is abrupt and irreversible as shown by open minor loops [Fig. III.6(b)]. This transition can be understood in terms of nucleation of inverse domains and propagation of domain walls perpendicular to the interface. An illustration of the magnetization depth profile just beyond the coercivity along the decreasing branch, at $H = -150$ Oe, is sketched in Fig. III.7 (a), where all Fe magnetic moments are aligned along the easy axis.

Different behavior was found in FeF_2/Ni bilayers (Fig. III.8). MOKE loop from Ni/air interface is square and symmetric, similar to the FeF_2/Fe case. However, the one from the FeF_2/Ni interface is asymmetric with an abrupt switching from positive saturation and a gradual tail extending to negative saturation (Fig. III.8 (a)). SQUID hysteresis loops show a similar asymmetry, and lie between the two MOKE loops. However, the difference among the MOKE and SQUID measurement is not as significant as in Py/FeF_2 sample shown in the previous section. This is consistent with our expectation that the difference between the two MOKE hysteresis lies in the FM parallel domain wall.

Minor loops (Fig. III.8 (b)) show the magnetization reversal involves two different processes. The rounded part at negative fields is reversible, while the jump around the coercive field is irreversible. Coming from positive saturation, the magnetization reversal starts at $H = -200$ Oe, likely by nucleation and propagation of domain walls perpendicular to the interface. At -300 Oe the upper part of the Ni layer (far from the AF) is fully negatively saturated, as indicated by the MOKE loop on the FM/air interface. However, the MOKE signal from the FeF_2/FM interface shows the FM is not yet saturated, and thus an in-depth

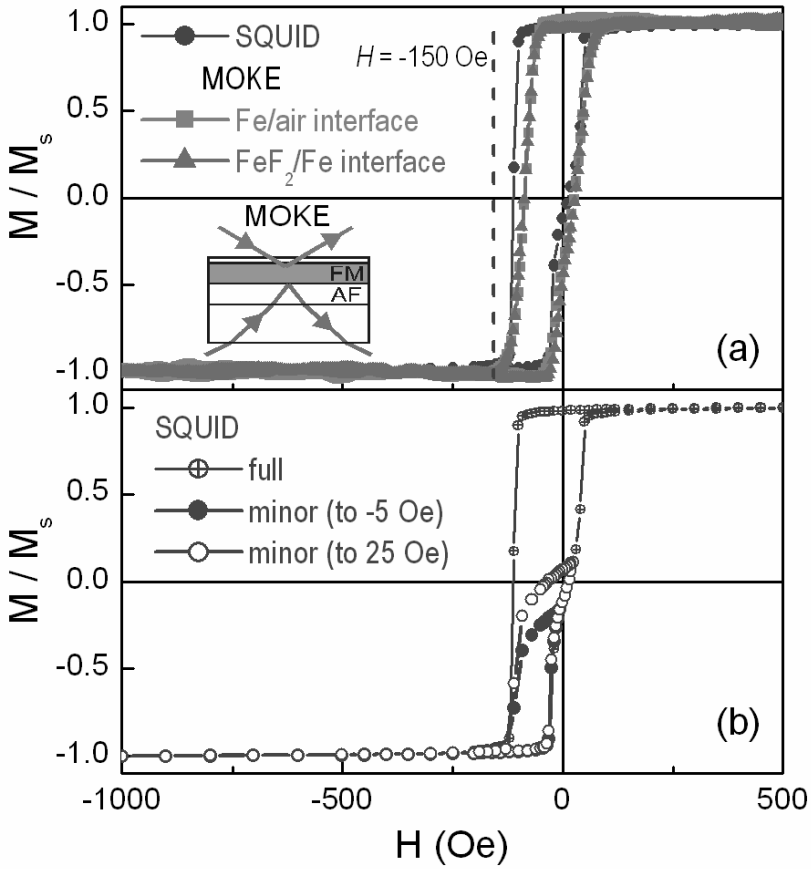

Figure III.6: FeF_2/Fe hysteresis loops at 10K. (a) SQUID and MOKE on both Fe interfaces. (b) Minor loops by SQUID.

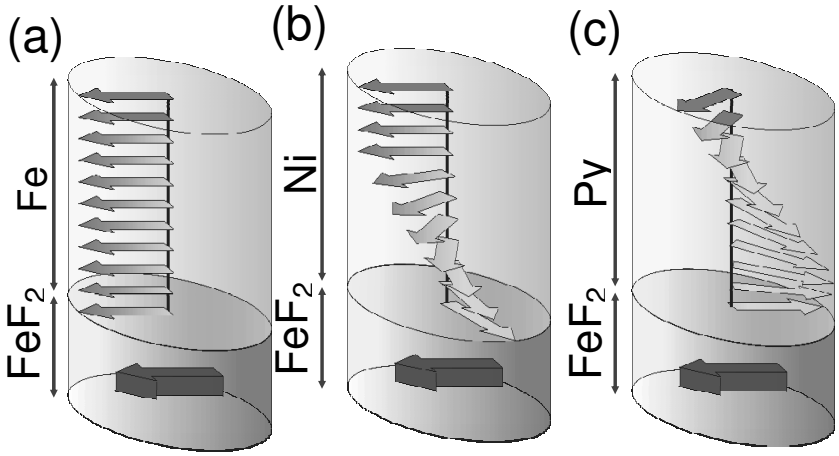

Figure III.7: Depicted profile of the magnetization in the FM layer at 10K for (a) FeF_2/Fe at $H = -150$ Oe (b) FeF_2/Ni at $H = -300$ Oe. (c) FeF_2/Py at $H = -140$ Oe. (The AF/FM coupling is antiferromagnetic).

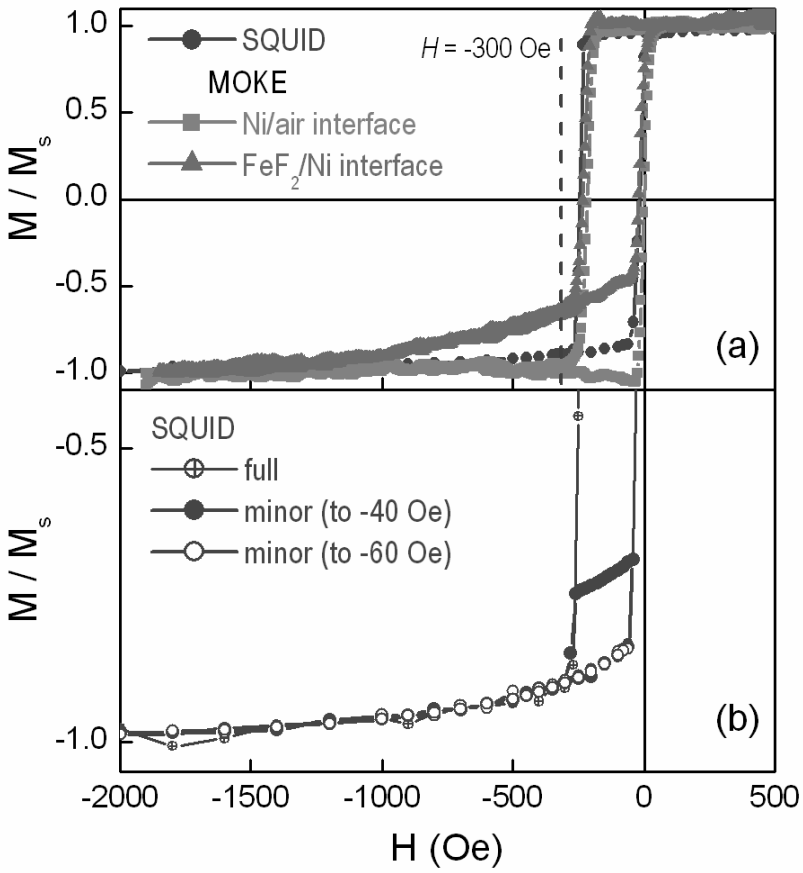

Figure III.8: FeF_2/Ni hysteresis loops at 10K. (a) SQUID and MOKE on both Ni interfaces. (b) Minor loops by SQUID.

domain structure has been created. A possible macroscopic scenario of this domain structure is a spring-like domain wall, as sketched in Fig. III.7 (b) where a magnetic structure extends from Ni spins antiferromagnetically coupled to the AF [72] toward the upper part of the Ni layer where all spins are inverted. Since the penetration depth of light is about 30 nm and the thickness of Ni is 70 nm, the spring domain wall should span less than 40 nm. A typical Bloch wall width in Ni is about 80 nm, [73] therefore, this spiral-like structure is an incomplete domain wall (IDW), i.e. a non-180° wall. This is in qualitative agreement with Kiwi's model, which predicts the existence of IDW in an exchange bias system with a compensated interface [16].

In contrast, as shown in the previous section, in materials with low magnetocrystalline anisotropy, such as Py in FeF_2/Py bilayers, there are no abrupt transitions in the M-H curves, and the difference between the two MOKE hysteresis is most pronounced (Fig. III.9 (a)). Decreasing the field from positive saturation, the MOKE signal from the upper side of the Py layer (Py/air) is always smaller than that from the FeF_2/Py interface, indicating that the incoherent rotation of the magnetization starts in the outmost layer of the Py thin film, and that these Py moments drag the magnetic moments underneath creating a spiral structure that extends to the AF/FM interface. For example, at $H = -140$ Oe, a spiral-like structure (Fig. III.7 (c)) extends throughout the 70 nm thick Py layer, with a null magnetic moment averaged on the upper part along the field direction due to the creation of an IDW. The existence of an IDW in this system is also consistent with the typical domain wall width of Py being around 100 nm [104], and is confirmed by vector VSM measurements. The VSM transverse magnetization loop (Fig. III.9 (a)) proves the reversal is by rotation. The magnitude of the transverse peak, with a maximum $\sim$95% of the total magnetic moment of the sample, demonstrates that the maximum angle between extreme spins in the spring-like wall must be smaller than 180°, hence being an IDW. Closed minor loops (Fig. III.9(b)) show that the reversal process of the IDW is fully reversible.

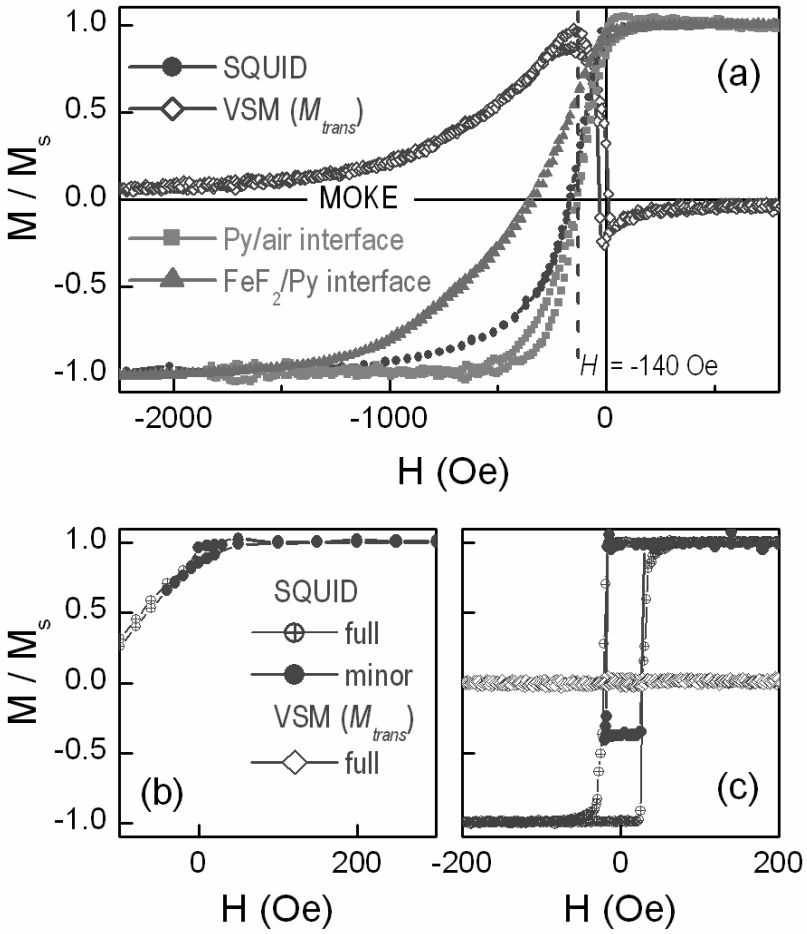

Figure III.9: FeF_2/Py hysteresis loops. (a) SQUID, transverse VSM and MOKE on both Py interfaces at 10K. (b) Minor loop by SQUID at 10K ($T < T_N$). (c) Minor loop by SQUID, and full transverse VSM loop at 90K ($T > T_N$).

The minor hysteresis loops of FeF_2/Py above T_N are different from those below T_N [Fig. III.9(c)]. At 90 K, the transition is abrupt and irreversible, with a finite coercivity, and the transverse component is null, typical of a magnetization reversal by nucleation and domain wall motion perpendicular to the interface, and quite different from the process below T_N, for which reversal takes place by incoherent rotation of magnetic moments parallel to the interface. This result proves that exchange bias can induce drastic changes in the magnetization reversal mechanism of a FM.

For all three FMs (Fe, Ni, Py), after warming up to above T_N, the difference between the two MOKE hysteresis loops disappear. This excludes the possibility that the difference is an artifact due to the laser going through the FeF_2 and MgF_2 substrates. Fig. III.10 summarizes all results, and unambiguously demonstrates that the FM incomplete domain wall is an important reversal mode in exchange biased systems, and can give rise strongly asymmetric hysteresis loops.

III.D Cooperation and Competition of Anisotropies

In the previous section, we showed that incomplete FM domain walls parallel to the interface play a significant role in asymmetric magnetization reversal. What remains unexplained is the experimental observation of coherent rotation or domain-wall-motion dominated reversal processes for decreasing and increasing field sweeps, respectively [5, 40]. This has been observed in different systems with relatively small exchange bias field, usually comparable with or smaller than the coercive field. Models have been proposed to explain this phenomenon as a result of competing uniaxial and unidirectional anisotropies [48, 49], but how their competition leads to the observed reversal asymmetry remains unclear. In this section, we show that uniaxial and unidirectional anisotropies cooperate with each other in the decreasing field branch, and results in enhanced rotation. For the increasing field branch, the two anisotropies compete with each other, and sup-

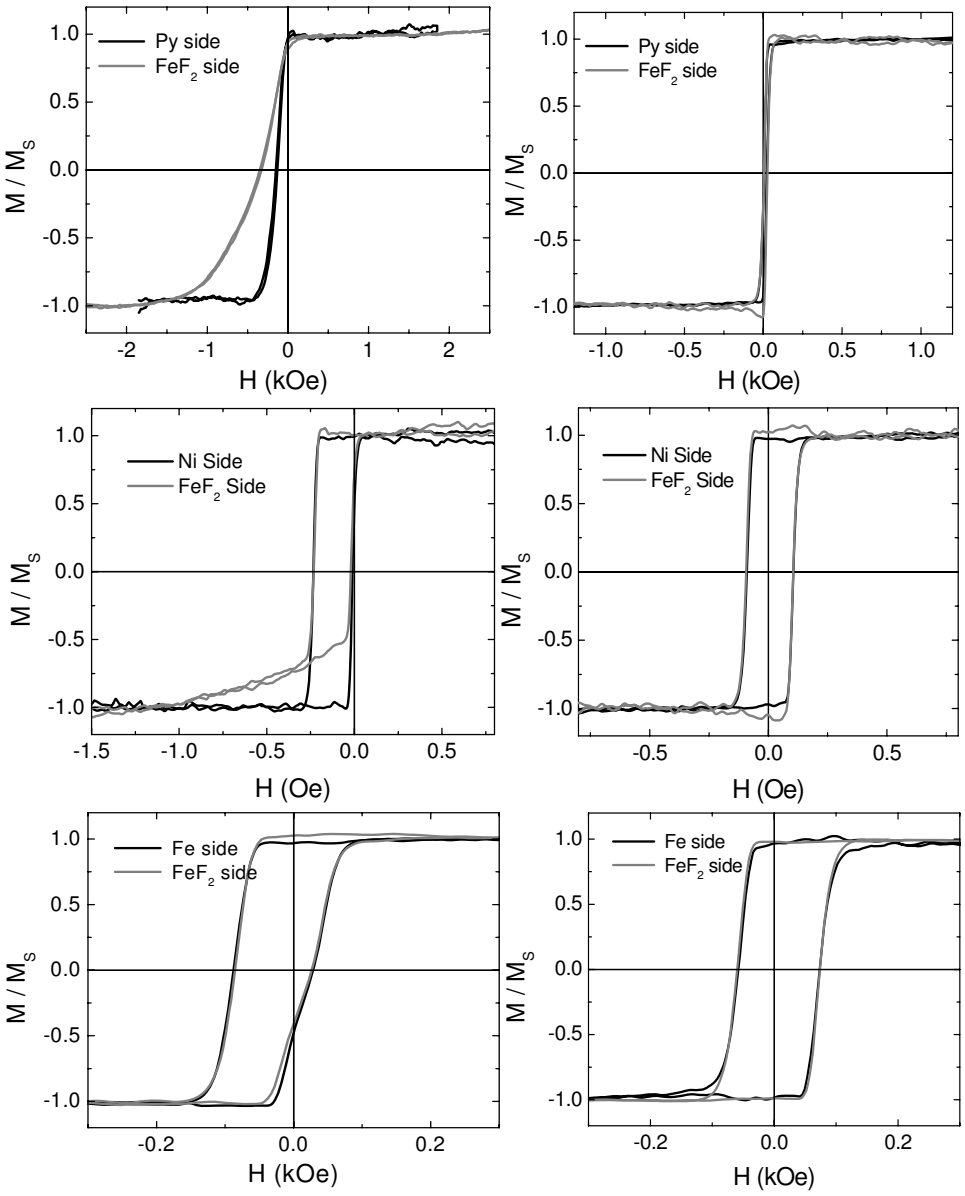

Figure III.10: Summary of MOKE hysteresis probed from the FM/air (black) and FM/AF (gray) sides for Py/FeF_2 (top panel), Ni/FeF_2 (middle panel), and Fe/FeF_2 (bottom panel) when $T = 10$ K (left panel) and $T = 90$ K $> T_N$ (right panel).

presses magnetization rotation. By micromagnetic simulation, we show that this suppressed rotation is manifested as domain formation and domain wall motion in inhomogeneous systems.

Similar micromagnetic simulation parameters are used as in the Ni simulation in Section III.B, except for the anisotropy and coupling parameters. In this case, the uniaxial anisotropy is $K_u = 10$ kJ/m^3, and the interfacial coupling is $\sim 0.45 J_{FeF_2}$, which is equivalent to unidirectional anisotropy 15 kJ/m^3. Easy axis of the uniaxial anisotropy and interfacial pinning field are parallel with each other, and the magnetic field is 5° misaligned with the pinning field. Dispersion in pinning field direction will be addressed in the next section. To simplify the problem, the case without interfacial inhomogeneity is considered.

When the FM is not exchange biased, and has only uniaxial anisotropy, a typical unshifted and symmetric hysteresis loop is obtained (Fig. III.11 (a)). The transverse component is negative and positive for decreasing and increasing field branches, respectively, symmetric with respect to the origin. The reversal process is sketched in Fig. III.13 (a). In a large enough magnetic field, FM moments are saturated along the field direction, away from the easy axis of the uniaxial anisotropy. It is worth noting that the anisotropy energy increases as FM moments rotate away from the easy axis, and reaches its maximum when they are perpendicular to the easy axis. Therefore, as the field decreases, FM spins rotates clockwise away from the field direction toward the easy axis. When the field further decreases to negative, FM spins continue to rotate clockwise with increasing negative transverse component. When the coercive field is reached, the anisotropy energy barrier is overcome by the magnetic field and FM moments snap to the field direction. When reversing from negative saturation, FM moments still rotate clockwise toward the closest of the two directions on the easy axis, resulting in a positive transverse component. Therefore, the misalignment between anisotropy easy axis and magnetic field causes FM spins rotate through different sides of the field, and results in transverse magnetization of different signs during the reversal.

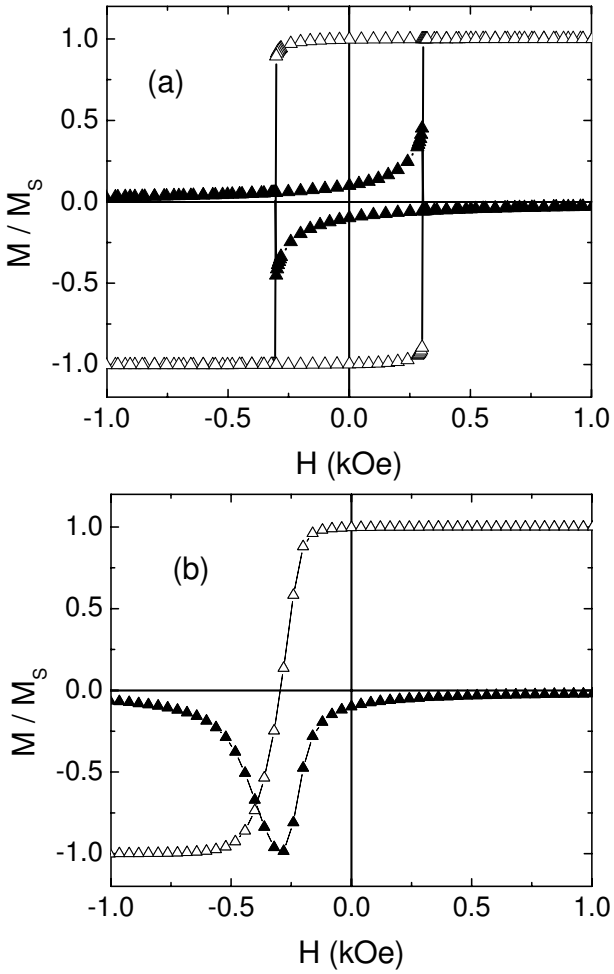

Figure III.11: Simulated magnetic hysteresis by micromagnetics when only (a) uniaxial or (b) unidirectional anisotropy is included. Longitudinal and transverse magnetizations are plotted in empty and solid symbols, respectively.

When the FM has only unidirectional anisotropy, a shifted non-hysteretic magnetization curve was found (Fig. III.11 (b)). In this case, since the anisotropy energy barrier resides opposite to the easy direction, FM moments always rotate through the easy direction on the same side of the magnetic field, and give rise to transverse component of the same sign for both field sweep directions (Fig. III.13 (b)).

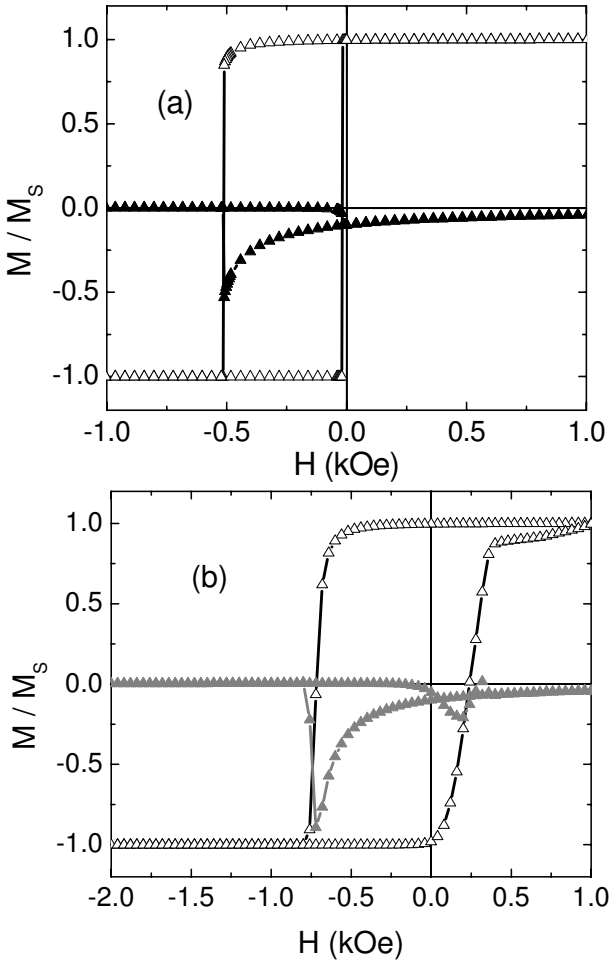

Figure III.12: Simulated magnetic hysteresis by micromagnetics when uniaxial and unidirectional (interfacial coupling) anisotropies coexist. (a) The interfacial coupling is spatially uniform. (b) The magnitude the interfacial coupling is spatially inhomogeneous, while its direction is uniform. Longitudinal and transverse magnetizations are plotted in empty and solid symbols, respectively. Solid triangles on the longitudinal hysteresis loop in (b) are the magnetic states, whose spin configurations are plotted in Fig. III.14 and III.15.

When these two anisotropies coexist, the magnetic hysteresis loop becomes asymmetric as shown in Fig. III.12 (a). The top-left corner of the longitudinal hysteresis is rounded, while the bottom-right one is sharp and square. At the same time, a much larger transverse component was found in the decreasing field branch. This behavior can be understood from the different effect of uniaxial and unidirectional anisotropies on the reversal process. For the decreasing field branch, both anisotropies prefer FM spins rotate clockwise since both anisotropy energies decrease in this direction. This results in an enhanced rotation and a large transverse component. However, when the field increases from negative saturation, these two anisotropies have opposite effects on the reversal. Uniaxial anisotropy favors FM moments rotating clockwise, while unidirectional anisotropy favors opposite rotation. When the magnitudes of these two anisotropies are comparable, they compete with each other, suppress the magnetization rotation and results in a much reduced transverse component during reversal (Fig. III.13 (c)). In real samples with inhomogeneous interfacial coupling or uniaxial anisotropy, the reversal behavior in the decreasing field branch will not change qualitatively since the two anisotropies cooperate with each other. However, for the increasing branch, this will cause spatial variation of the preferred direction of rotation.

To simulate this effect, the same interfacial inhomogeneity was assumed as used in Section III.B. $K_u = 12$ kJ/m^3 was used. The resultant transverse hysteresis loop displays the same asymmetry as the case without inhomogeneity (Fig. III.12 (b)). A slightly larger coercivity is due to the frustration from interfacial inhomogeneity. Fig. III.14 and III.15 show the spin configuration during reversal for decreasing and increasing field branches. The spatial variation of transverse magnetization is color coded. For the decreasing field branch, only very small color contrast was found, suggesting a reversal process through nearly coherent rotation. However, as the field increases from negative saturation, more complicated domain patterns were found. A striking difference with the other branch is the dark-gray bands of about 40 nm wide, which are domain walls separating reversed

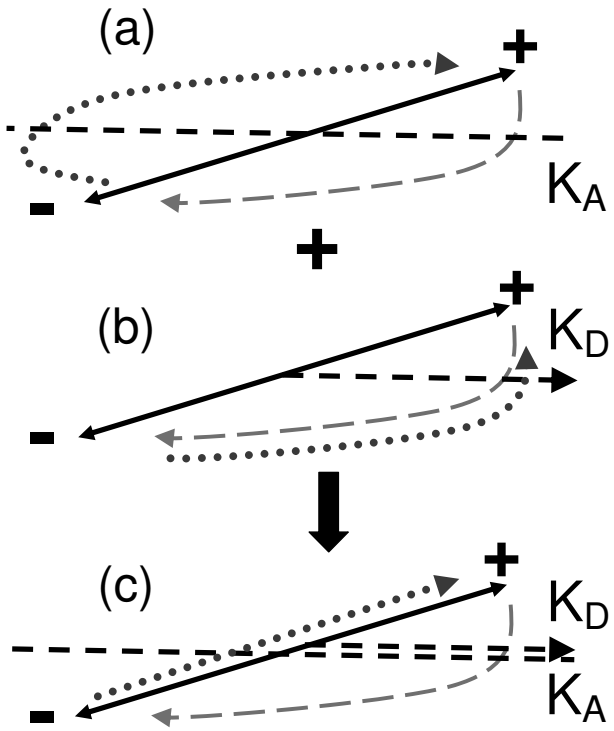

Figure III.13: Schematics of the reversal process when there is (a) only uniaxial anisotropy, (b) only unidirectional anisotropy, or (c) both anisotropies. Solid line refers to the magnetic field direction. Short dashed lines refer to the easy axis/direction of the uniaxial/unidirectional anisotropy. Long dashed line and dotted line refer to the magnetization reversal path of the decreasing and increasing field branches, respectively.

and un-reversed regions. As the field increases, these domain walls propagate until all FM spins are reversed. This demonstrates that the cooperation and competition of the two anisotropies result in reversal processes through coherent rotation and domain wall motion for the two field sweep branches, respectively.

It is worth noting this asymmetric reversal mechanism is independent of the mechanism found in Section III.B. Local incomplete domain walls parallel to the interface will form and dominate the reversal process when unidirectional anisotropy is large enough. Competing anisotropies dominates the asymmetric reversal when unidirectional anisotropy is small and comparable with uniaxial anisotropy. However, even for the hysteresis loop in Fig. III.12 (b) where the EB field is small, examining the magnetization depth profile shows that the FM does not rotate coherently in the depth of the FM, and an incomplete domain wall is developed (Fig. III.16). When the FM is half reversed in the decreasing branch, from the top of the FM to the interface, a difference of about 35% of the saturation magnetization was found. This is due to the interfacial nature of EB phenomenon, and suggests that parallel incomplete domain wall is a universal property of EB.

That parallel domain wall structure is an integral part of EB and can result in asymmetric magnetization reversal questions the applicability of simulation methods that model the FM as a single layer without structure in its depth. A typical and most important approach under this assumption is the Stoner-Wolfarth model. In the literature, this model has been successful in explaining many experimental features, including the role of misalignment in reversal asymmetry, high order anisotropy, and training effect [49, 10, 97]. Below, a comparison between micromagnetics considering the depth profile and Stoner-Wolfarth numerical calculation is made. To make a sensible comparison, no interfacial inhomogeneity is included in the micromagnetic simulation. In case of a FM with only uniaxial anisotropy, two simulation methods give nearly identical longitudinal and transverse components of the magnetization as a function of the field (Fig. III.18 (a)). Furthermore, when there is only a small unidirectional anisotropy $K_d = 3.86$ kJ/m^3, in the

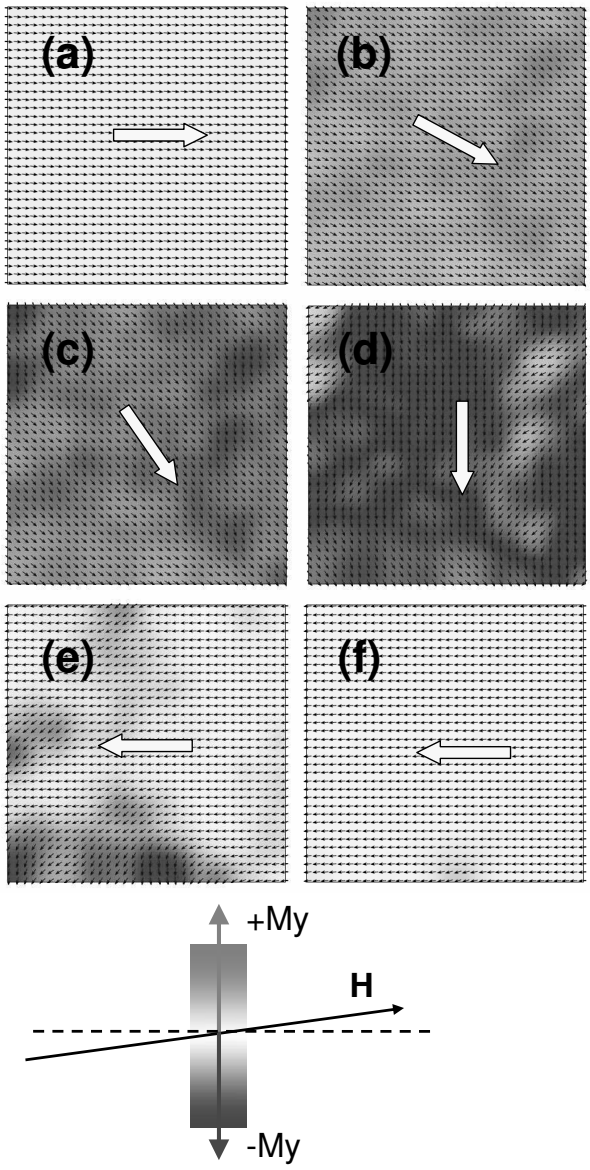

Figure III.14: Spin configurations of the FM when reversing from positive to negative saturation. For figure (a) to (f), the corresponding magnetic field decreases, as marked in Fig. III.12 (b). The bottom-most figure gives the color coding and the geometry, so that dark-gray, white and black refer to positive, zero, and negative transverse component M_y. Big light-gray arrows mark the dominating spin orientation.

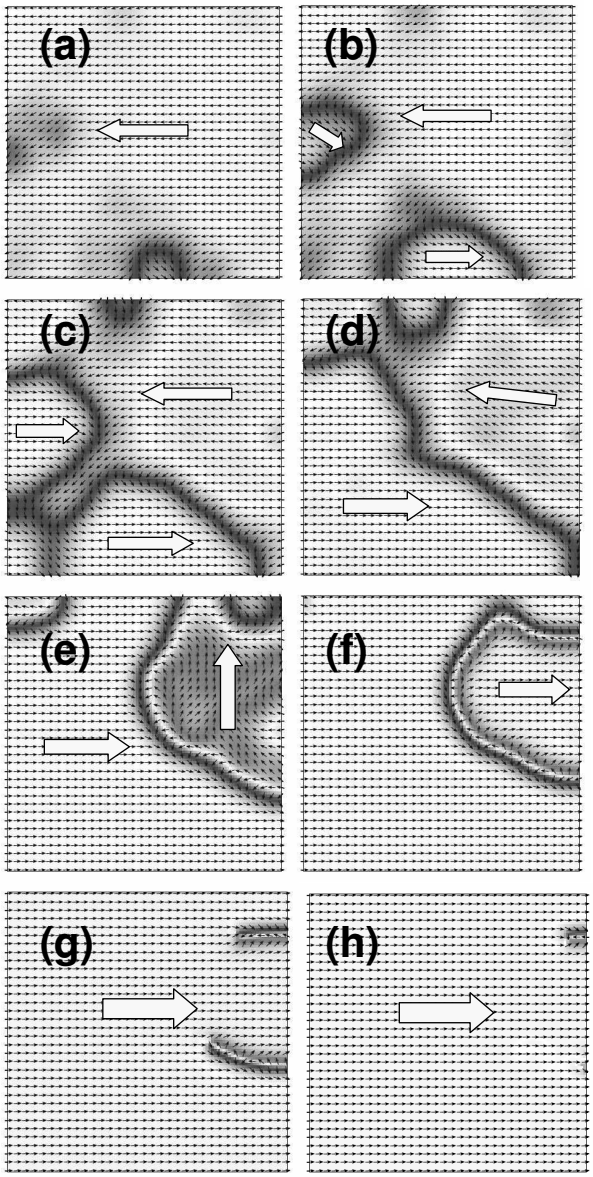

Figure III.15: Spin configurations of the FM when reversing from negative to positive saturation. For figure (a) to (h), the correspondent magnetic field increases, marked in Fig. III.12 (b). The same color coding is used as in the Fig. III.14. Big light-gray arrows marks the dominating spin orientation of corresponding domains.

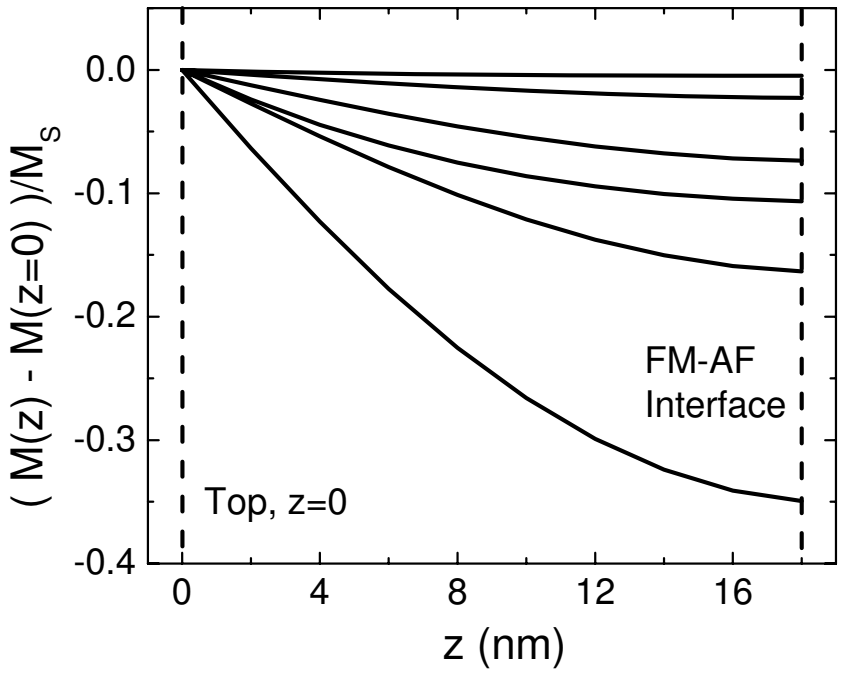

Figure III.16: Longitudinal magnetization depth profile in the magnetic field decreasing branch of the hysteresis loop in Fig. III.12 (b). Curves from top to bottom correspond to magnetic fields $H = -0.64$, -0.92, -0.84, -0.68, -0.76, and -0.72 kOe. The one with the largest depth dependence corresponds to the magnetic state half-way reversed.

Stoner-Wolfarth model or interfacial coupling with $J_{FM/AF} = 0.11dJ_{AF}$ (equivalent of StageZeeman field of 618 kA/m in OOMMF) in micromagnetic simulation, very similar result was also found (Fig. III.18 (b)). This justifies the validity of subsequent comparison.

Stoner-Wolfarth numerical calculation for K_u = 0, 5, 10, 15, 20, or 25 kJ/m^3, and K_d = 0, 10, 20, 30, 40, or 50 kJ/m^3 was performed (Fig. III.17). The result shows qualitatively similar behavior as discussed earlier in this section, where small K_d is considered. When there is only uniaxial or unidirectional anisotropy, the important features in the transverse magnetization in as found in Fig. III.11 were nicely reproduced. When two anisotropies coexist, a larger transverse component is developed in the decreasing field sweep than in the increasing sweep. This behavior persists for the whole range of anisotropy magnitude, for it only concerns the relative magnitudes of K_d and K_u. However, as the interfacial coupling grows larger, parallel domain walls will become more pronounced, and the opposite asymmetry similar to Fig. III.3 will develop.

Fig. III.19 compares hysteresis loops for a large interfacial coupling $J_{FM/AF} = 1.13J_{AF}$ in micromagnetic simulation, and equivalently K_d = 38.6 kJ/m^3 in Stoner-Wolfarth calculation, with or without K_u = 15 kJ/m^3. For both cases, the two calculations show drastically different magnetic behavior. While Stoner-Wolfarth calculation still exhibits the same asymmetry as the case with small unidirectional anisotropy, micromagnetic simulation clearly shows a tail that extends to magnetic fields much larger than the coercive fields around negative saturation. When uniaxial anisotropy is included, a smaller transverse component was found in the decreasing field branch in the micromagnetic simulation. This suggests that the magnetization depth profile has become so significant that the reversal process can not be properly described by calculations assuming FM moments as uniform throughout the depth. As for the criterion when the FM depth profile becomes important, this should depend on the FM thickness t_{FM}, exchange constant A, uniaxial anisotropy K_u, and exchange coupling $J_{FM/AF}$. Qualitatively, a large

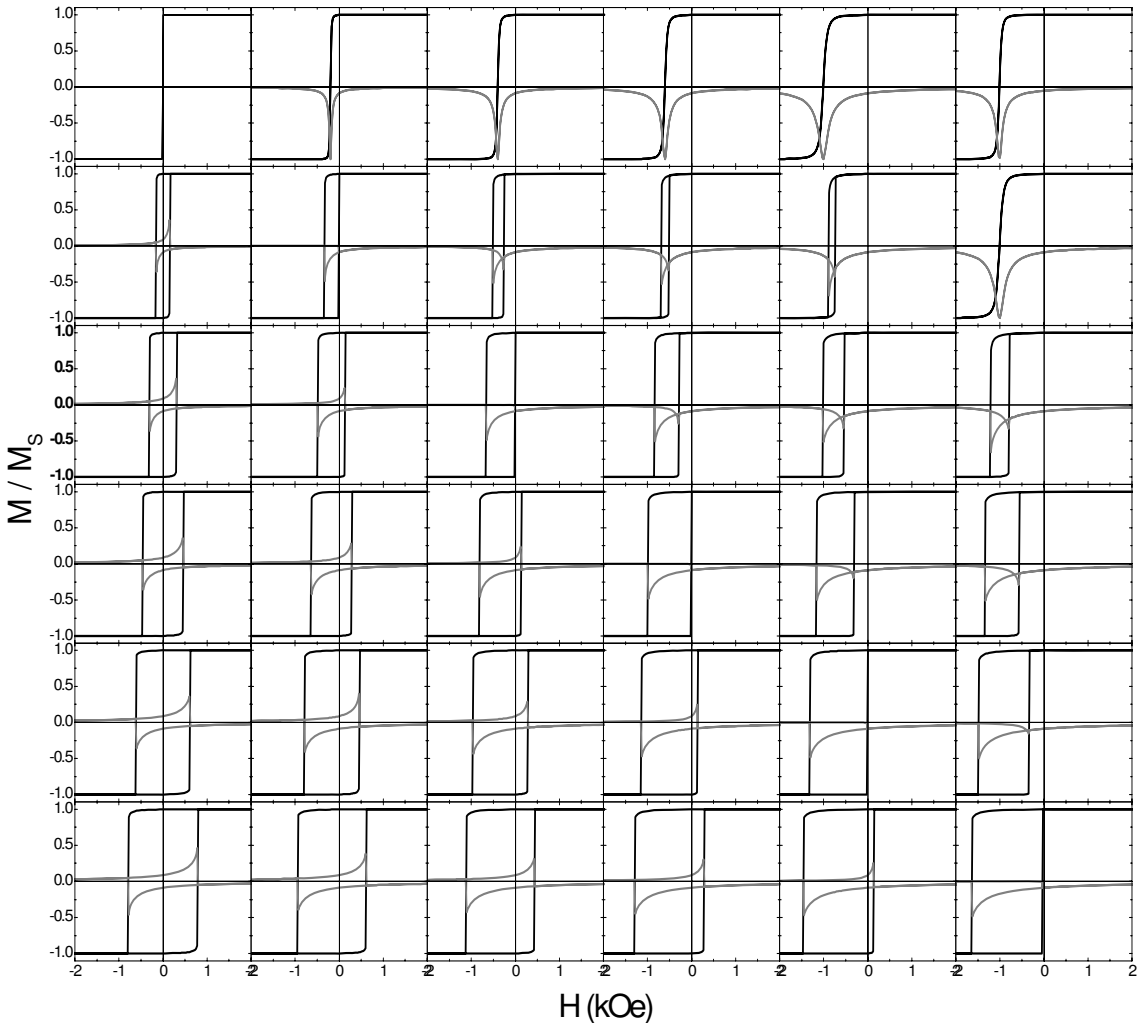

Figure III.17: Magnetic hysteresis loops calculated using Stoner-Wolfarth model. Both longitudinal (black) and transverse (light-gray) magnetizations are calculated. From left to right, the unidirectional anisotropies are 0, 10, 20, 30, 40 and 50 kJ/m^3, respectively. From top to bottom, the uniaxial anisotropies are 0, 5, 10, 15, 20, and 25 kJ/m^3, respectively.

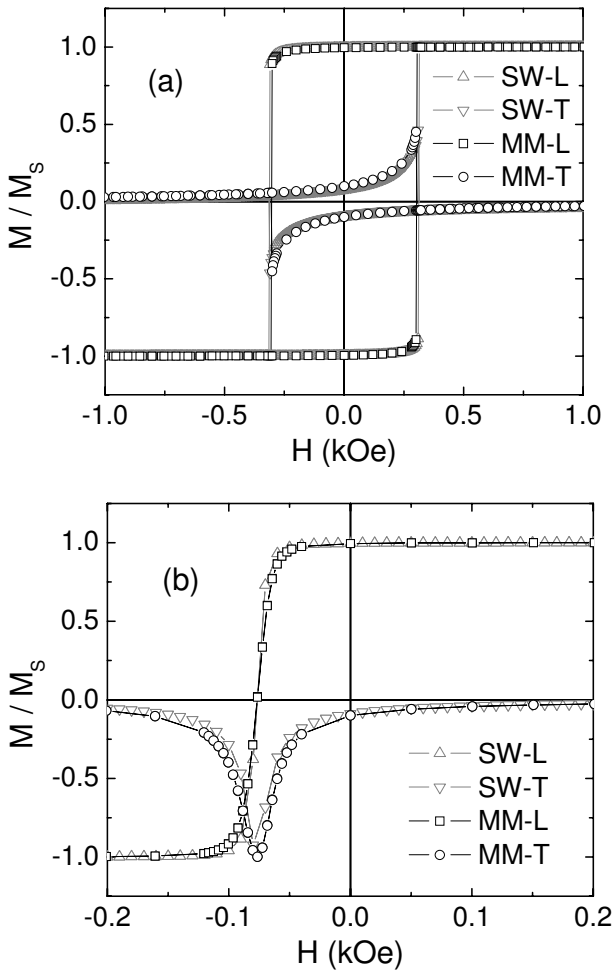

Figure III.18: Comparison of Stoner-Wolfarth numerical calculation (SW) and micromagnetic simulation (MM) for both longitudinal (L) and transverse (T) magnetization vs. magnetic field. (a) Only uniaxial anisotropy is considered, $K_u = 10$ kJ/m^3. (b) Only unidirectional anisotropy is included, $J_{FM/AF} = 0.11 J_{AF}$, or $K_d = 3.86$ kJ/m^3.

$J_{FM/AF}$, K_u, and t_{FM}, or a small A can cause a more pronounced FM domain wall, and thus simple Stoner-Wolfarth model is more likely to fail.

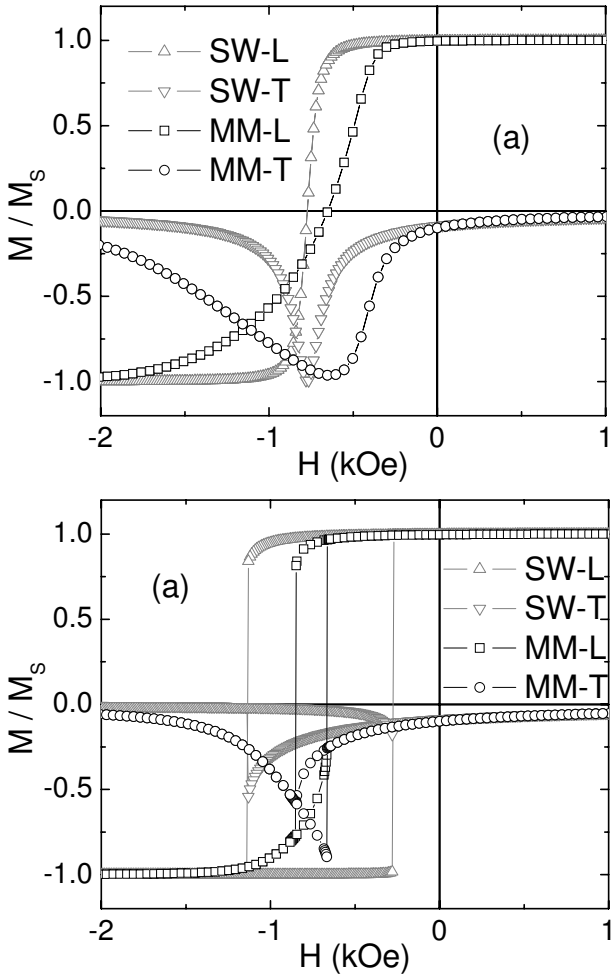

Figure III.19: Comparison of Stoner-Wolfarth numerical calculation (SW) and micromagnetic simulation (MM) for both longitudinal (L) and transverse (T) magnetization vs. magnetic field. (a) $J_{FM/AF} = 1.13 J_{AF}$ in Micromagnetic simulation, or equivalently $K_d = 38.6$ kJ/m^3 in Stoner-Wolfarth calculation. (b) $K_u = 15$ kJ/m^3, and $J_{FM/AF} = 1.13 J_{AF}$, or $K_d = 38.6$ kJ/m^3.

III.E Length Scale Relevance in Asymmetric Reversal

As demonstrated in the previous section, the two asymmetric magnetization reversal mechanisms exhibit different relative magnitudes of transverse magnetization peaks during reversal. When competing anisotropies dominate the

reversal behavior, a larger M_T is found in the decreasing field branch. However, parallel FM domain walls causes a larger M_T in the increasing field branch because the domain walls are less suppressed in this branch by a smaller coercive field than in the other. In the literature, measurement of transverse magnetization and examining their peak heights at reversal by vector MOKE, magnetometry, etc., were widely used to study the reversal asymmetry [44, 105, 97]. While the two asymmetric reversal mechanisms can explain many experimental features in simple model systems, more subtle and complicated situations were also found in the literature. A confusing observation found in some twinned FeF_2/Fe bilayers is that the asymmetry of transverse magnetization peaks is sensitively dependent on the alignment of the sample relative to the magnetic field [97]. With about 5° inplane rotation of the sample, the reversal asymmetry is reversed. It is worth mentioning that this was never observed in untwinned FeF_2/FM samples. Among numerous twinned FeF_2 or MnF_2 based samples studied by vector magnetometry, neutron scattering, magneto-transport, etc, most samples do not exhibit this alignment-sensitive asymmetry.

In Ref. [97], Tillmanns *et al.* attributed this to the presence of four-fold anisotropy. This interpretation requires a strong enough four-fold anisotropy to compete with anisotropies of lower orders. Misalignment between the easy axis of four-fold and other anisotropies is also necessary. However, as shown in Ref. [97], such strong four-fold anisotropy will cause a kink in one of the branches, suggesting that FM moments rotate to an intermediate state favored by the four-fold anisotropy. But this was never observed experimentally in FeF_2 systems due to the dominating uniaxial anisotropy (two-fold). In systems that do show kinked hysteresis, this alignment-sensitive asymmetry was not observed in samples measured so far [46]. This motivates us to look for alternative interpretation of this behavior, and we attribute this to the dispersion of easy directions from different AF domains and the relevance between FM domain wall width and AF domain size. Here, we consider a system with only uniaxial anisotropy and interfacial coupling.

Without inhomogeneity, for misalignment smaller than $arctan(2K_u/K_d)$, varying the field direction changes the transverse peak height, but not the asymmetry [49].

In Chapter II, we demonstrated that how interfacial exchange interaction couples different length scales in two materials. Depending on the comparison of the FM domain wall width and AF domain size, either FM moments average over multiple AF domains, or FM moments on different AF domains behave independently. In either case, a FM spin is influenced by AF spins in its vicinity of a length scale comparable with the FM domain wall width. Suppose there is a dispersion of AF spin axis between AF domains but not within each of them. When the FM domain wall width is much larger than AF domain size, large number of AF domains are averaged over and the statistical fluctuation of the easy direction averaged by different FM moments is small. In this case, the misalignment between magnetic field and easy directions has little spatial variation, thus the asymmetry is insensitive to the alignment. When the AF domain size is comparable or just slightly smaller than the FM domain wall width, large spatial fluctuation of averaged easy directions is expected. Therefore, FM spins will rotate in different directions depending on the local misalignment between the easy direction and magnetic field, leading to a subtle and less intuitive situation. This idea is confirmed by micromagnetic simulation, assuming AF grain size of 25 nm, within each of which uncompensated AF moments point in the same direction randomly chosen between $\pm 5°$. The interfacial coupling is $1.81 J_{AF}$, and uniaxial anisotropy is $K_u = 25$ kJ/m^3. Here, the FM domain wall width is about 40 nm, thus a FM spin is only influenced by about three AF domains. Strong dependence of reversal asymmetry on misalignment was found.

Resultant hysteresis loops for misalignments between $\pm 4.29°$ are shown in Fig. III.20. For a large misalignment, *e.g.* $4.29°$, a hysteresis loop similar to Fig. III.3 was found, with a larger transverse component in the increasing field branch, suggesting a reversal process dominated by parallel FM domain walls. As the misalignment decreases, the transverse peak in the increasing field branch

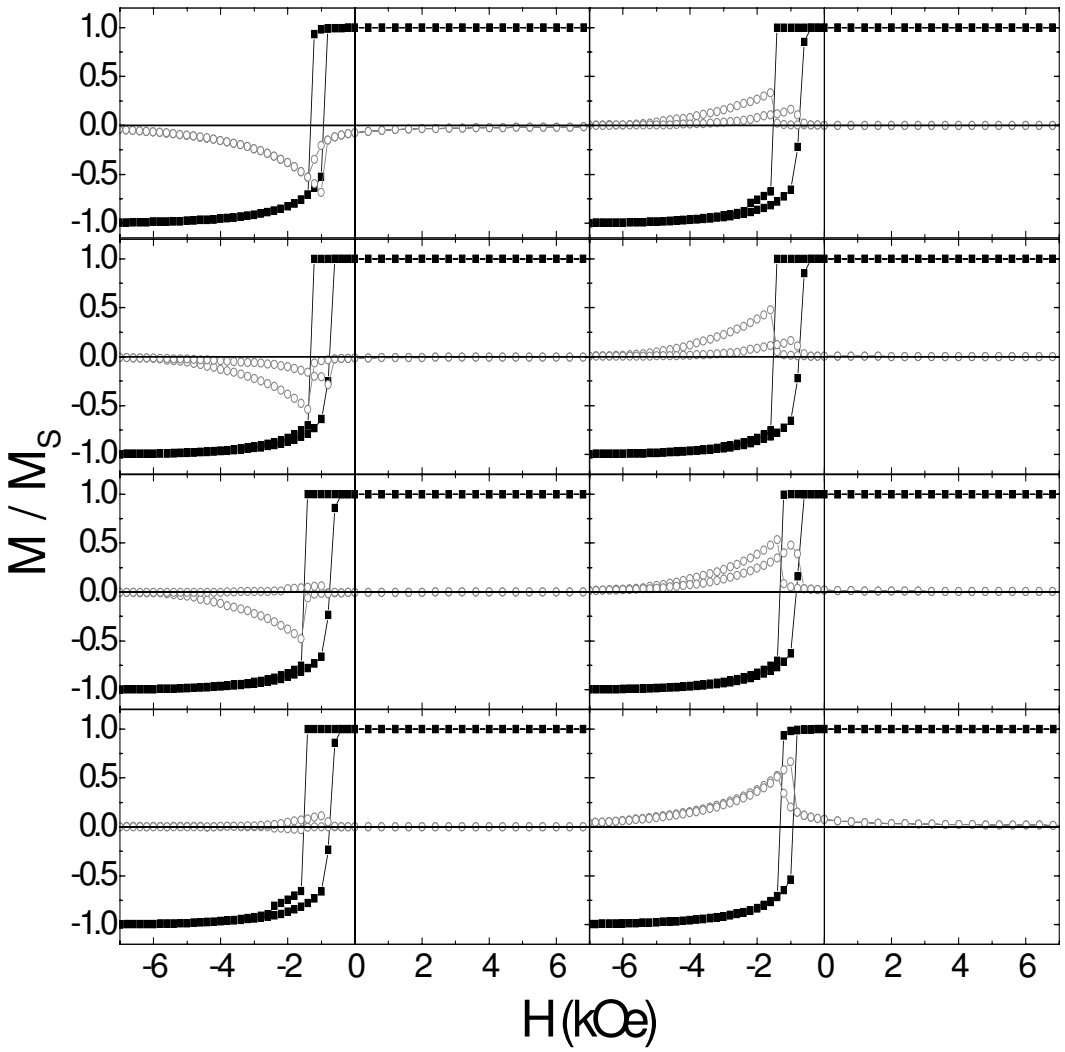

Figure III.20: Magnetic hysteresis loops for different misalignment between the average easy direction and magnetic field. Both longitudinal (solid squares) and transverse (empty circles) magnetizations are shown. From top to bottom in the left column, the misalignments are 4.29, 0.86, 0.29, and 0 degree, respectively. Misalignments for figures in the right column are -0.14, -0.29, -1.17, -4.29 degree, respectively.

becomes larger than that in the other branch. When the misalignment angle crosses zero, the transverse component reduces to nearly zero, as expected from the symmetry consideration. When the misalignment further decreases to negative, the transverse peak in the decreasing field branch is at first larger and then smaller than that in the increasing field branch. When misalignment reaches -4.29°, the same asymmetry as that for +4.29° misalignment is restored.

If one changes the AF domain size to much larger or smaller than the FM domain wall width, this alignment-sensitive asymmetry disappears. In Section III.B, we showed that the inhomogeneity of the magnitude of interfacial coupling is important to explain experimental observations. Earlier in this section, we also showed that inhomogeneity is important in causing coherent rotation and domain wall motion in two hysteresis branches. Here, it is the angular dispersion of AF spin axis that is important. Also, this result again demonstrates the significance of lateral length scale relevance in modifying the magnetization reversal process. Observation of this alignment-sensitive behavior requires the sample having the right length scale of interfacial inhomogeneity to allow for a large enough spatial variation of the average AF spin axis. It was mentioned earlier that the AF grain size in twinned FeF_2 is about 5-10 nm, much smaller than most FM domain widths, and the AF domain size in untwinned FeF_2 is much larger than the FM domain wall width. Therefore, this behavior was generally not observed in all untwinned and most twinned FeF_2/FM systems.

III.F Training Effect Induced Reversal Asymmetry

It was found in some exchange bias samples like CoO/Co that show training effect, the magnetization reversal asymmetry also evolves as the field is cycled [106]. Recently, it was called to attention that training effect only occurs in systems with biaxial anisotropy [10]. For fluoride-based systems, like FeF_2 and MnF_2 we studied, where only uniaxial anisotropy is present, training effect was never ob-

served. While two-fold anisotropy favors the AF spins on the easy axis antiparallel with each other, with four-fold anisotropy, perpendicular orientations of AF spins are also favored. When the four-fold anisotropy competes with AF exchange energy and interfacial coupling, the system may exhibit a ground state and multiple metastable state. It was argued that the AF spins, which was in its ground state after field cooling, will fall into a metastable state as the magnetic field is cycled. As shown in the literature, biaxial anisotropy can also create a complicated energy landscape on the parameter space, giving rise to unexpected reversal behavior [105, 106]. In this section, I will examine the training of reversal asymmetry as a result of the magnetic field cycling.

Simple Stoner-Wolfarth calculation will be used for this study. The system energies of the AF and FM E_{AF} and E_{FM} are,

$$E_{AF} = E_{K4} + E_{AF} + E_{inf} + E_{HAF}$$
$$E_{FM} = E_{K2} + E_{inf} + E_{HFM}.$$

Here, E_{K4}, E_{AF} and E_{HAF} are the four-fold anisotropy, exchange energy, and Zeeman energy of the AF, while E_{K2} and E_{HFM} are the uniaxial anisotropy and Zeeman energy of the FM, respectively. E_{inf} is the interfacial coupling energy, which is assumed to be equal to the AF exchange energy. I assume that the easy axis of all anisotropy is tilted by $+5^\circ$ away from the magnetic field direction. The system energy is parameterized into three variables, θ_1 and θ_2, the orientations of AF spins in the two sublattices, and θ_{FM}, the orientation of the FM macrospin. To evaluate the magnetization reversal process, I assume that the AF reaches its global energy minimum after cooling. To evaluate the training process, the ground state of the AF spins were first searched by brutal force. And then, energy local minimum was searched by following the energy gradient from the initial state. Below, two different cases are discussed, for large or small AF anisotropy. The FM uniaxial anisotropy $K_u = 10$ kJ/m^3 and saturation magnetization $M_S = 494$ kA/m are used for calculation. Ferromagnetic interfacial coupling with maximum coupling

energy 2.5 kJ/m^2 is assumed.

In the first case, we consider $E_{K4|max}/E_{AF|max} = 5$. The AF ground state has the AF spins orienting at $\theta_1 = 10°$ and $\theta 2 = -95°$. This is the result of the competition between the interfacial coupling that favors spins from both sublattices parallel with the FM moment, AF exchange interaction between the sublattices that favors antiparallel alignment, and biaxial anisotropy that favors the spins on any of the four easy orientations. Using the AF ground state as the initial condition, we calculated the hysteresis for the first three magnetic field cycles. Fig. III.21 shows the result. We found for a large AF anisotropy, the AF spins are only perturbed around their initial orientations without training effect. The magnetization reversal symmetry is opposite to what we found earlier for small interfacial coupling. The discrepancy lies in the two perpendicular AF moments at around 10° and −95°. The easy axis of uniaxial anisotropy lies in +5° and -175°. Following similar analysis as in section III.D, unidirectional and unaxial anisotropy compete with each other in the decreasing branch, while they both favor the FM rotate to counter-clockwise in the increasing field branch.

In the second case, we consider $E_{K4|max}/E_{AF|max} = 3$, where the ground state has the AF spins orienting at $\theta_1 = 16°$ and $\theta 2 = -95°$. Using these angles as the initial condition, the magnetic hysteresis for the first three field cycles were calculated and plotted in Fig. III.22. Training effect was found for this case. After the first cycle, $\theta_1 = 4.7°$, and $\theta_2 = -174.5°$, antiparallel with each other. This change of the AF spin configuration leads to zero exchange bias, and magnetization reversal becomes symmetry. For a real magnetic magnetic system, the two spin axis may not be coupled with the FM equivalently, and a finite residual exchange bias may exist. But even so, the reversal asymmetry is still expected to become less significant as in the first loop. This is similar to what was found in the anisotropic magneto-resistance (AMR) measurement on CoO/Co [106]. After the first cycle, AF spins are trapped in the metastable local energy minimum that exhibits reduced exchange bias and reversal asymmetry. More field cycling do not change the AF

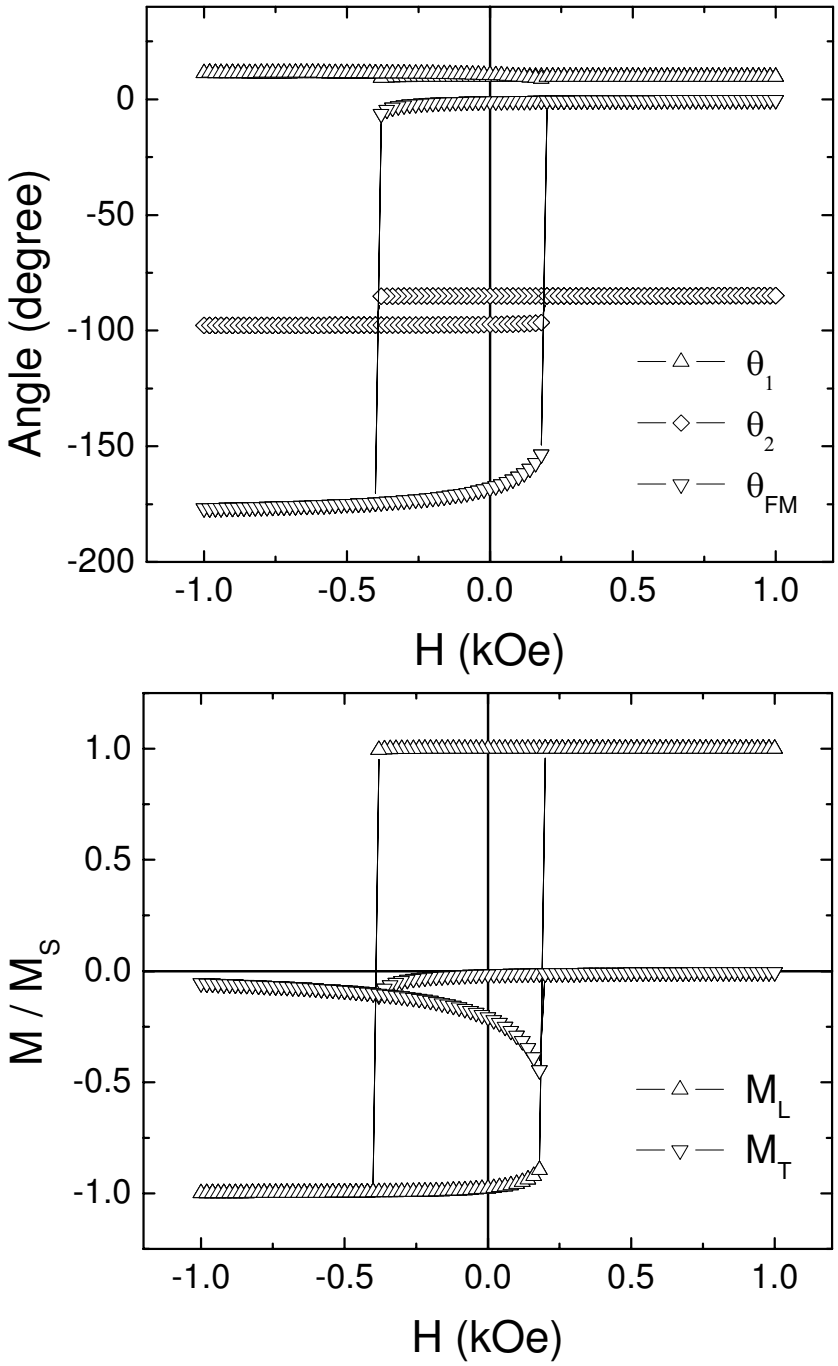

Figure III.21: Stoner-Wolfarth calculation result for $E_{K4|max}/E_{AF|max} = 5$, where no training effect was observed. (a) Orientation of the AF spins in the two sublattices θ_1 and θ_2, and that of the FM spin θ_{FM} as a function of magnetic field. (b) FM longitudinal M_L and transverse magnetization M_T as a function of magnetic field.

spin configuration and FM hystersis. Further studies are necessary to examine the parameter space in much greater detail, and unravel the relationship between the reversal asymmetry and training effect.

III.G Asymmetric Reversal in Nanostructured systems

In antiferromagnetic (AF)- ferromagnetic(FM) bilayers the interfacial coupling is believed to control the magnitude of the loop shift and domains in the AF and/or the FM play a crucial role [107]. Thus drastic changes of magnetic properties are expected when the lateral size of an EB structure becomes comparable to these sizes. A less explored possibility is that in an EB sample nanostructuring produces major changes in the demagnetizing energy which may affect the magnetic properties in a fundamental way. The reversal mechanism in magnetic materials originates from a balance between different energies: Zeeman, demagnetizing, anisotropy in the FM and AF, and interfacial exchange. In contrast to a pure FM layer, those energies are not symmetric in the two branches of the hysteresis loop, but asymmetric because of the unidirectional anisotropy induced by EB. This can produce not only shifted but also asymmetrically shaped hysteresis loops. Patterning a FM layer changes the demagnetizing energy drastically which often leads to smaller FM domains and increases in coercivity. This may affect the reversal mechanism in FM-AF bilayers, perhaps influencing differently the two reversal branches and changing the magnitude of the EB. The possibility of such effects has not been emphasized in recent experiments on patterned EB bilayers [41, 75, 108, 109, 110, 74]. There, the interpretation of size dependent exchange bias field H_{EB} is often focused on modifications of the exchange interaction at the AF-FM interface and/or matching of length scales. To investigate this possibility we have embarked on a systematic study of nanostructuring exchange biased Fe-FeF_2 bilayers.

Fe-FeF_2 bilayers are prepared by e-beam evaporation on MgO(100) sub-

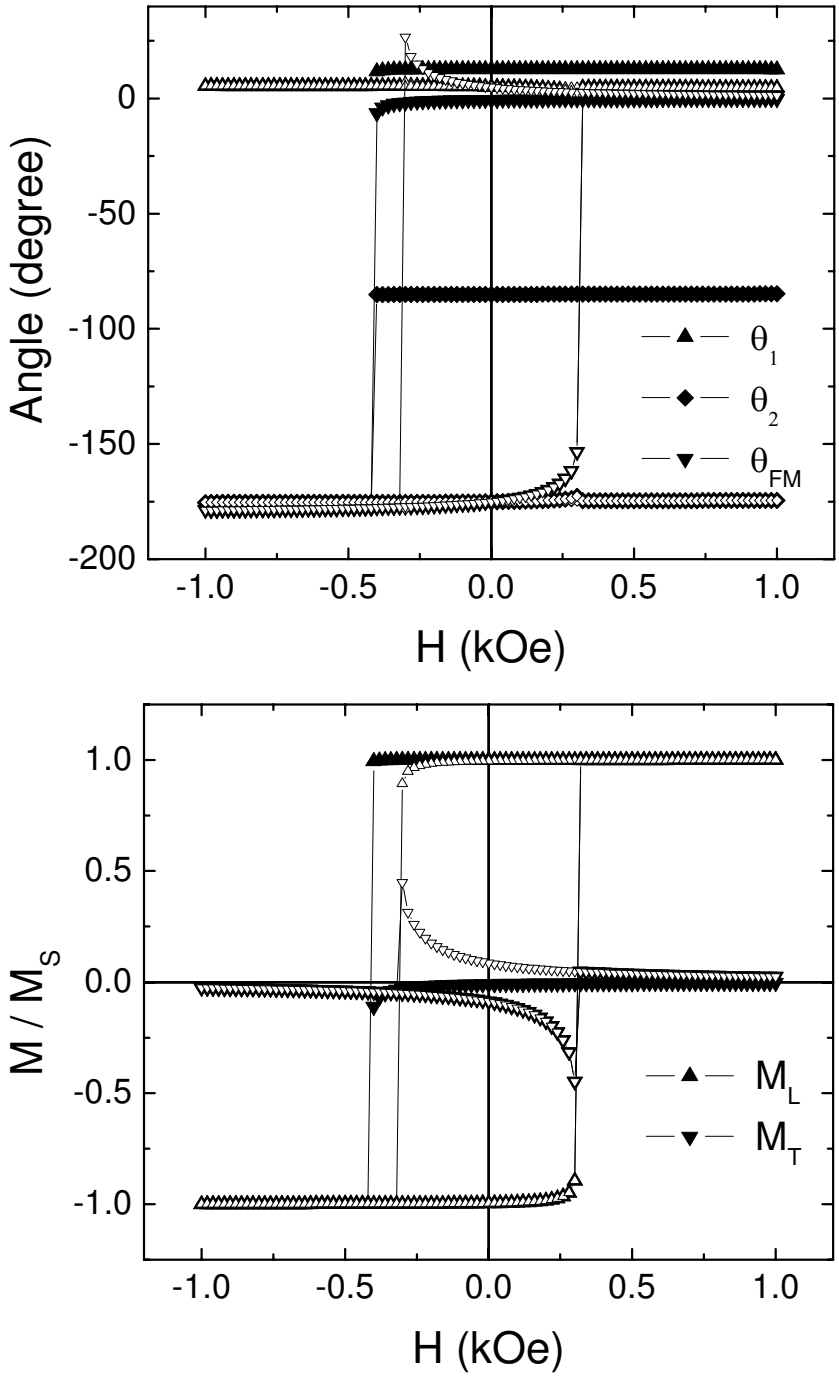

Figure III.22: Stoner-Wolfarth calculation result for $E_{K4|max}/E_{AF|max} = 5$, where training effect was observed. (a) Orientation of the AF spins in the two sublattices θ_1 and θ_2, and that of the FM spin θ_{FM} as a function of magnetic field. (b) FM longitudinal M_L and transverse magnetization M_T as a function of magnetic field. The first and second field cycles are plotted in empty and filled symbols, respectively.

strates. From X-ray diffraction, we determine that the layer structure is FeF_2 (23.8 nm) / Fe (12 nm) / Al (4.8 nm). Different square arrays of circular Fe dots with diameter of 600 ± 10 nm and 100 ± 10 nm were prepared by Ar^+-ion milling through a resist mask produced by e-beam lithography. The center-to-center distance of the dots is twice their diameter. On the same sample, an unpatterned area was kept, covered with resist during ion-milling to provide a continuous film control sample. To minimize possible differences due to processing, the patterned and unpatterned area were subject to the same processing steps together. Because of the small overall area of electron beam patterned samples, the magnetic properties were measured by magneto-optical Kerr effect (MOKE) using an optical magnet cryostat. The MOKE signal was measured after ramping the field with 1 Oe/s to a specific value, waiting for 5 sec and than taking the average of 5 consecutive values measured within 10 sec. The HeNe laser beam was focused down to 50μm diameter to measure the unpatterned or patterned area (size: 80 $\times$ 80 μm^2) on the same film individually. The samples were field cooled from 150 K to 10 K through the Néel temperature T_N =78.4 K of FeF_2. The cooling field $H_{FC} = 2$ kOe, oriented parallel to the film surface along the [010] direction of the MgO substrate, is large enough to saturate the FM layer and the FM dots. Using p-polarized light (incident at 58° with respect to the normal), the longitudinal magnetization component M_l (parallel to the field) was measured by detecting the Kerr rotation of the reflected light. The transverse magnetization component M_t was measured by rotating the polarization of the incident beam by 45° with respect to the commonly used p-polarization [111, 105].

Fig. III.23 shows the MOKE signal of M_l and M_t at 10 K of an unpatterned region on the Fe-FeF_2 bilayer. Typically for many EB bilayer systems [112, 113, 89, 5, 114, 115, 116, 117, 118], the hysteresis loop of M_l (open symbols) is asymmetric, i.e. one branch (in Fig. III.23 the increasing branch) is more rounded than the other.

This asymmetry is also reflected in the corresponding M_t which shows a

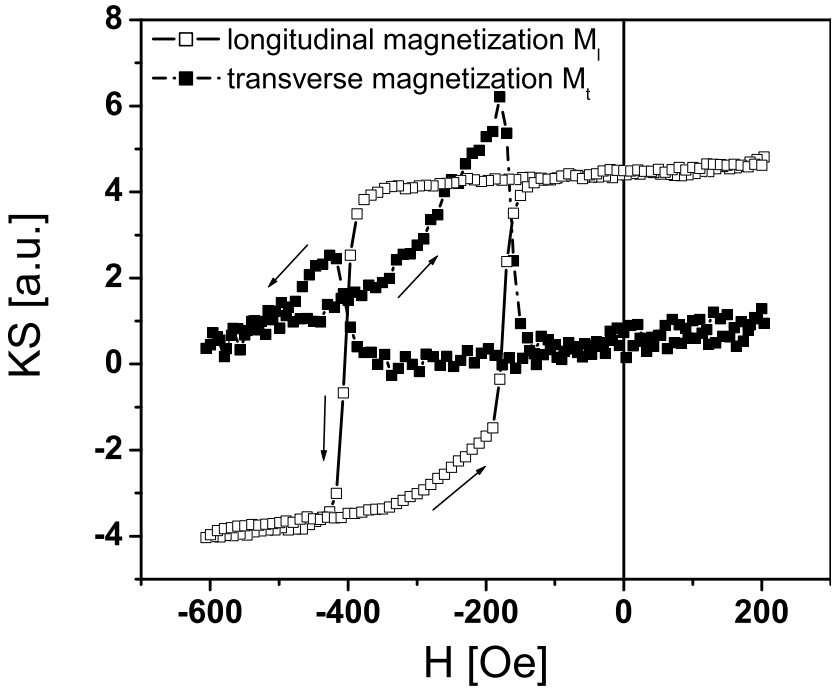

Figure III.23: MOKE signal of M_l (open symbols) and M_t (closed symbols) of the unpatterned area of the film at 10 K after field cooling in 2kOe.

larger signal in the increasing branch than the decreasing branch. This behavior is very similar to what was found in Fig. III.3, suggesting the presence of local incomplete FM domain walls parallel to the interface. This similarity implies that a likely situation is a larger winding of domain walls in the depth in the increasing branch, and at the same time, more domains laterally as shown in Fig. III.2. This suggests different spin structures in the two branches of unpatterned film.

The same sample patterned to dot arrays has hysteresis loops with clearly larger coercive field H_c and smaller EB field H_{EB} (Fig. III.24), even if the larger errors of the exact branch positions are considered. The measured hysteresis is not as smooth as that from the unpatterned area, probably because of a large linear background subtracted from the data. As expected, with increasing temperature, H_{EB} for both the unpatterned and patterned areas becomes smaller and vanishes at T_N (inset of Fig. III.24).

To investigate the influence of patterning on the reversal in detail, we

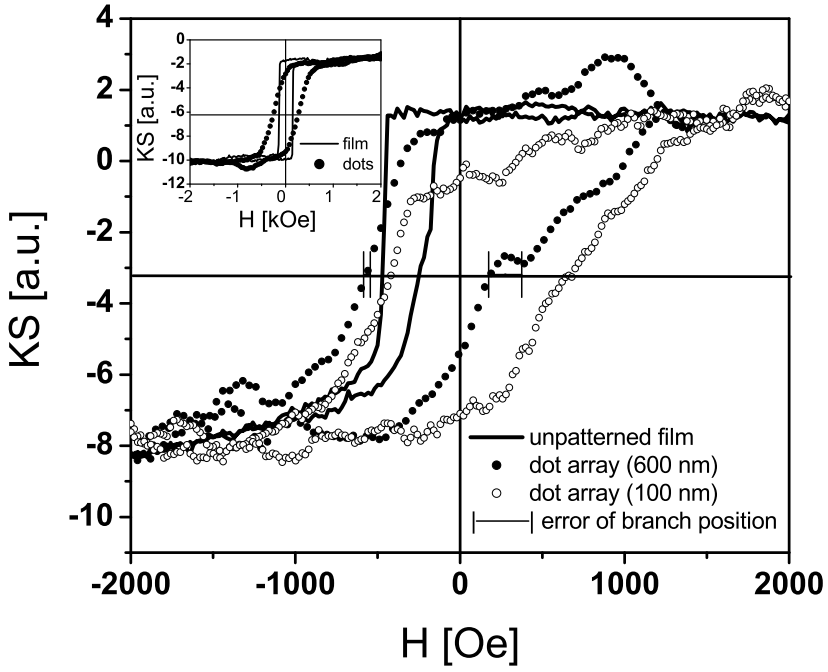

Figure III.24: MOKE signal (KS) of M_l vs. H of unpatterned Fe-FeF_2 film (line) and different Fe dot arrays (circles) on FeF_2 at 10 K (below T_N). The inset shows the signal of unpatterned Fe-FeF_2 film and the 600 nm Fe dots on FeF_2 at 90 K (above T_N).

compared the positions of the decreasing and increasing branches of unpatterned and patterned film area with 600 nm dots at different temperatures and with the external field applied either parallel or at 40 ° ("tilted") with respect to the sample surface (Fig. III.25). The error bar of the coercive field reflects the scatter in the data (cf. Fig. III.24).

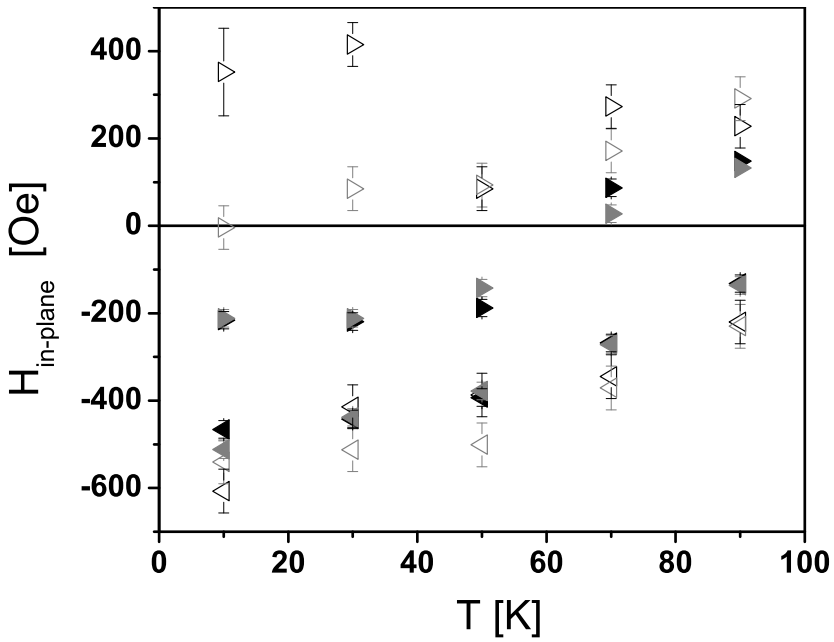

Figure III.25: In-plane magnetic field component $H_{\mathrm{in-plane}}$ for the positions of the decreasing branch (triangles pointing to the left) and increasing branch (triangles pointing to the right), defined by $H(M_l = 0)$, for unpatterned (solid symbols) and patterned (open symbols) sample. For the black symbols the field was parallel to the sample surface. For the grey symbols the field was tilted by 40 ° with respect to surface after field cooling.

At low temperature ($\leq$ 30 K) a strong shift of the increasing branch of the hysteresis loop is caused by the patterning, while the change on the decreasing branch is much less pronounced. To compare the in-plane component of the magnetization of the two series of experiments, the measured value for the tilted sample was multiplied by cos(40 °) as shown in Fig. III.25.

Since domains may play a central role, the following considerations are important. If the AF domain sizes are much smaller than the FM dot size, any

explanation [74] that assumes comparable AF domain size with FM dot size should not play a major role here. The AF domain size in such FeF_2/Fe thin films is difficult to measure because of their very small size. An indication of the domain size can be inferred from the thickness dependence of the EB. FeF_2-Fe bilayers prepared under similar conditions show an increase of H_{EB} with increasing AF film thickness up to about 20 nm and then a levelling off [119]. The constant H_{EB} at larger thicknesses is an indication that the EB and the size of AF domains are mostly determined by the size of twins in the AF, whose size is comparable to the AF film thickness (24 nm) [36, 120]. Alternatively, the lateral size of the AF domain can be estimated to be about twice the AF film thickness [19]. The width L of AF domain wall can be estimated to be $L = \pi(A_2/K)^{1/2} = 0.6$ nm (Table A.3). For 100 nm dot size, reduced H_{EB} might be explained by the comparable AF domain size with the structural size [74]. The situation is different for the larger dots with diameter of 600 nm. There, both the AF domain size and the wall width are considerably smaller than the dot size. In the following, we will concentrate on possible origins of the reduced H_{EB} for these comparably large dots, which is unexpected considering interpretations discussed so far for patterned EB samples.

Since a training effect is not observed in the FeF_2-Fe system, it is generally assumed that for FeF_2 the AF spin distribution at the AF-FM interface is determined mostly by field cooling, which freezes to a stable configuration below T_N. In contrast, FM domains are not frozen, but change their average size from a large size at saturation to a smaller size at magnetization reversal. The latter requires the FM structure to be large enough to sustain multi-domain states. We can assume this for our polycrystalline Fe dots (diameter = 600 nm), because even for epitaxial Fe dots with smaller diameters and same thickness, multi domain states were observed [121]. Since H_c in our sample is mainly caused by pinning of FM domain walls at defects [2], it increases with larger domain wall density. Losses in the AF layer contribute to H_c only close to T_N, leading to a maximum in the otherwise constant H_c in Fig. III.25 of the unpatterned film.

The domain wall density depends on the domain size. Since the dots are large enough to sustain multi-domain states, shape anisotropy can be reduced by forming smaller domains in the FM. In the meantime, H_c increases by $\Delta H_c = 1/2(\Delta H_{CD} + \Delta H_{CI})$. Here, ΔH_{CD} and ΔH_{CI} are the shifts of the decreasing and increasing branches, respectively, towards larger coercivity. Since the domain structures at the two magnetization reversals are different in the unpatterned film, patterning might change the domain structure in the two branches differently. As a consequence, the shifts of the branches will be different, i.e. $\Delta H_{CD} \neq \Delta H_{CI}$. This changes H_{EB} by $\Delta H_{EB} = 1/2(\Delta H_{CD} - \Delta H_{CI})$ without need of a modified interfacial exchange interaction.

To investigate this issue, we will examine the data of Fig. III.25 in more detail. The first set of measurements was performed with the external field parallel to the sample surface and the second at 40° with respect to the sample surface. However, in both cases the sample was field cooled in a field parallel to the sample surface. Since the domain structure of FeF_2 freezes during field cooling into a stable configuration, the AF domain structure and the interfacial exchange interaction should be comparable for the untilted and tilted case. This is supported by the fact that the positions of the branches of the *untilted*, unpatterned film agree with rescaled positions of the *tilted*, unpatterned film over the whole temperature range (Fig. III.25). The situation is significantly different for the patterned sample at $T = 10$ K and 30 K, where patterning changes the in-plane component of H_{EB} differently for the tilted and untilted case. The interfacial exchange interaction of the dot array should not be altered by tilting either, because of the much larger size of the Fe dots compared to the AF domain size, and therefore properties of the interfacial exchange interaction comparable to the one of the unpatterned sample. For unchanged interfacial exchange interaction the different in-plane component of H_{EB} can only be due to the FM spin structure, which is not frozen and may be influenced by tilting. Obviously H_c, mainly determined by pinning of FM domains, changes in such a way that $\Delta H_{CD} - \Delta H_{CI} = 2\Delta H_{EB}$ is different for the untilted

and tilted sample. Because of the small AF domain size, a change of interfacial exchange interaction by patterning is not expected in our size regime. Moreover, it is unlikely that the changes of H_C and H_{EB} after patterning for $T \leq 30$ K stem mainly from averaging over different properties of the individual dots, because then we would expect similar large differences at all temperatures, in particular also above T_N. Therefore, such asymmetric shifts of the branches caused by changed FM domain structure should be the main contribution to the decreased H_{EB} in our patterned sample.

We notice that especially at $T \leq 30$ K the differences between patterned and unpatterned film in H_c and H_{EB} are caused by a strong shift of the increasing branch of the hysteresis loop, while the change on the decreasing branch is much less pronounced. This may be related to the different field values at the two reversals. The relative contribution of the Zeeman energy to the total energy of the FM layer increases with the external field H_{ext} and will be different in the two branches. Therefore minimization of the Zeeman energy determines the spin structure at the reversal of the decreasing branch more strongly than the one of the increasing branch. Since the Zeeman energy favors parallel spin orientation, the smaller M_t in the decreasing branch (compared to the increasing branch) is an indication that this situation is present in the unpatterned area of our sample. The demagnetization field H_d due to patterning changes the total energy in the FM layer, which is equivalent to a change of the Zeeman energy with an external field reduced by $1/2H_d$. This will effect the spin configuration only slightly, if Zeeman and demagnetization energies together still dominate the total energy of the system. In order to estimate the relevance of this effect we calculate an approximate upper limit for the demagnetization field H_d. First, we consider only a single dot without interdot coupling with its neighbors. This approach seems reasonable according to measurements on polycrystalline iron dot arrays on Si with comparable geometries [122] which implies interdot coupling can be neglected. The upper limit of the demagnetization field can be estimated to $H_d = -N\,M_s =$

-245 ± 14 Oe with an approximated demagnetization factor $N = 0.01571 \pm 0.0002$ for a single iron dot and a saturation magnetization $M_s = 1.24 \times 10^6$A/m, as obtained by SQUID magnetometry. The maximum field which can be produced by the next nearest neighbors is 19 Oe and much smaller than H_d, which supports neglecting interdot interaction. The relatively weak shift of the decreasing branch of the patterned area implies that the FM spin structure is dominated by the sum of Zeeman and demagnetization energy, since $1/2H_d = -122$ Oe is definitely smaller than the field value at the decreasing reversal of the unpatterned area. At the increasing branch of the unpatterned area the estimated $1/2H_d$ is already comparable to the external field. This increases the influence of anisotropy and exchange energy in minimizing the total energy. The formation of a large number of domain walls becomes more favorable, causing a stronger average pinning with a distinct shift of the increasing branch towards larger H_c. Consequently, the decreased H_{EB} in the patterned sample is significantly determined by the influence of demagnetization on the FM spin structure.

Micromagnetic simulations of patterned NiFe-CoO bilayers point towards a similar direction [123]. However, in contrast to our experiments the simulated H_{EB} of small elements is larger than those of the unpatterned films. This discrepancy is not solved, yet, but might be due to different material parameters and pattern sizes in the simulation and our experiment. Also an unconsidered depth dependence in the FM spin structure might have an influence, like in the unpatterned film.

In summary, Fe nanodots in contact with an FeF_2 antiferromagnetic substrate exhibit decreased H_{EB} and increased H_c compared with continuous films, although the diameter of Fe dots is much larger compared to the AF domain size, and therefore a change of AF/FM exchange interaction is not expected. This effect originates in patterned EB systems when the changes in the demagnetizing energy compared to other important energies in the problem (Zeeman, exchange and anisotropy) becomes a dominant factor.

III.H Exchange Biased Vortex State

As shown in the previous section, magneto-static effect plays an important role in modifying the magnetization reversal of patterned structures. A most significant demonstration of magnetostatic effect in nanostructures is the vortex state, among other interesting spin configurations. It arises from the competition between magnetostatic and exchange energy [124]. For dots of certain sizes, when the magnetic field is reduced from saturation, a vortex core nucleates at one edge, reversibly moves across the dot and annihilates on the other side. In this case, the reversible movement of the vortex core often manifests in the hysteresis loop as a straight line through the origin. This has been studied in detail both experimentally and using micromagnetic simulations [125, 124]. In this work, we modify the reversal process of a FM by shaping it into sub-micron dots to investigate its influence on the EB effect.

Fe(30 nm)/FeF_2(20 nm) bilayers capped with 4 nm Al were prepared on top of a single crystal MgO(100) substrate by e-beam evaporation. Square arrays of circular Fe dots with diameter d = 300 nm or 600 nm and center-to-center distance of $a = 2d$ were prepared by e-beam lithography and subsequent Ar^+-ion milling. By controlling the ion-milling time, two different types of systems were prepared from the same bilayer sample: in the type A sample, only the Fe layer was nanostructured, while in type B both Fe and FeF_2 were nanostructured (see Figure III.26(a)). In both cases, a small area was kept unexposed to the ion beam to allow comparison of the dots and continuous film on the same sample. The dot arrays were imaged by atomic force microscopy as shown in Figure III.26(b). The samples were initially cooled from 150 K to 10 K through the Néel temperature T_N = 78.4 K of FeF_2 in an in-plane cooling field H_{FC} = 5 kOe. Magnetic measurements were carried out using low-temperature magneto-optical Kerr effect (MOKE) both below and above the Néel temperature (T = 10 and 90 K) to compare the reversal behavior when the AF is either ordered or in a paramagnetic

state, respectively. The laser beam was focused to 50 to 100 μm, much larger than the dot size, thus measuring the average behavior of a large number of dots ($\sim 10^4$ dots).

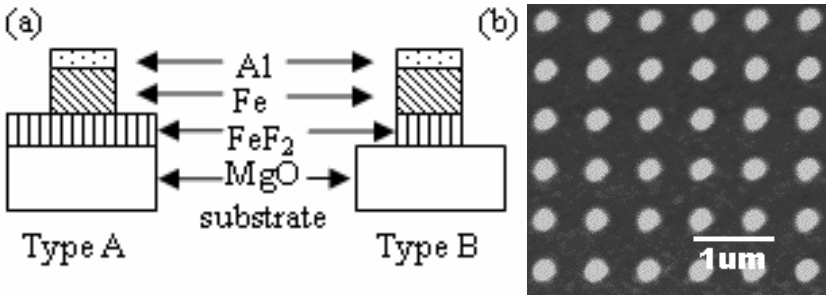

Figure III.26: (a) Schematic of type A and B samples. (b) Atomic force microscopy image of a type B sample with dot diameter 300 nm. The array size is 80×80 μm^2.

The results from the two types of dot arrays and the film are summarized in Table III.1. Figure III.27 shows the measurement on sample A for Fe dots of 300 nm (a) and 600 nm (b) diameter respectively, at $T = 10$ and 90 K. At $T = 90$ K, the continuous Fe/FeF_2 film exhibits a square loop (upper inset of Figure III.27(a)). The 300 nm dot array clearly shows that the two hysteresis branches almost join at zero field, which is characteristic of the vortex state [125]. The 600 nm dot array shows a sheared loop at 90 K without any vortex signature. The observed shearing of the loop is generally believed to come from shape anisotropy or the distribution of switching fields [126]. When the sample is cooled to $T = 10$ K, the exchange bias of the continuous film manifests as a clear loop shift by $H_{EB} = -97$ Oe. While the 600 nm dots exhibits $H_{EB} = -96$ Oe similar to that of the continous film, the 300 nm dot array shows a smaller EB field $H_{EB} = -55$ Oe. The coercivity is enhanced upon biasing for both dot sizes. The collapse of the two hysteresis branches in the 300 nm dot leads to a smaller coercivity than the 600 nm dots. Moreover, patterning also leads to an increased coercivity compared with the unpatterned film possibly due to the increased importance of the shape anisotropy and pinning.

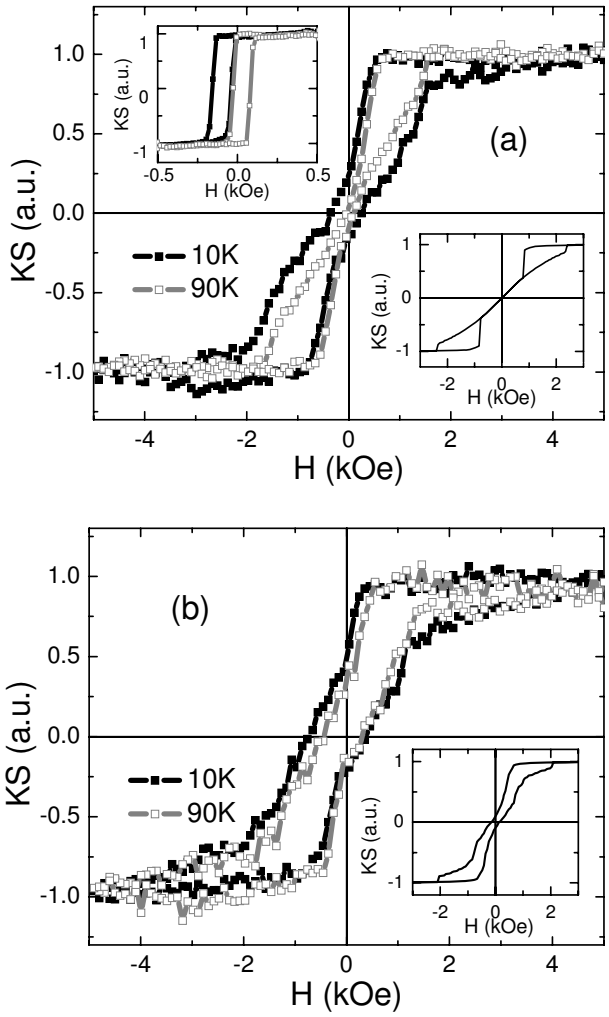

Figure III.27: Kerr effect signal (KS) vs. magnetic field H from type A sample (Fe dots on FeF_2 film) with dot diameter 300 nm (a) and 600 nm (b) at $T = 10$ K (solid squares) and 90 K (open squares). The upper inset of (a) shows the data on the continuous film of the same sample. The lower insets of (a) and (b) show corresponding data from micromagnetic calculations in the unbiased case.

Table III.1: Coercivities H_C at $T = 10$ K and 90 K, and exchange bias field H_{EB} at $T = 10$ K for dot arrays and continuous film determined from the inflection points of the hysteresis loops. The error is close to 5 Oe for the continuous film, 10 Oe for type A dots, and 20 Oe for type B dots.

Type	H_C (Oe) at $T = 90$ K	H_C (Oe) $T = 10$ K	H_{EB} (Oe) $T = 10$ K
A, $d = 300$ nm	99	302	-55
A, $d = 600$ nm	395	546	-96
B, $d = 300$ nm	299	433	-110
B, $d = 600$ nm	768	875	-105
Continuous Film	54	60	-97

The type B samples (Figure III.28) show much larger coercivities than type A with a similar trend in size and temperature as shown in Table I. This may be attributed to increased structural defects and pinning due to the high etching rate of the FeF_2 compared with Fe. Contrary to type A, the 300 nm type B dots do not show the vortex-characteristic narrowing in the hysteresis loop close to zero field, showing that the increased pinning modifies the reversal behavior with the vortex becoming pinned or inhibited. Moreover, the EB field becomes almost independent of the lateral size, i.e. -110 and -105 Oe for the 300 nm and 600 nm dot array respectively, which is comparable with the continuous film, $H_{EB} = -97$ Oe. Shaping the AF has little influence on the EB field possibly because the AF domain size in twinned FeF_2 is estimated to be close to the grain size of about 10 nm [35], which is much smaller than either dot dimension.

The above results imply several important features related to EB. First, the 300 nm dots of type A with a vortex-characteristic hysteresis exhibit a reduction of the EB field. For other cases, regardless of dot sizes and types, the unidirectional anisotropy shifts the hysteresis loops by $H_{EB} \approx -100$ Oe. Second, both dot types show larger coercivities at $T = 10$ K than $T = 90$ K. This observation is consistent with the coercivity enhancement commonly observed in EB systems. It should

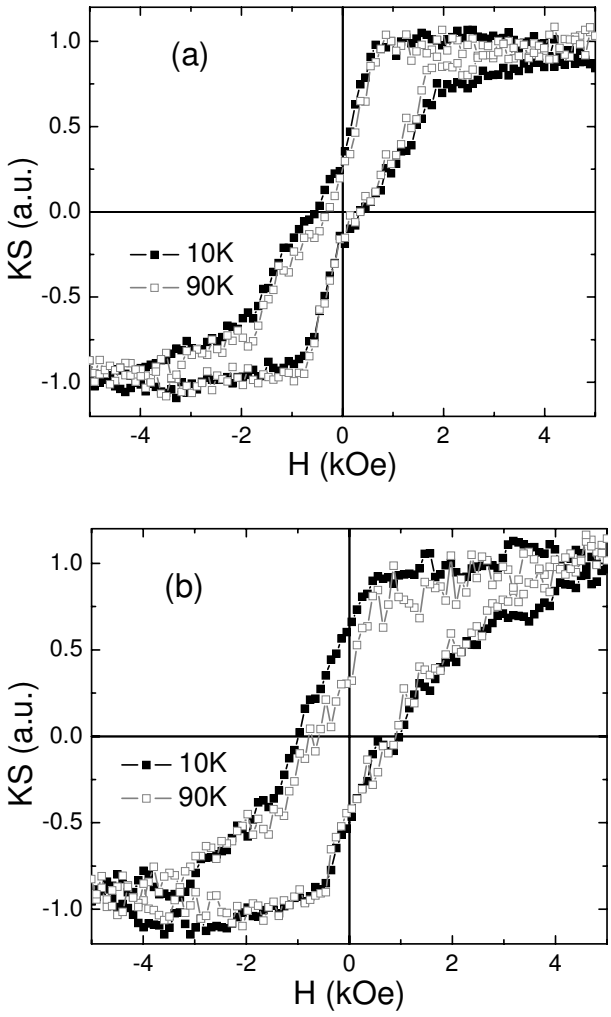

Figure III.28: Kerr signal (KS) vs. magnetic field H from type B sample with dot diameter 300 nm (a) and 600 nm (b) at $T = 10$ K (solid squares) and 90 K (open squares).

be mentioned that several groups have reported a decrease of the EB field upon nanostructuring [74, 75, 44], while the reverse situation was also observed [41]. A possible scenario is that different parts of in the thickness-diameter diagram have different size dependences of the EB. Additional experimental studies are needed to clarify this issue.

To understand the reversal behavior of the dots, we performed micromagnetic calculations [70]. First, the FM dots without the AF are simulated. The $d = 600$ nm and $t = 30$ nm Fe dots show a reversal through a multi-domain state with a similar magnetization curve as in our experiment (lower inset of Figure III.27 (b)). For the 300 nm dots, the shape anisotropy dominates its behavior and a flux-closure vortex state is encountered (lower inset of Figure III.27 (a)). This confirms our experimental observations that in type A dots a vortex state is observed in the 300 nm dots, but not in the 600 nm ones. The incomplete collapse in the experiment may arise from deviations from circular shape of the dots, roughness, structural variations from dot to dot and other imperfections.

To investigate the influence of the vortex state on the EB, we assume that 4% of randomly distributed, rigid, uncompensated AF interfacial spins are exchange coupled to the bottom layer of the FM [37, 38] because of the very high anisotropy of FeF_2 [61]. The interfacial coupling strength is taken to be the AF coupling in the FeF_2, $J_{FM/AF} = -0.45$ meV [61]. The results of these simulations are presented in Figure III.29, where the 300 nm dot shows an EB field of -206 Oe, compared with -505 Oe for the continuous film. The same trend was found experimentally. Figure III.30 shows the corresponding spin structure of the biased dot at different fields along the increasing hysteresis branch. There is virtually no difference in the reversal process compared to the unbiased case (see Fig. III.27 (a) inset) except an overall EB shift. This means the AF pinning spins act as a uniform EB field, and the magnetization loop resembles that of the unbiased case. Moreover, the vortex core is no longer at the center of the dot at zero field, but shifted to one side in the direction perpendicular to the bias field.

The reduction of the EB field for the vortex state can be understood since a flux closed state has only part of its spins pointing parallel to the net frozen interface moment of the AF, thus the total interfacial coupling energy is reduced. In other words, the exchange bias is associated with a term of the type $S_{AF} \cdot S_{FM}$ [89], which is reduced in the vortex state. On the other hand, the above simulation does not show any coercivity increase upon biasing as found in the experiment. Hence, the ansatz considering only few uncompensated unidirectional frozen AF moments is too simple. This might be related to the lack of a reversible component of AF interfacial spins leading to an additional contribution to the coercivity. This discrepancy can also come from variations among individual dots, e.g. distribution of defect pinning and exchange coupling.

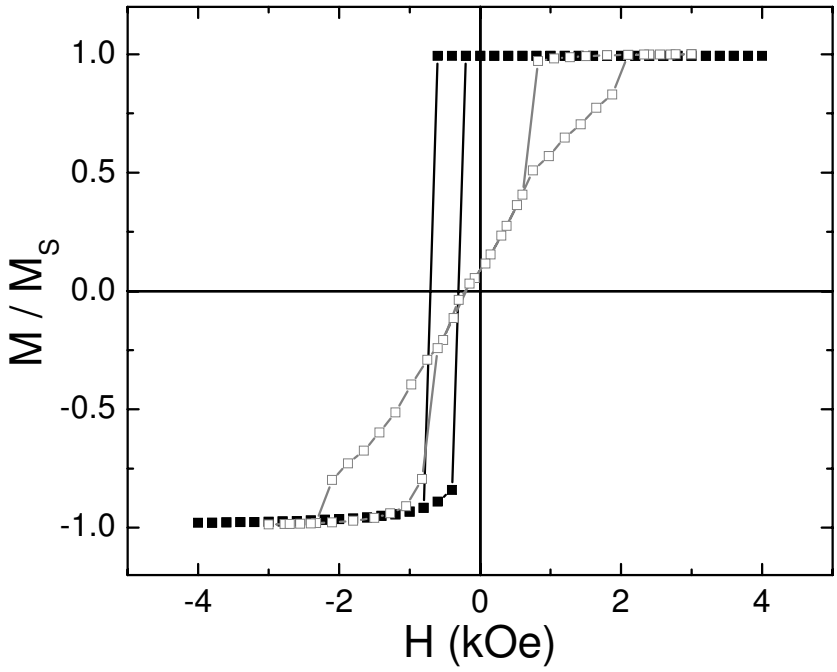

Figure III.29: Micromagnetic simulations of a FM film (solid square) and a 300 nm type A dot (open square) subject to rigid AF uncompensated spins. The thickness in both cases is 30 nm.

In summary, we have studied the reversal behavior of sub-micron Fe dots exchange biased to FeF_2 using low temperature MOKE. We varied the diameter of dots (d = 300 and 600 nm) as well as the type of structuring, i.e. Fe dots on

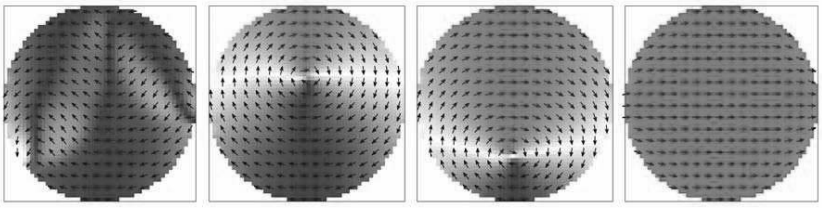

Figure III.30: Spin configurations of a 300 nm type A dot in external fields of -825, -600, 975, and 2550 Oe along the increasing hysteresis branch from the micromagnetic simulation. The dark-gray, white and black color codes refer to M_x (horizontal direction) equal to 1, 0 and -1, respectively.

top of a continuous FeF_2 film (type A) or both Fe and FeF_2 patterned (type B), while the thickness was kept constant, $t_{FM} = 30$ nm, $t_{AF} = 20$ nm. We find that a vortex state leads to an EB field smaller than in all other cases. This result is consistent with micromagnetic simulations.

III.I Acknowledgement

Chapter III, in part, is a reprint of the material as it appears in Zhi-Pan Li, Oleg Petracic, Rafael Morales, Justin Olamit, Xavier Batlle, Kai Liu, and Ivan K. Schuller, "*Asymmetric Reversal in Inhomogeneous Magnetic Heterostructures*," Phys. Rev. Lett. **96**, 217205 © 2006 The American Physical Society, where the dissertation author was the first author, and Zhi-Pan Li, Oleg Petracic, Johannes Eisenmenger, and Ivan K. Schuller, "*Reversal behavior of exchange-biased submicron dots*," Appl. Phys. Lett. **86**, 072501 © 2005 American Institute of Physics, where the dissertation author was the first author, R. Morales, Zhi-Pan Li, O. Petracic, X. Batlle and Ivan K. Schuller, "*Magnetization depth dependence and reversal processes in exchange coupled FeF_2/FM bilayer*," Appl. Phys. Lett. **89**, 072504 © 2006 American Institute of Physics, where the dissertation author was the second author, and Johannes Eisenmenger, Zhi-Pan Li, Waldemar A. A. Macedo, and Ivan K. Schuller, "*Exchange Bias and Asymmetric Reversal in Nanostructured Dot Arrays*," Phys. Rev. Lett. **94**, 057203 © 2005 The American Physical Society, where the dissertation author was the second author. The

co-authors in this publication directed, supervised, and co-worked on the research which forms the basis of this chapter.

IV

Thermally induced Spontaneous Magnetization Reversal

IV.A Introduction

Nanoscience has become an active area of research due to the breakdown of naive expectations when one or more length scales are reduced to the nanoscale. Moreover, nanostructuring combined with proximity effects may produce emergent phenomena that are neither found in homogeneous materials nor predicted by simple finite size scaling laws. Conventional semiconductor heterostructures at the nanoscale, result in 2-dimensional electron gases and quantum dots, which exhibit phenomena such as coloumb blockade and the fractional quantum Hall effect [127]. Nanoscale heterostructures of ferromagnets (FMs) with semiconductors, normal metals, and antiferromagnets (AFs) give rise to ferromagnetic semiconductors [128], giant magnetoresistance [129], and exchange bias (EB) [1], which are the basis of the novel field of spintronics [130, 131].

In this chapter, we present a novel and unusual phenomenon in which, under a constant magnetic field, a nanoscale FM in intimate contact with an AF, spontaneously reverses its magnetization with decreasing temperature. This is contrary to the general understanding that an applied field and an electric current

are the only two ways to fully reverse the orientation of a ferromagnet's magnetization [132]. We observe that below an upper limit, larger applied magnetic fields induce larger magnetization reversal. Interestingly, the temperature dependence of the magnetization is hysteretic, thus allowing FM switching by thermal cycling.

We observe this phenomenon in exchange bias heterostructures FeF_2/FM, where positive EB has been routinely observed (Section IV.B). The positive EB has been attributed to the antiferromagnetic interfacial coupling. As AF Zeeman energy dominates the coupling, positive EB can be induced. We believe that the spontaneous FM magnetization reversal is due to the competition between the AF interfacial coupling and the FM Zeeman energy. Using this interpretation and with knowledge of the temperature dependence of coercivity and exchange bias field, the reversal temperature is quantitatively estimated, and fit well with the experiment.

This spontaneous reversal is sensitive to time-dependent cooling protocols. Two protocols were studied: cooling with uniform speeds, or fast cooling to around T_N followed by waiting at the temperature and then fast cooling to a low temperature. We find that a slower cooling or longer waiting close to T_N leads to a larger magnetization reversal. Thermal cycling around T_N leads to successive reversals with the reversal magnitude exponentially decaying. We attribute this dynamic behavior of spontaneous reversal to the competition of forming an AF or FM parallel domain wall and the interfacial coupling at T_N when the AF is becoming ordered. Qualitative description of positive vs. negative exchange bias is also proposed.

Besides the novelty of reversing a FM by thermal cycling in a constant field, it also questions the present interpretation of positive EB. The current theory of positive EB predicts the FM moment should be smaller than the total AF uncompensated moments when the thermal reversal occurs. However, no significant AF moments are found experimentally. We propose the mechanism of positive EB should also include parallel FM and AF domain wall formation energy, as we

demonstrated earlier, to account for the thermally induced FM reversal.

IV.B Thermally induced Spontaneous Magnetization Reversal

Epitaxial exchange biased FM/AF samples were grown on MgF_2 (110) substrates by e-beam evaporation with a structure ZnF_2 (30nm) / FeF_2 (50nm) / FM (3nm) /Al (3nm), with FM = Ni or Co. The ZnF_2 is a paramagnetic buffer layer for the epitaxial growth of antiferromagnetic FeF_2 (T_N = 78 K). The Al capping layer was used to prevent oxidation. ZnF_2 and FeF_2 were grown at 300°C, the FM and Al at 150°C, all at 0.05 nm/s with a base pressure of 10^{-7} Torr. X-ray diffraction revealed that the FeF_2 grows epitaxially untwined in the (110) orientation, while the FM is polycrystalline. The magnetization was measured using superconducting quantum interference device (SQUID) magnetometry with the magnetic field applied parallel to the [001] easy axis of FeF_2 in the sample plane. The easy axis of the FM coincides with FeF_2 [001]. At T = 10 K, the FeF_2 / Ni sample exhibits positive EB with H_{EB} = 4.1 kOe when cooled in $H_{FC} >$ 0.5 kOe, and shows both positive and negative EB of $H_{EB} = \pm$4.1 kOe for H_{FC} between 0 and 0.5 kOe (Fig. IV.1 inset). The FeF_2 / Co sample shows solely positive or negative EB for H_{FC} above 1 kOe and below 0.1 kOe, respectively, with coexistence of both between these fields. Spontaneous reversal only occurs in samples displaying positive EB, either entirely or partially.

At T = 150 K, the FeF_2 / Ni sample shows a typical square magnetic hysteresis (M-H) loop [55]. The sample was first saturated at this temperature by a 5 kOe magnetic field, then subject to a constant H_{FC} while saturated. The sample was then cooled to 10 K, then heated to above 150 K. Fig. IV.1 shows the magnetization as the temperature was changed for two constant H_{FC} (M-T curves). For H_{FC} = 1 kOe, the magnetization starts to reverse at 65 K (below T_N), reaches zero at 57 K, then fully reverses, aligning anti-parallel to H_{FC} at 50 K.

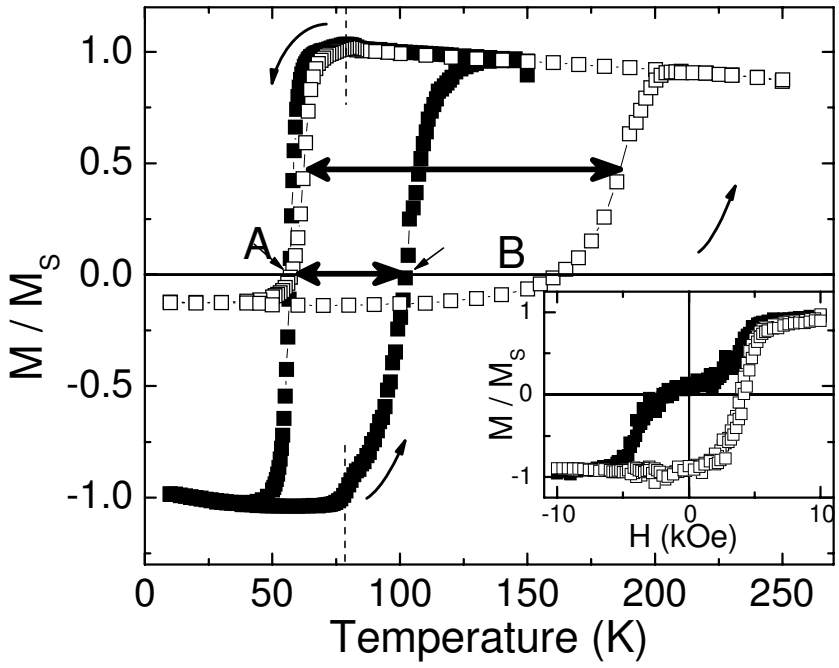

Figure IV.1: Normalized magnetization of FeF_2 (50 nm) / Ni (3 nm) measured under temperature sweep in 1 kOe (solid squares) and 0.1 kOe (empty squares) by SQUID magnetometry. The dashed line marks $T_N = 78$ K of FeF_2. The width ΔT_C is marked by thick horizontal arrows at ¡M¿. Points A and B are the reversal temperatures 57 K and 104 K for $H_{FC} = 1$ kOe (see Fig. IV.3 for more details). (Inset) Magnetization hysteresis loops for FeF_2/Ni at T = 10 K for $H_{FC} = 0.1$ kOe (solid squares) and 1 kOe (empty squares).

With increasing temperature, the FM magnetization increases to zero at 104 K, then restores its full alignment with H_{FC} at ≈120 K. The net result is a significant M-T hysteresis with a full thermal width at half the reversed magnetization T_C = 47 K. The hysteresis is more pronounced if cooled in a lower field of H_{FC} = 0.1 kOe. With this cooling field, the Ni magnetization reverses by 55% relative to full reversal at 63 K, and returns to its original state at 185 K, giving T_C = 123 K. A similar effect was also observed in the FeF_2 / Co sample. At H_{FC} = 0.3 kOe, the Co magnetization reverses by 68% at 55 K and switches back at 114 K, giving T_C = 59 K. This thermal hysteresis is reminiscent of a FM switching between two saturated states in response to a sweeping external magnetic field or electric current [133] at constant temperature.

The change in the magnetization, $\Delta M = M(T = 150\text{ K}) - M(T = 10\text{ K})$, and the width T_C of the M-T hysteresis can be tuned by H_{FC}, as shown in Fig. IV.2. For both FMs, ΔM increases with increasing H_{FC} until $H_{FC} \approx 1$ kOe, after which it decreases until the spontaneous reversal is no longer observed. T_C rapidly decreases with increasing H_{FC} initially (below ≈1 kOe), then slowly tends toward zero for higher H_{FC} (Fig. IV.2b).

The thermally induced FM reversal results from two competitions: one between the antiferromagnetic (AF) interfacial coupling $\mathcal{H}_{int}$ and the AF Zeeman energy $\mathcal{H}_{AF-Zeeman}$, and the other between the coupling $\mathcal{H}_{int}$ and the FM Zeeman energy $\mathcal{H}_{FM-Zeeman}$. The former determines the orientation of the frozen interfacial AF uncompensated moment, S_{AF}, and establishes positive EB; with the AF thus frozen, the latter determines the orientation of the FM.

Positive EB arises when the interfacial AF moment freezes in the magnetic field direction under a cooling field large enough to overcome the AF interfacial coupling [8]. When the interfacial coupling dominates AF Zeeman energy for small cooling fields, the uncompensated AF moment orients opposite to the field and gives rise to negative EB. At intermediate cooling fields, positive and negative EB coexist due to spatially inhomogeneous interfacial coupling. In this case, double

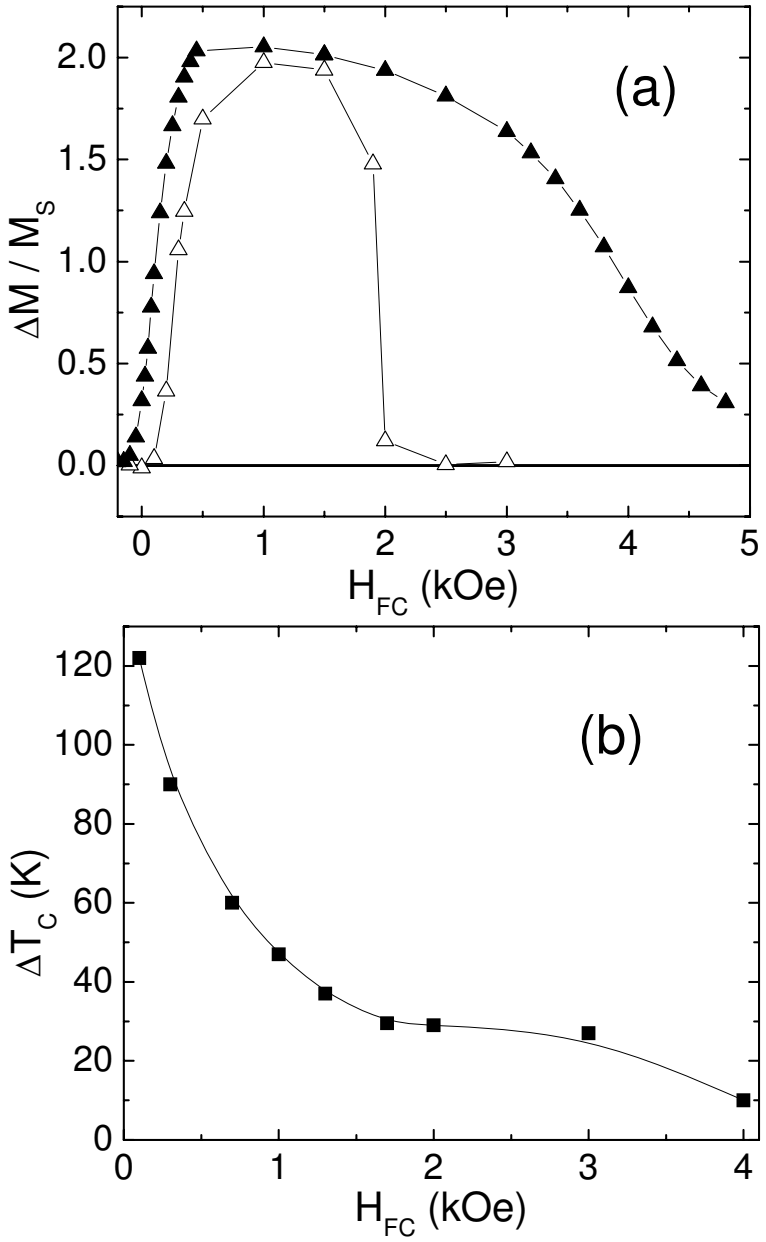

Figure IV.2: (a) Magnetic cooling field dependence of the magnetization change ΔM during fast thermal cycling normalized by the saturation magnetization M_S (insert a value) for FeF_2 / Ni (solid triangles) and FeF_2 / Co (open triangles). A cooling speed dependence results in systematic and controllable differences of up to 10% in M. (b) Magnetic field dependence of the full thermal width ΔT_C at $< M >$. Lines are guides to the eye.

hysteresis loops are observed if the length scale of this inhomogeneity is much larger than the FM domain wall width [55, 57]. In our system, 50% of the sample exhibits positive EB for $H_{FC} = 0.05$ kOe. The origin of this surprisingly low onset cooling field for positive EB is thus far unknown.

Once positive EB is established, the reversal of the FM is governed by the competition of the FM Zeeman energy with the AF interfacial coupling. The FM Zeeman energy favors the FM aligning parallel to H_{FC}, while positive frozen SAF and the AF interfacial coupling favors an antiparallel orientation. SAF, and thus H int, increases as the AF becomes increasingly ordered with decreasing temperature below T_N, as evidenced by the increase of H_{EB} (Fig. IV.3 inset). $\mathcal{H}_{int}$ eventually overcomes the FM Zeeman energy, causing the FM to spontaneously reverse its magnetization. In the case of purely negative EB (negative S_{AF}), the AF interfacial coupling assists in aligning the FM magnetization parallel to H_{FC}, and thus will not lead to spontaneous reversal.

This competition can also explain the unusual low field behavior: i.e. increasing H_{FC} causing M to increase (Fig. IV.2). When a larger H_{FC} is applied, the positively EB regions of the sample increase in area at the cost of negatively EB regions. As a result, a larger percentage of the FM reverses. If the field is large enough that the entire sample exhibits positive EB, SAF can no longer increase. In this case, with increasing field and thus increasing FM Zeeman energy, M decreases and ultimately vanishes when $\mathcal{H}_{FM-Zeeman} > \mathcal{H}_{int}$.

Quantitatively, the two competing energies that govern the reversal process can be expressed as $\mathcal{H}_{FM-Zeeman} = -\mu_0 H_{FC} M_{FM} t_{FM}$, and $\mathcal{H}_{int} = -J_{FM/AF} S_{AF}$. S_{FM}, where M_{FM} and t_{FM} are the magnetization and thickness of the FM, respectively, S_{AF} and S_{FM} are the AF and FM interfacial moment per unit interface area, and $J_{FM/AF} < 0$ is the interfacial coupling between the AF and FM. In order for the interfacial coupling to reverse the FM magnetization, it also has to overcome an energy barrier, $\mathcal{H}_{barrier}$, between the two saturated states of the FM. This energy barrier is determined by the intrinsic FM anisotropy, anisotropy induced by

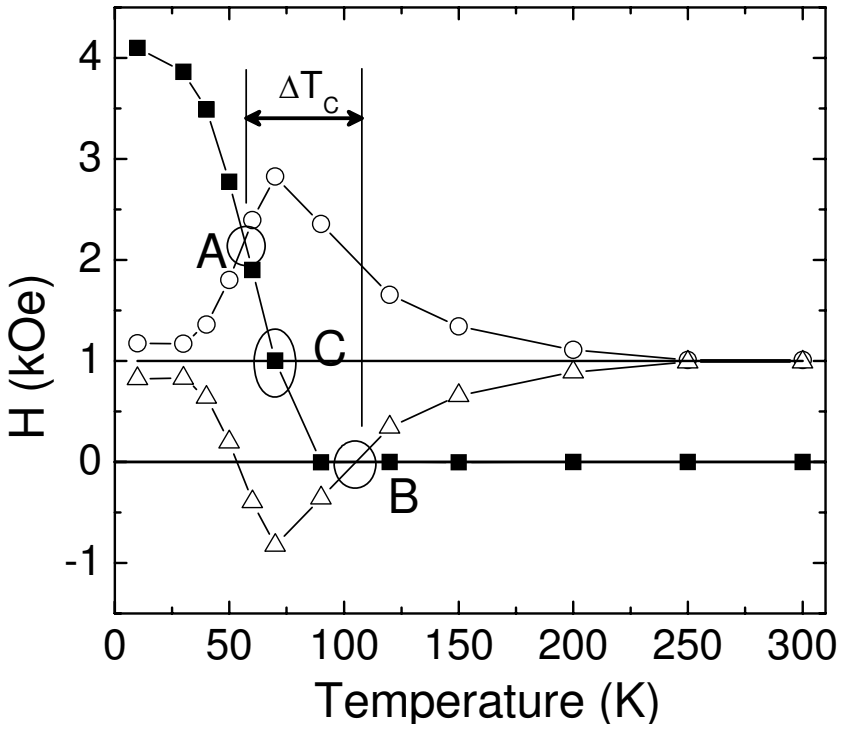

Figure IV.3: Exchange bias H_{EB} (solid squares), $H_{FC}+H_C$ (empty circles), $H_{FC}-H_C$ (empty triangles) as functions of temperature. The cooling field H_{FC} is marked by the horizontal line at 1 kOe. Points A and B mark the reversal temperatures with FM anisotropy considered, in agreement with the position of points A and B in Fig. IV.1. Point C refers to the reversal temperature for a negligible FM reversal barrier.

the interfacial coupling, and the energy related to domain formation. Spontaneous reversal occurs when $|\mathcal{H}_{int}| > |\mathcal{H}_{FM-Zeeman}| + \mathcal{H}_{barrier}$, and aligns with the field when $|\mathcal{H}_{FM-Zeeman}| > |\mathcal{H}_{int}| + \mathcal{H}_{barrier}$. Adopting the Meiklejohn-Bean model [1, 2] allows us to rewrite the interfacial coupling as $\mathcal{H}_{int} = \mu_0 H_{EB} M_{FM} t_{FM}$, where the sign refers to the sign of S_{FM}. Thus for negligible H barrier, the reversal should occur when $H_{EB}(T) = H_{FC}(T)$ for both cooling and heating, without any hysteresis. Fig. IV.3 shows H_{EB} and H_{FC} as functions of temperature for FeF_2 / Ni with $H_{FC} = 1$ kOe. The condition $H_{EB} = H_{FC}$ is satisfied at point C with $T = 70$ K. Experimentally, $\mathcal{H}_{barrier}$ is not negligible evidenced by the significant coercivity H_C enhancement around T_N (Fig. IV.3). This H_C enhancement is attributed to short-range order in the AF [85, 89]. Using $\mathcal{H}_{barrier} = \mu_0 H_C M_{FM} t_{FM}$, the reversal condition becomes $H_{EB}(T) \approx H_{FC} \pm H_C(T)$, where positive and negative signs refer to cooling and heating, respectively. This leads to a lower reversal temperature for cooling and higher for heating than predicted by $H_{EB} = H_{FC}$. Fig. IV.3 shows that the reversal condition is satisfied at 57 K (point A) and 105 K (point B), for cooling and heating, respectively, in agreement with Fig. IV.1. While the details of the reversal process are unknown, this shows that the M-T hysteresis with a tunable width T_C originates from the temperature dependent interface-induced anisotropy.

The interfacial coupling energy must dominate the FM Zeeman energy for FM spontaneous reversal. This condition is experimentally realized using FMs with nanoscale thickness because $\mathcal{H}_{FM-Zeeman}$ (proportional to t_{FM}) can be tuned to be of the order of $\mathcal{H}_{int}$, which is thickness independent. Thus, increasing the FM thickness should lead to lower spontaneous reversal temperatures until the phenomenon disappears. In this case, the FM magnetization can no longer fully reverse; it may still exhibit reversal tendencies such as spontaneous rotation or domain formation with decreasing temperature.

To investigate this further, vector SQUID magnetometry was used to measure the longitudinal (parallel to H_{FC}) and transverse (perpendicular to H_{FC}

in the sample plane) components of the magnetic moment of a sample with 21 nm thick Ni on FeF_2. The temperature dependence of H_C shows that this sample exhibits a low reversal energy barrier: the peak coercivity $H_C = 0.15$ kOe at $T = 90$ K was small compared to 1.8 kOe for the 3 nm thick Ni samples. The approximate reversal condition $H_{EB} \approx H_{FC}$ is thus appropriate here. The two components were measured while cooling from $T = 150$ K to 10 K in $H_{FC} = 2$ kOe, and heating in the same field. In this cooling field, the sample exhibits positive EB with $H_{EB} = 1$ kOe. Coexistence of positive and negative EB is encountered for H_{FC} between 1 and 2 kOe, while only negative EB exists for H_{FC} less than 1 kOe. Since $H_{EB} < H_{FC}$ for $H_{FC} = 2$ kOe, the interfacial coupling cannot overcome the FM Zeeman energy, and thus no spontaneous reversal should be observed. The measurement showed a small reduction of the longitudinal and a large increase of transverse moment with decreasing temperature, with the total magnetic moment above $0.96M_S$ (Fig. IV.4). Therefore, although unable to fully reverse as in thin FMs, here the FM magnetization nearly coherently rotated away from the magnetic field direction by about 30 degrees. This FM spontaneous rotation was not hysteretic due to the small H_C, signature of small intrinsic and AF-induced anisotropy of the FM. A larger cooling field reduces the amount of rotation, similar to the behavior in the high field range of Fig. IV.2.

Although the above discussion explains the observed phenomenon, and correctly gives an estimate of reversal temperatures, it also leads to important open questions. The present understanding of positive EB implies that $|\mathcal{H}_{AF-Zeeman}| > |\mathcal{H}_{int}|$ below T_N. At the same time, the FM reversal condition requires $|\mathcal{H}_{FM-Zeeman}| < |\mathcal{H}_{int}|$ below the FM reversal temperature. Therefore, $|\mathcal{H}_{AF-Zeeman}|$ is larger than $|\mathcal{H}_{FM-Zeeman}|$ below the reversal temperature, or $m_{AF} > m_{FM}$, where m_{AF} refers to the uncompensated frozen AF moment. It is reasonable that when m_{AF} becomes larger than m_{FM}, the FM should reverse with m_{AF} in the field direction. This is similar to some ferrimagnet Gd-Co [134] and multilayer systems Co/Gd [135], which results from two antiferromagnetically coupled spin species compet-

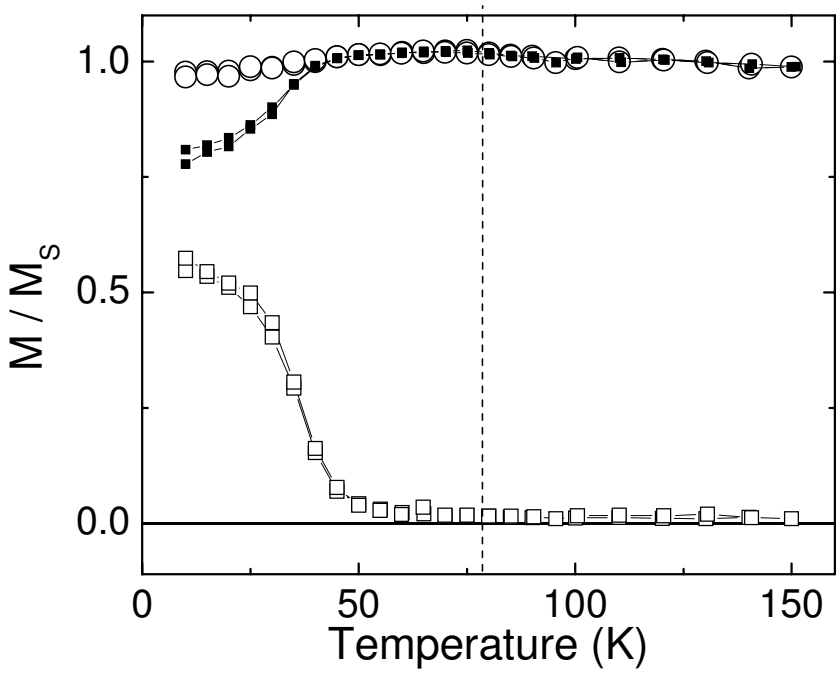

Figure IV.4: Normalized in plane longitudinal (solid squares), transverse (empty squares) and total (empty circles) magnetization of FeF_2 (50 nm) / Ni (21 nm) measured by vector SQUID magnetometry in thermal cycling with a 2 kOe magnetic field. T_N is marked by the dashed line.

ing to align with the field. In this case, the two magnetizations can be clearly identified and its total moment at a low enough temperature is always positive. However, in our FM/AF system, a large m_{AF}, would manifest as a significant shift of the M-H loop [51] along the magnetization axis, which was not observed (Fig. IV.1 inset). This suggests that m_{AF} is much smaller than m_{FM}, contrary to the previous argument, yet spontaneous reversal still occurs with a negative low-temperature magnetic moment for certain cooling fields. This contradiction implies that either spontaneous reversal is a novel metastable state, or the present positive EB model is incomplete. In this work, we demonstrate the slow dynamics and thermal training effect of the spontaneous reversal, which shows that the state with the FM reversed is thermodynamically stable, rather than a metastable state. A modified model for positive EB is proposed, which argues that it is the energy to form an AF parallel domain wall that competes with the interfacial coupling and partial FM parallel domain wall energy.

In summary, we report a novel temperature-driven phenomenon where, under a constant applied magnetic field, saturated magnetic heterostructures spontaneously reverse their magnetization. This phenomenon is observed when the heterostructure exhibits positive exchange bias. This reversal behavior shows a significant temperature hysteresis that can be tuned by the field applied during thermal cycling, in contrast to the conventional temperature-dependent hysteretic behavior of a FM under magnetic field cycling. This behavior not only provides another means for inducing ferromagnetic reversal beside magnetic fields and electric current, but also offers possible probes for buried interfaces and AF. Although the proposed interpretation is able to partially explain the phenomenon, it also leads to open questions due to our incomplete understanding of exchange bias in general.

IV.C Dynamics of Spontaneous Magnetization Reversal

In this section, we will demonstrate the slow dynamics and thermal training effect of the spontaneous reversal, and show that spontaneous reversal is energetically favored rather than metastable. The same Ni(3nm)/FeF_2(30nm) sample on a MgF_2 substrate was studied as in our previous section. Without loss of generality, only $H_{FC} = 0.1$ kOe is discussed, where the magnetization reverses by about 50% upon cooling.

Two different cooling protocols were studied. In the first (Fig. IV.5 inset), the sample was cooled from $T = 150$ K to 10 K with uniform cooling speeds ranging from 0.1 K/min to 10 K/min. The second protocol cools the sample from 150 K to an intermediate temperature T_w at 10 K/min, holds the temperature $T = T_w$ for τ minutes, then cools to 10 K at 10 K/min (Fig. IV.6 inset). After the sample temperature is stable at 10 K, the magnetization $M(T = 10\text{ K})$ is measured.

Fig. IV.5 shows the dependence of magnetization reversal $\Delta M = M(T = 10\text{ K}) - M(T = 150\text{ K})$ on the cooling speed. Slower cooling leads to a larger $|\Delta M|$. With the largest cooling speed 10 K/min, the FM reverses by $\Delta M = -0.9M_S$. When cooled at 0.1 K/min, $|\Delta M|$ increases by $0.2M_S$. Moreover, the reversal magnitude is most time-sensitive around T_N, as demonstrated by the second cooling protocol. The dependence of ΔM on the wait temperature T_w and wait time τ shows that the largest $|\Delta M|$ was achieved at $T_w = 80$ K closest to T_N (Fig. IV.6). As τ increases, $|\Delta M|$ increases from $0.9M_S$ until $\tau = 30$-35 minutes, when it saturates at $1.25M_S$. For $T_w = 85$ K, $|\Delta M|$ only changes by $0.08M_S$ after waiting for 50 minutes. For $T_w = 75$ K, $|\Delta M|$ saturates after ~ 15 minutes at $1.1M_S$. This time-dependent reversal behavior was not observed when waiting at $T = 63$ K, at which the FM reverses. Measurement using these two cooling protocols shows that spontaneous magnetization reversal exhibits slow dynamics with a relatively long time scale. More importantly, the fact that the dynamics are most pronounced around T_N hints toward the significance of the establishment of AF domain states

in this effect.

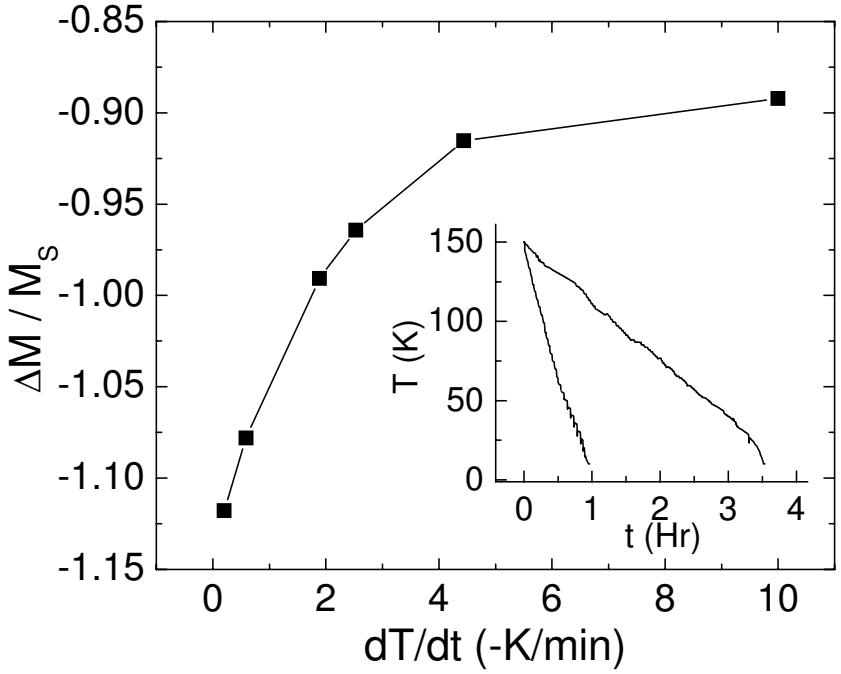

Figure IV.5: Normalized reversal magnetization $\Delta M/M_S$ as function of uniform cooling speed dT/dt for $H_{FC} = 0.1$ kOe. (Inset) Temperature T vs. time t for cooling from $T = 150$ K to 10 K at uniform speeds, 2.5 and 0.6 K/min. Lines are a guide to the eye.

To ensure that the dynamics does not come from experimental artifacts, several tests were performed. First, measuring the magnetic moment in the SQUID at intermediate temperatures involves moving the sample through the SQUID coils by 4 cm, thus subjecting the sample to magnetic field inhomogeneity. To exclude this influence, the same cooling procedure was preformed but without measuring magnetization at intermediate temperatures. The reversal magnitude ΔM only differs by $3 \times 10^{-4} M_S$, much smaller than ΔM variation (up to $0.2 M_S$) due to various cooling speeds. Second, occasional temperature fluctuations during cooling may also be a source of artifacts. To check this, the sample was heated from 10 K to a temperature T_x, then cooled back down to 10 K. When $T_x \leq 80$ K, ΔM varies by no more than $0.01 M_S$, still too small to account for the ΔM variation found earlier (Fig. IV.7). When $T_x > 80$ K, a significant second magnetization

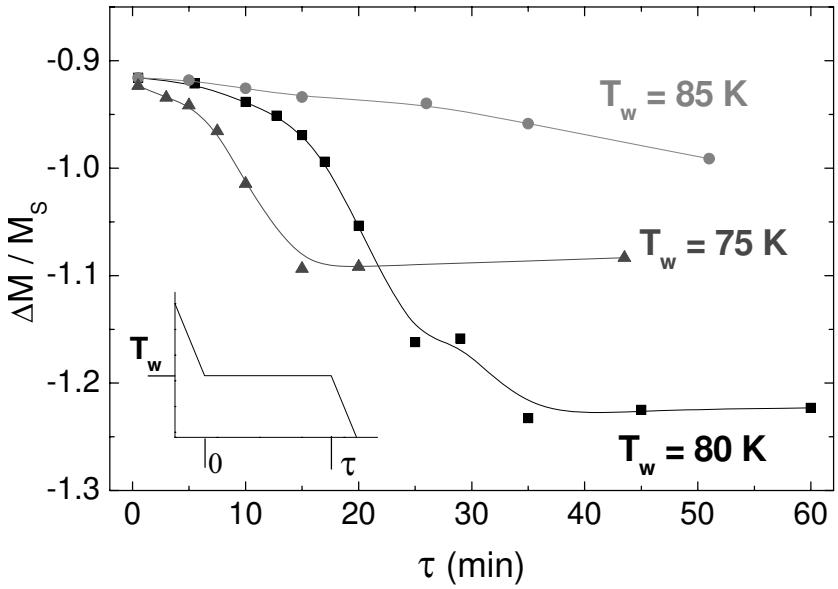

Figure IV.6: Normalized magnetization reversal $\Delta M/M_S$ as a function of wait time τ at temperatures T_w = 75(triangles), 80(squares), and 85(circles) K for $H_{FC} = 0.1$ kOe. (Inset) Schematic of the cooling protocol from $T = 150$ K to 10 K with waiting around T_N for time τ. Lines are a guide to the eye.

reversal is observed, which will be discussed in detail later. This demonstrates that the dynamics of spontaneous reversal being time-sensitive is not an experimental artifact but critically related to AF phase transition.

A larger reversal for slower cooling rates and longer waiting around T_N suggests that it is thermodynamically favorable for the FM to reverse. However, the slow evolution of the system toward a larger reversal implies the presence of large energy barriers. The second large reversal during thermal cycling from $T_x > 80$ K in the above study (Fig. IV.7) suggests that thermal activation can assist the system to overcome the energy barrier.

Thermal training effect refers to successive magnetization reversal when the system is thermally cycled between above and below T_N of the AF in a constant magnetic field H_{FC}. With the FM saturated, the sample was first cooled in H_{FC} = 0.1 kOe from 150 K to 10 K at 0.1 K/min, followed by heating to 150 K, just below the temperature for the FM to reverse back along the field direction. After that, the sample was cycled between 150 K and 10 K. The magnetic field was held constant

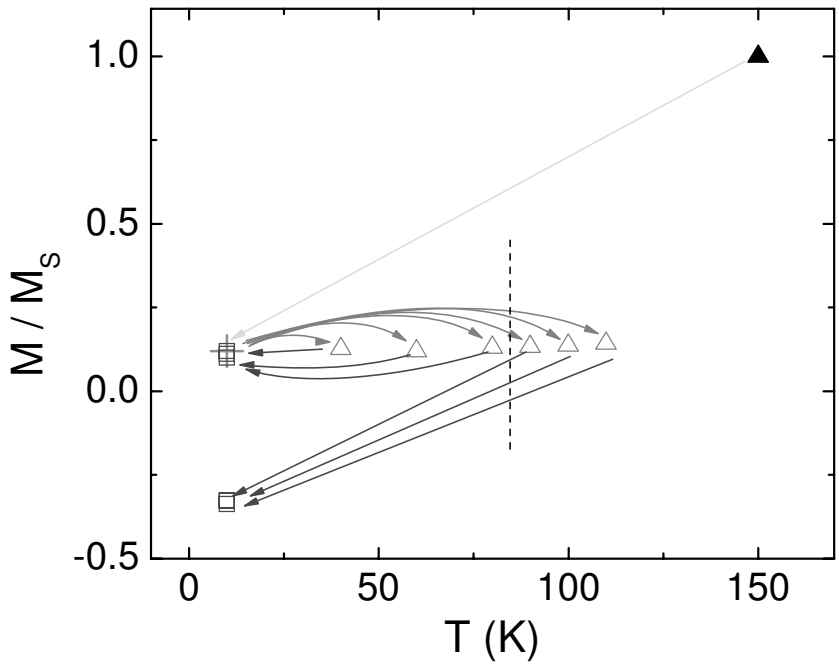

Figure IV.7: Normalized magnetization M/M_S was measured after each step of the three-step thermal cycle. (1) Cool from $T = 150$ K to 10 K (cross); (2) Warm up to various temperatures ranging from 40 to 110 K (triangles); (3) Cool back down to 10 K (squares). Two different behaviors were found in step 3, which is reversible when cooled from below 80 K, and irreversible when cooled from above 80 K. The dash line marks the separation of the these two regimes, close to T_N. The lines are schematics of the measurement sequence.

at $H_{FC} = 0.1$ kOe throughout the thermal cycles. The FM reverses in every cooling step, with decreasing reversal magnitude, until the total magnetization reversal reaches $1.8M_S$, which is $0.7M_S$ more than the first cycle (Fig. IV.8).

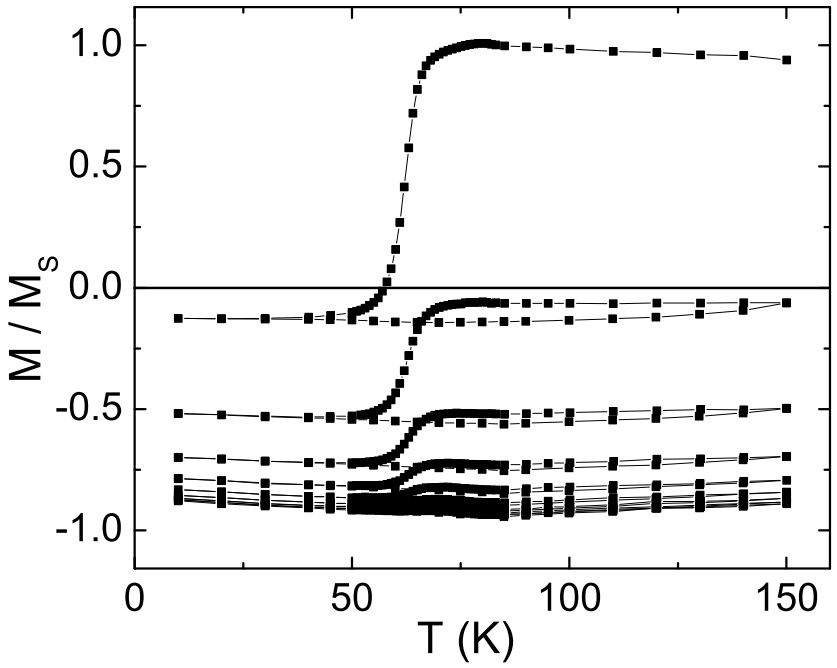

Figure IV.8: Normalized magnetization M/M_S was measured as the temperature is cycled between 150 K and 10 K in a 0.1 kOe magnetic field. In total, nine cycles were conducted. Lines are a guide to the eye.

As found earlier, the magnetization reversal magnitude depends on both the cooling speed and cooling field H_{FC}. Fig. IV.9 shows the dependence of $M(10\text{K})$ on the number of cycles N for different H_{FC} and cooling speeds. For all cases, they follow an exponential dependence, $M_N(10\text{K}) = M_\infty + (M_S - M_\infty)\exp(-N/\eta)$ (Fig. IV.9), where M_∞ is the convergent $M(10\text{K})$ when $N \to \infty$, and η is a characteristic cycle number for each H_{FC} and cooling speed. $M_N(10\text{K})$ for $N = 0$ is defined as M_S. M_∞ is found to be linearly dependent on H_{FC} for a constant cooling speed (Fig. IV.9 inset). A larger H_{FC} also causes a smaller η, or faster approaching of $M(10\text{K})$ to M_∞. This is understandable since a larger magnetic field can assist overcoming the reversal energy barrier, thus faster approaching M_∞.

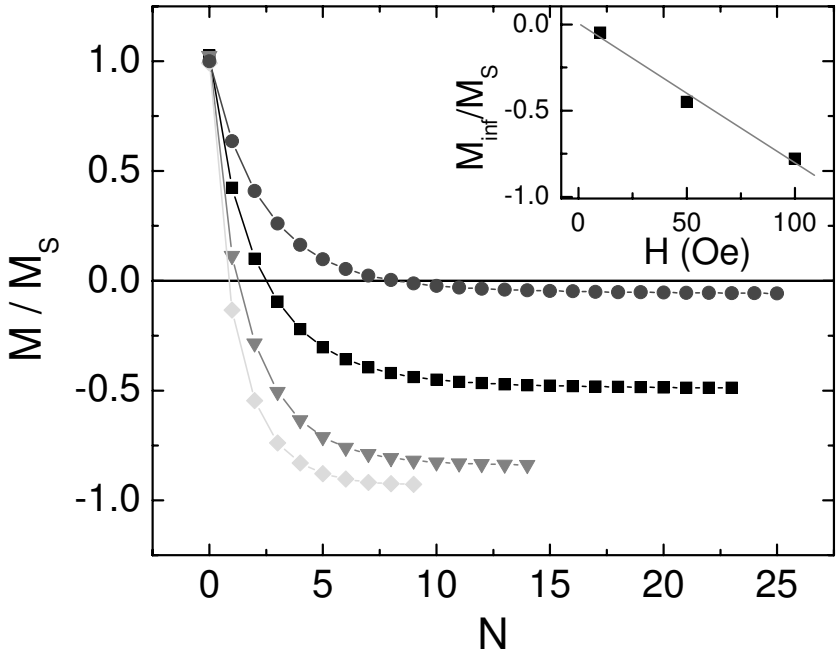

Figure IV.9: Normalized magnetization M/M_S at $T = 10$ K after each thermal cycle between 150 K and 10 K as a function of the number of cycles N. Different cooling parameters were used, $H_{FC} = 10$ Oe(circles), 50 Oe(squares), 100 Oe(upside-down triangles) with 10 K/min cooling/heating rate, and $H_{FC} = 100$ Oe with 0.1 K/min (diamonds). The lines are a guide to the eye. (Inset) Asymptotic magnetization M_∞/M_S at high cycling number N obtained by exponential fitting, as a function of H_{FC}. The straight line is a linear fit.

The above experiments of magnetization reversal dependence on the cooling speed, isothermal relaxation, and thermal activation all suggest that it is energetically favorable for the FM to reverse against H_{FC}, albeit counterintuitive since $|m_{FM}| >> |m_{AF}|$. As we argued in the introduction, this behavior cannot be explained simply by the competition between Zeeman energy and interfacial coupling. Additionally, when the FM was partially reversed upon cooling, *e.g.* at $H_{FC} = 0.1$ kOe, double hysteresis loop was found with the magnetization nearly constant for magnetic fields near zero. Therefore, $(M_S - M(10\text{K}))/2M_S$ gives the percentage of sample that exhibits positive EB at 10 K for an intermediate H_{FC}. For $H_{FC} = 0.1$ kOe, the sample is nearly 90% positively exchange biased at 10 K after 6 thermal cycles at 0.1 K/min. This very small H_{FC} necessary for positive EB challenges the present interpretation of positive EB. The interfacial coupling energy in this sample is $E_{int} = J_{FM/AF}\mathbf{S}_{FM} \cdot \mathbf{S}_{AF} = \mu_0 H_{EB} M_{FM} t_{FM} = 0.79$ erg/cm^2, close to that previously found in similar systems [12]. However, the onset H_{FC} for positive EB in this case is about two orders of magnitude smaller than previously found [52]. A new mechanism for determining the sign of AF uncompensated moments is necessary to explain the features we observe experimentally.

In summary, we find that spontaneous magnetization reversal in exchange biased bilayers exhibits strong dependence on time-dependent cooling protocols. Slower cooling or longer wait time around the Néel temperature T_N of the antiferromagnet leads to a larger magnetization reversal. Thermal cycling between above and below the Néel temperature causes the FM to reverse successively by an amount exponentially decaying with cycling. The slow dynamics and thermal training behavior suggests that spontaneously reversal is thermodynamically stable, rather than metastable as predicted by current understanding of positive EB.

While the underlying mechanism of this dynamic process is still under investigation, we believe this behavior is due to the competing interactions around T_N, when the AF is becoming ordered yet not frozen, and the sign of the exchange

bias field is determined. Preliminary numerical calculation shows that including AF and FM parallel domain wall energies can resolve the dilemma raised by current understanding of positive EB and explain the experimental features.

IV.D Acknowledgement

Chapter IV, in part, is a reprint of the material as it appears in Zhi-Pan Li, Johannes Eisenmenger, Casey W. Miller, and Ivan K. Schuller, "*Anomalous Spontaneous Reversal in Magnetic Heterostructures*," Phys. Rev. Lett. **96**, 137201 © 2006 The American Physical Society, where the dissertation author was the first author. The co-authors in this publication directed, supervised, and co-worked on the research which forms the basis of this chapter.

V

Conclusion

A ferromagnet(FM)/antiferromagnet(AF) bilayer is a prototypical magnetic heterostructure that has been heavily studied because of its intriguing physics derived from the interaction of two dissimilar magnetic systems across a buried interface. Exchange bias arises from frozen AF moments pinning the FM at the interface, which defines a preferred FM orientation and results in a shifted hysteresis loop. Many important properties of exchange bias are governed by how different quantities of the two dissimilar magnetic systems are coupled together. For example, the AF usually have much larger anisotropy than the FM while the exchange interaction is much larger in the FM. This determines that the FM domain wall width is usually much larger than that of the AF, thus, any variation on the scale of the AF domain wall width is averaged over and will not be sensed by the FM. However, variations in the AF on a scale comparable to or larger than the FM domain wall width will play a significant role in the FM magnetization reversal. Beside the importance of length scale relevance, competing interactions also play a significant role. However, a general understanding of the competition of energy and length scales in the FM and AF, and how they influence various reversal behavior is still lacking. In this thesis, we investigated three problems to gain a better understanding of competing length scales and energies: double vs. single hysteresis, asymmetric magnetization reversal, and thermally induced spon-

taneous magnetization reversal. Both continuous thin films and nanostructures were studied.

The first issue this thesis addresses is the origin and implication of doubly shifted hysteresis loops in the transition from negative to positive exchange bias, as opposed to single loop as commonly observed. We found the origin of this phenomenon lies in the relevance of lateral length scales of the FM and AF. The most important length scales of the FM and AF are the FM domain wall width and the AF domain size, respectively. When the latter is much larger than the former, as found in untwinned epitaxial AF, the sign of exchange bias is locally defined by the sign of the corresponding uncompensated AF moments, and double hysteresis occurs. When the FM domain wall width is much larger than the AF domain size, the FM averages over the domain-to-domain variation in the AF and shows a single averaged exchange bias field. In order to further probe the AF domain size, the FM layer is nanostructured into sizes from 100 nm to 600 nm. We found the cooling field necessary for positive exchange bias is nearly an order of magnitude smaller in nanostructures than that for continuous thin film. This is happening because the FM dot size is comparable with the AF domain size, which we estimated to be around 500 nm.

Then the asymmetric magnetization reversal mechanism is discussed. There are two underlying mechanisms that drive the reversal asymmetry, the first being local incomplete FM domain wall parallel to the FM/AF interface, and the second being the competing uniaxial and unidirectional anisotropies. These two mechanisms carry different weight in systems with different anisotropies. The first plays a significant role in systems with large interfacial coupling, which pins the interfacial FM moments and leads to pronounced parallel FM domain walls and asymmetric magnetization reversal. The second is important when the interfacial coupling is relatively small so that the two anisotropies are comparable. It is important to see that interfacial inhomogeneity and lateral length scale relevance are also critical in understanding the reversal asymmetry. Interfacial inhomogeneity

results in asynchronously developed parallel FM domain walls, which creates lateral domain wall patterns along with the winding of parallel domain walls. This is manifested in magnetometry as an extended tail in the transverse component up to a large magnetic field. In the second asymmetric reversal mechanism, interfacial inhomogeneity is responsible for the domain formation in the increasing field branch, where the two anisotropies compete with each other. In addition, when the FM domain wall width and AF domain size are comparable, alignment-sensitive reversal asymmetry occurs. In the presence of biaxial anisotropy, its competition with interfacial coupling and AF exchange energy causes training effect, and its competition with FM uniaxial anisotropy causes reversal asymmetry.

Beside magnetic-field-driven magnetization reversal, we found that under certain circumstances, temperature sweep can also give rise to magnetization reversal hysteresis. The magnetic field applied during the thermal cycle can tune the width and height of the hysteresis. We attribute this thermal response to the temperature dependent interfacial coupling competing with the FM Zeeman energy. A question that arises from this phenomenon is the stability of the spontaneously reversed state and the criterion for positive exchange bias. By studying the dynamic behavior the spontaneous reversal, we confirmed that the FM favors a larger magnetization reversal given slow enough cooling or long enough waiting around the Néel temperature of the AF. While positive exchange bias is still under further investigation, we believe that parallel FM and AF domain wall formation energies should also be included in the positive exchange bias model to resolve issues raised by spontaneous magnetization reversal.

In the end, I will summarize the key elements in understanding exchange bias. Although exchange bias is such a subtle phenomenon that involves many different factors that complicate the matter, but they all lie within the scope of the basic elements I will mention below, and can be understood by straightforward Stoner-Wolfarth calculation or simple micromagnetic simulation.

The most important of all is frozen uncompensated AF moments and

their coupling with free FM moments across the interface. Although the origin and spatial distribution of these uncompensated AF moments, their response to temperature or magnetic field, and the nature of the interfacial coupling are still under investigation, it is agreed by most researchers that they are necessary conditions of exchange bias. Moreover, uncompensated AF moments not only reside at the interface and directly interact with the FM, but also in the bulk of the AF. Uncompensated AF moments in the bulk stabilizes those at the interface, and are central to domain-state model of exchange bias. Their existence and significance were also confirmed by neutron and x-ray scattering and FM/AF/FM tri-layer experiment. Equally important is structural defects at the interface, in the FM and AF. Many theoretical models rely on the presence of the surface roughness, dilution of the AF by defects, or AF grains. In our experiment, we also found that interfacial inhomogeneity are clearly manifested in both mechanisms of asymmetric reversal proposed in this thesis. Next key element is magnetic anisotropy. As mentioned above, the relationship of the anisotropy in the AF and FM determines their length scale relevance. It also gives rise to various reversal asymmetries. The last is the FM and AF domains with domain wall either parallel or perpendicular to the interface. Much effort has been devoted into understanding the role of domains in exchange bias by microscopy, magnetometry, and nanostructuring.

In this thesis, I discussed about three problems, unraveled the important role of energy and length scale relevance in exchange bias, developed a simple method to simulate exchange bias by micromagnetics, and discovered a new way of achieving magnetization reversal. This understanding may be extended to other heterostructures that involve two or more dissimilar magnetic systems of various length and energy scales.

V.A Open Issues

1. Length scale relevance

- The respective role of AF incomplete domain wall, unpinned AF moments and inhomogeneity-induced frustration in coercivity enhancement.

2. Asymmetric Magnetization Reversal

   - The role of hybrid FM and AF incomplete domain walls parallel to the interface in reversal asymmetry.
   - Observation of the local incomplete domain wall by microscopy to confirm the micromagnetic simulation result.
   - The role of four-fold anisotropy of the AF in training effect and reversal asymmetry.
   - Detailed examination of the parameter space with biaxial and uniaxial anisotropy in the AF. And is it possible to cause kinked hysteresis without introducing biaxial anisotropy into the FM?

3. Thermally induced spontaneous magnetization reversal

   - The dependence of onset cooling field for positive exchange bias on the AF/FM thickness, interfacial roughness, or lateral dispersion of spin axis orientation.
   - The role of ZnF_2 on the onset cooling field for positive exchange bias. Other related question is how ZnF_2 modifies the crytallinity of FeF_2, results in reduced exchange bias field.

4. Exchange biased nanostructures

   - The development of vortex state in exchange biased sub-micron dots, as compared with unbiased dots.

A

Tables of Material Crystallographic and Magnetic Constants

Table A.1: Crystallographic parameters for FeF_2, MnF_2, ZnF_2, MgF_2, MgO obtained from Power Diffraction File (PDF-4), published by International Centre for Diffraction Data. Important crystalline surfaces for this work and the corresponding x-ray diffraction peak position 2θ for a Cu Kα source are also listed. All above materials have tetragonal or cubic structure.

Material	a	c	Important surface	2θ
FeF_2	4.7035	3.3056	(110)	26.796
MnF_2	4.8736	3.3100	(110)	25.840
ZnF_2	4.711	3.132	(110)	26.772
MgF_2	4.6200	3.0509	(110)	27.298
MgO	4.2112	4.2112	(100)	42.953

Table A.2: Micromagnetic parameters of Fe Ni, and Co at room temperature [73]. Saturation magnetization $\mu_0 M_s$, exchange stiffness A, anisotropy K_1, and Bloch domain wall width δ are listed. The values for Fe and Ni are uniaxial estimates.

Material	$\mu_0 M_s$(T)	A(pJ)	K_1(MJ/m^3)	δ(nm)
Fe	2.15	8.3	0.05	40
Co	1.76	10.3	0.53	14
Ni	0.61	3.4	-0.005	82

Table A.3: Magnetic constants of FeF_2 [61].

Quantity	value
Exchange constant along [001] J_1	-0.048 cm^{-1}
Exchange constant along [111] J_2	3.46 cm^{-1}
Exchange constant along [100] J_3	0.149 cm^{-1}
Uniaxial anisotropy K_1	1.35×10^4 kJ/m^3
Spin of an Fe ion S	2
Néel Temperature T_N	78.4 K

B

Table of Samples Studied

Sample	Structure	Comments
ZFFF02A	MgO(100) / FeF_2(20 nm) / Fe(30 nm) / Al(4 nm)	Patterned into dots from 100 to 600 nm diameter. Over-etched for 2 hours into FeF_2 and substrate. AFM pictures taken. MOKE measured.
ZFFF03A	MgO(100) / FeF_2(20 nm) / Fe(30 nm) / Al(4 nm)	Patterned into dots from 100 to 600 nm diameter. MOKE measured.
ZFFF05A	MgO(100) / FeF_2(20 nm) / Fe(10 nm) / Al(4 nm)	Patterned into dots from 100 to 600 nm diameter. Resist not fully removed. MOKE measured.
102103W1	MgO(100) / MnF_2(40 nm) / Fe(0-6.4 nm) / Co (0.5 nm) / Al(5 nm?)	Sent to Kai Liu for XMCD at ALS. Al thickness uncontrolled.
102203W2	MgO(100) / FeF_2(40 nm) / Fe(0-6.4 nm) / Co (0.5 nm?) / Al(5 nm?)	Sent to Kai Liu for XMCD at ALS. Co and Al thickness uncontrolled.
020904W3	MgF_2(110) / FeF_2(50 nm) / Co(1 nm) / Fe(1 nm) / Ni(1 nm) / FeF_2(1 nm)	Sent to Kai Liu for XMCD at ALD.
021004W4	MgO(100) / FeF_2(40 nm) / Fe(0-6 nm) / Co(0.5 nm) / Al(2.5 nm)	Sent to Kai Liu for XMCD at ALD.
021004W5	MgO(100) / FeF_2(40 nm) / Fe(0-6 nm) / Co(0.5 nm) / Fe(6-0 nm) / Al(2.5 nm)	Double wedge sample sent to Kai Liu for XMCD at ALS.
021104W6	MgO(100) / FeF_2(40 nm) / Fe(0-3 nm) / Co(0.5 nm) / Fe(3-0 nm) / Al(2.5 nm)	Double wedge sample sent to Kai Liu for XMCD at ALS.
ZF09	MgF_2(110) / FeF_2(50 nm) / Fe(21 nm) / Al(7.6 nm)	NO Double loop. Small EB (¡200Oe). MTI substrate.

Sample	Structure	Comments
ZF10	MgF_2(110) / FeF_2(50 nm) / Ni(3.8 nm) / Al(2.5 nm)	Double loop. Crystec substrate.
ZF11	MgF_2(110) / FeF_2(50 nm) / Ni(3.8 nm) / Al(2.5 nm)	No double loop. MTI substrate.
ZF12	MgF_2(110) / FeF_2(50 nm)	Linear response to magnetic field sweep.
ZF13	MgF_2(110) / FeF_2(50 nm) / Ni(21 nm) / Al(7.6 nm)	Ni grown at 300°C. Large coercivity. Double loop.
ZF14	MgF_2(110) / FeF_2(50 nm) / Ni(26.4-74.2 nm) / Al(7.6 nm)	MOKE measured. No clear trend found.
BIF7P7A	MgF_2(110) / FeF_2(70 nm) / Py(7 nm) / Al (4 nm)	MOKE from both sides of the sample measured.
BIF7N7A	MgF_2(110) / FeF_2(70 nm) / Ni(7 nm) / Al (4 nm)	MOKE from both sides of the sample measured.
BIF7F7A	MgF_2(110) / FeF_2(70 nm) / Fe(7 nm) / Al (4 nm)	MOKE from both sides of the sample measured.
ZF16	MgF_2(110) / FeF_2(50 nm)	AFM imaged. MTI substrate.
ZF17	MgF_2(110) / FeF_2(50 nm)	AFM imaged. Crystec substrate.
ZF18	MgF_2(110) / FeF_2(50 nm) / Ni(3.8 nm) / Al(2.5 nm)	SQUID strange result. Possible contamination.
ZF19	MgF_2(110) / FeF_2(50 nm) / Ni(3.8 nm) / Al(2.5 nm)	SQUID unfinished. Possible contamination?
ZF20	MgF_2(110) / FeF_2(50 nm) / Ni(21 nm) / Al(7.6 nm)	Crystec. Evaporated together with ZF21. Unbiased component found.
ZF21	MgF_2(110) / FeF_2(50 nm) / Ni(21 nm) / Al(7.6 nm)	MTI. Partly unbiased. Double loop.
ZF22	MgF_2(110) / FeF_2(50 nm) / Ni(3.8 nm) / Al(3 nm)	Crystec. Evaporated together with ZF23. Double loop, but not clear.
ZF23	MgF_2(110) / FeF_2(50 nm) / Ni(3.8 nm) / Al(3 nm)	MTI. No double loop.
081204W1	MgF_2(110) / FeF_2(50 nm) / Ni(0-2 nm) / Ni(0.5-2.5 nm) / Al(2.5 nm)	Control sample for 081204W2. Sent to Kai Liu for XMCD at ALS.
081204W2	MgF_2(110) / FeF_2(50 nm) / Ni(0-2 nm) / Co(0.3 nm) / Ni(0.5-2.5 nm) / Al(2.5 nm)	Sent to Kai Liu for XMCD at ALS.
082404W1	MgF_2(110) / FeF_2(50 nm) / Ni(0-2 nm) / Ni(0.3 nm) / Ni(0.5-2.5 nm) / Al(2.5 nm)	Control sample for 082404W2. Sent to Kai Liu for XMCD at ALS.

Sample	Structure	Comments
082404W2	MgF_2(110) / FeF_2(50 nm) / Ni(0-2 nm) / Co(0.1 nm) / Ni(0.5-2.5 nm) / Al(2.5 nm)	Apparent non-uniform thickness. Sent to Kai Liu for XMCD at ALS.
082404W3	MgF_2(110) / FeF_2(50 nm) / Ni(0-2 nm) / Co(0.2 nm?) / Ni(0.5-2.5 nm) / Al(2.5 nm)	Sent to Kai Liu for XMCD at ALS.
ZF26	MgF_2(110) / FeF_2(50 nm) / Fe(4 nm) / Al(4 nm)	Strange loop shape.
ZF27	MgF_2(110) / FeF_2(50 nm) / Fe(4 nm) / Al(4 nm)	Double loop, but not sharp. Easy/hard axis hysteresis measured.
091804W1	MgF_2(110) / FeF_2(50 nm) / Ni(0-2 nm) / Ni(0.1 nm) / Ni(0.5-2.5 nm) / Al(2.5 nm)	Control sample for 091804W2. Sent to Kai Liu for XMCD at ALS.
091804W2	MgF_2(110) / FeF_2(50 nm) / Ni(0-2 nm) / Co(0.1 nm) / Ni(0.5-2.5 nm) / Al(2.5 nm)	Sent to Kai Liu for XMCD at ALS.
091804W3	MgF_2(110) / FeF_2(50 nm) / Ni(2-3 nm) / Al(2.5 nm)	Control sample for 091804W2. Sent to Kai Liu for XMCD at ALS.
ZF29	MgF_2(110) / Ni(50 nm) / FeF_2(30 nm) / Al(4 nm)	Small exchange bias field. (=BN5A3).
ZF30	MgF_2(110) / Ni(50 nm) / FeF_2(30 nm) / Ni(70 nm) / Al(4 nm)	FM/AF/FM trilayer. (=TN5A3N7).
ZF31	MgF_2(110) / FeF_2(30 nm) / Ni(21 nm) / Al(4 nm)	Good double hysteresis. O_2 baking is important.
ZF32	MgF_2(110) / FeF_2(30 nm) / Ni(70 nm) / FeF_2(30 nm) / Al(4 nm)	AF/FM/AF trilayer. Good double loop. Small exchange bias field.
ZF33	MgF_2(110) / FeF_2(30 nm) / Fe(4 nm) / Al(4 nm)	Thin Fe. Double loop. Different shape than Ni sample.
ZF34	MgF_2(110) / FeF_2(30 nm) / Ni(4 nm) / FeF_2(10 nm) / Al(4 nm)	AF/FM/AF trilayer. Two overlapping hysteresis found.
ZF35	MgO(100) / ZnF_2(20 nm) / MnF_2(30 nm) / Co(3 nm) / Al(2.5 nm)	Sent to Kai Liu for XMCD at ALS. No EB.
ZF36	MgO(100) / ZnF_2(20 nm) / MnF_2(30 nm) / Co(3 nm) / Al(2.5 nm)	Sent to Kai Liu for XMCD at ALS. No EB.
ZF37	MgF_2(110) / ZnF_2(30 nm) / FeF_2(30 nm) / Co(3 nm) / Al(2.5 nm)	Spontaneous magnetization reversal found.
ZF38	MgF_2(110) / FeF_2(50 nm) / Ni(3 nm) / Al(3 nm)	Sent to Kai Liu for XMCD at ALS. Tuneable exchange bias from negative to positive.

Sample	Structure	Comments
ZF39	MgF_2(110) / ZnF_2(0-10 nm) / FeF_2(30 nm) / Ni(2.5 nm) / Al(2.5 nm)	ZnF_2 wedge. Sent to Kai Liu for XMCD at ALS. Reduced EB field with increasing ZnF_2 thicknesses.
ZF39K	Si / FeF_2(50 nm) / Ni(21 nm) / Al(7.6 nm)	Sent to Kai Liu for vector magnetometry.
ZF40K	MgO(100) / FeF_2(50 nm) / Ni(21 nm) / Al(7.6 nm)	Sent to Kai Liu for vector magnetometry.
ZF41K	MgF_2(110) / FeF_2(50 nm) / Ni(21 nm) / Al(7.6 nm)	Sent to Kai Liu for vector magnetometry.
ZF41	MgF_2(110) / ZnF_2(30 nm) / FeF_2(50 nm) / Co(4 nm) / Al(2.5 nm)	Sent to Sujoy Roy for x-ray speckle experiment.
ZF44	MgF_2(110) / FeF_2(50 nm) / Co(3.8 nm) / Al(2.5 nm)	Sent to Mike Fitzsimmons for polarized neutron reflectivity measurment.
ZF53	MgO(100) / FeF_2(50 nm) / Ni(30 nm) / Al(4.1 nm)	Patterned into nanodots. Unable to remove resist.
ZF54	MgF_2(110) / FeF_2(50 nm) / Ni(30 nm) / Al(4.1 nm)	Patterned into nanodots. Found onset cooling field for positive exchange bias depends on dot sizes.
ZF57	MgF_2(110) / FeF_2(50 nm) / Co(3.8 nm) / Al(2.5 nm)	Sent to Sujoy Roy for diffuse scattering experiment.
ZF58	MgF_2(110) / FeF_2(50 nm) / Fe(30 nm) / Al(8.4 nm)	Sent to Kai for vector magnetometry.
ZF59	MgO(100) / FeF_2(30 nm) / Co(3 nm) / Al(2.5 nm)	Prepared for Maria Varela for cross sectional STEM. Discarded due to STEM breakdown.
ZF60	MgF_2(110) / FeF_2(30 nm) / Co(3 nm) / Al(2.5 nm)	Prepared for Maria Varela for cross sectional STEM. Bad samples. Discarded
ZF63	MgO(100) / FeF_2(30 nm) / Co(3 nm) / Al(2.5 nm)	Sent to Maria Varela for cross sectional STEM.
ZF64	MgF_2(110) / FeF_2(30 nm) / Co(3 nm) / Al(2.5 nm)	Sent to Maria Varela for cross sectional STEM.
ZF65	MgF_2(110) / FeF_2(50 nm) / Co(4 nm) / Al(2.5 nm)	2×2 cm^2 MgF_2 substrate. No positive EB at 7 kOe cooling field. Sent to Mike Fitzsimmons for neutron scattering.
IZ051606	MgF_2(110) / FeF_2(50 nm) / Al(2.5 nm)	Hysteresis found.

Sample	Structure	Comments
ZF66	MgF_2(110) / FeF_2(50 nm) / Co(3.8 nm) / Al(3 nm)	2×2 cm^2 MgF_2 substrate. Sent to Mike Fitzsimmons for neutron scattering.
ZF67	MgF_2(110) / FeF_2(50 nm) / Al(3 nm)	Hysteresis found.
ZF68	MgF_2(110) / FeF_2(50 nm) / Co(3.8 nm) / Al(3 nm)	No positive EB at 7 kOe cooling field.
ZF69	MgF_2(110) / FeF_2(50 nm) / Co(3.8 nm) / Al(2.5 nm)	No positive EB at 7 kOe cooling field.
ZF70	MgF_2(110) / FeF_2(50 nm) / Co(3.8 nm) / Al(2.5 nm)	2×2 cm^2 MgF_2 substrate. No positive EB at 7 kOe cooling field. Sent to Mike for neutron scattering.
IZ072606	MgF_2(110) / FeF_2(50 nm) / Co(3.8 nm) / Al(2.5 nm)	Prepared for neutron scattering.

Bibliography

[1] W. H. Meiklejohn and C. P. Bean, Phys. Rev. **105**, 904 (1957).

[2] J. Nogués and I. K. Schuller, J. Magn. Magn. Mat. **192**, 203 (1999).

[3] M. Kiwi, J. Magn. Magn. Mat. **234**, 584 (2001).

[4] J. C. S. Kools, IEEE Trans. Magn. **32**, 3165 (1996).

[5] M. R. Fitzsimmons, P. Yashar, C. Leighton, I. K. Schuller, J. Nogués, C. F. Majkrzak, and J. A. Dura, Phys. Rev. Lett. **84**, 3986 (2000).

[6] V. Skumryev, S. Stoyanov, Y. Zhang, G. Hadjipanayis, D. Givord, and J. Nogués, Nature **423**, 850 (2003).

[7] K. Liu, J. Nogués, C. Leighton, H. Masuda, K. Nishio, I. V. Roshchin, and I. K. Schuller, Appl. Phys. Lett. **81**, 4434 (2002).

[8] J. Nogués, D. Lederman, T. J. Moran, and I. K. Schuller, Phys. Rev. Lett. **76**, 4624 (1996a).

[9] D. Paccard, C. Schlenker, O. Massenet, R. Montmory, and A. Yelon, Phys. Status Solidi **16**, 301 (1966).

[10] A. Hoffmann, Phys. Rev. Lett. **93**, 97203 (2004).

[11] D. Mauri, E. Kay, D. Scholl, and J. K. Howard, J. Appl. Phys. **62**, 2929 (1987a).

[12] J. Nogués, D. Lederman, T. J. Moran, I. K. Schuller, and K. V. Rao, Appl. Phys. Lett. **68**, 3186 (1996b).

[13] N. C. Koon, Phys. Rev. Lett. **78**, 4865 (1997).

[14] H. Suhl and I. K. Schuller, Phys. Rev. B **58**, 258 (1998).

[15] D. Mauri, H. C. Siegmann, P. S. Bagus, and E. Kay, J. Appl. Phys. **62**, 3047 (1987b).

[16] M. Kiwi, J. Mejía-López, R. D. Portugal, and R. Ramírez, Appl. Phys. Lett. **75**, 3995 (1999).

[17] M. D. Stiles and R. D. McMichael, Phys. Rev. B **59**, 3722 (1999).

[18] T. C. Schulthess and W. H. Butler, Phys. Rev. Lett. **81**, 4516 (1998).

[19] A. P. Malozemoff, Phys. Rev. B **35**, 3679 (1987).

[20] K. Takano, R. H. Kodama, A. E. Berkowitz, W. Cao, and G. Thomas, Phys. Rev. Lett. **79**, 1130 (1997).

[21] C. Binek, X. Chen, A. Hochstrat, and W. Kleemann, J. Magn. Magn. Mat. **240**, 257 (2002).

[22] U. Nowak, K. D. Usadel, J. Keller, P. Miltényi, B. Beschoten, and G. Güntherodt, Phys. Rev. B **66**, 14430 (2002).

[23] S. Urazhdin and C. L. Chien, Phys. Rev. B **71**, 220410 (2005).

[24] C. L. Chien, V. S. Gornakov, V. I. Nikitenko, A. J. Shapiro, and R. D. Shull, Phys. Rev. B **68**, 14418 (2003).

[25] J. R. Fermin, M. A. Lucena, A. Azevedo, F. M. de Aguiar, and S. M. Rezende, J. Appl. Phys. **87**, 6421 (2000).

[26] A. Scholl, M. Liberati, E. Arenholz, H. Ohldag, and J. Stöhr, Phys. Rev. Lett. **92**, 247201 (2004a).

[27] H. Ohldag, T. J. Regan, J. Stöhr, A. Scholl, F. Nolting, J. Lüning, C. Stamm, S. Anders, , and R. L. White, Phys. Rev. Lett. **87**, 247201 (2001).

[28] K. S. Lee, S. K. Kima, and J. B. Kortright, Appl. Phys. Lett. **83**, 3764 (2003).

[29] E. F. Kneller and R. Hawig, IEEE Trans. Magn. **27**, 3588 (1991).

[30] E. E. Fullerton, J. S. Jiang, M. Grimsditch, C. H. Sowers, and S. D. Bader, Phys. Rev. B **58**, 12193 (1998).

[31] P. Miltényi, M. Gierlings, J. Keller, B. Beschoten, and G. Güntherodt, Phys. Rev. Lett. **84**, 4224 (2000).

[32] J.-I. Hong, T. Leo, D. J. Smith, and A. E. Berkowitz, Phys. Rev. Lett. **96**, 117204 (2006).

[33] H. Shi, D. Lederman, N. R. Dilley, R. C. Black, J. Diedrichs, K. Jensen, and M. B. Simmonds, J. Appl. Phys. **93**, 8600 (2003).

[34] H. Shi, D. Lederman, and E. E. Fullerton, J. Appl. Phys. **91**, 7763 (2002).

[35] H. Shi and D. Lederman, Phys. Rev. B **66**, 94426 (2002).

[36] B. Beschoten, J. Keller, P. Miltényi, and G. Güntherodt, J. Magn. Magn. Mat. **240**, 248 (2001).

[37] H. Ohldag, A. Scholl, F. Nolting, E. Arenholz, S. Maat, A. Young, M. Carey, and J. Stöhr, Phys. Rev. Lett. **91**, 17203 (2003).

[38] P. Kappenberger, S. Martin, Y. Pellmont, H. J. Hug, J. B. Kortright, O. Hellwig, and E. E. Fullerton, Phys. Rev. Lett. **91**, 267202 (2003).

[39] S. Roy, M. Fitzsimmons, S. Park, M. Dorn, O. Petracic, I. V. Roshchin, Z.-P. Li, X. Batlle, R. Morales, A. Misra, X. Zhang, K. Chesnel, J. Kortright, S. Sinha, and I. K. Schuller, Phys. Rev. Lett. **95**, 47201 (2005).

[40] P. Blomqvist, K. M. Krishnan, and H. Ohldag, Phys. Rev. Lett. **94**, 107203 (2000).

[41] K. Liu, S. M. Baker, M. Tuominen, T. P. Russell, and I. K. Schuller, Phys. Rev. B **63**, 60403 (2001).

[42] X. Portier, A. K. Petford-Long, A. de Morais, N. W. Owen, H. Laidler, and K. O'Grady, J. Appl. Phys. **87**, 6412 (2000).

[43] V. I. Nikitenko, V. S. Gornakov, A. J. Shapiro, R. D. Shull, K. Liu, S. M. Zhou, and C. L. Chien, Phys. Rev. Lett. **84**, 765 (2000).

[44] J. Eisenmenger, Z.-P. Li, W. A. A. Macedo, and I. K. Schuller, Phys. Rev. Lett. **94**, 57203 (2005).

[45] M. Gierlings, M. J. Prandolini, H. Fritzsche, M. Gruyters, and D. Riegel, Phys. Rev. B **65**, 92407 (2002).

[46] C. Leighton, M. R. Fitzsimmons, P. Yashar, A. Hoffmann, J. Nogués, J. Dura, C. F. Majkrzak, and I. K. Schuller, Phys. Rev. Lett. **86**, 4394 (2001).

[47] S. Brems, D. Buntinx, K. Temst, C. V. Haesendonck, F. Radu, and H. Zabel, Phys. Rev. Lett. **95**, 157202 (2005).

[48] B. Beckmann, U. Nowak, and K. D. Usadel, Phys. Rev. Lett. **91**, 187201 (2003).

[49] J. Camarero, J. Sort, A. Hoffmann, J. M. García-Martín, B. Dieny, R. Miranda, and J. Nogués, Phys. Rev. Lett. **95**, 57204 (2005).

[50] Z. Li and S. Zhang, Appl. Phys. Lett. **77**, 423 (2000a).

[51] J. Nogués, C. Leighton, and I. K. Schuller, Phys. Rev. B **61**, 1315 (2000).

[52] C. Leighton, J. Nogués, H. Suhl, and I. K. Schuller, Phys. Rev. B **60**, 12837 (1999).

[53] X. Ke, M. Rzchowski, L. Belenky, and C. Eom, Appl. Phys. Lett. **84**, 5458 (2004).

[54] F. Canet, S. Mangin, C. Bellouard, and M. Piecuch, Europhys. Lett. **52**, 594 (2000).

[55] O. Petracic, Z.-P. Li, I. V. Roshchin, M. Viret, R. Morales, X. Batlle, and I. K. Schuller, Appl. Phys. Lett. **87**, 222509 (2005).

[56] P. Miltényi, M. Gierlings, M. Bamming, U. May, G. Güntherodt, J. Nogués, M. Gruyters, C. Leighton, and I. K. Schuller, Appl. Phys. Lett. **75**, 2304 (1999).

[57] I. Roshchin, O. Petracic, R. Morales, Z.-P. Li, X. Batlle, and I. K. Schuller, Europhys. Lett. **71**, 297 (2005).

[58] E. Arenholz, K. Liu, Z.-P. Li, and I. K. Schuller, Appl. Phys. Lett. **88**, 72503 (2006).

[59] M. R. Fitzsimmons, B. J. Kirby, S. Roy, Z.-P. Li, I. V. Roshchin, S. K. Sinha, and I. K. Schuller, (unpublished).

[60] C. Leighton, J. Nogués, B. J. J. Åkerman, and I. K. Schuller, Phys. Rev. Lett. **84**, 3466 (2000a).

[61] M. T. Hutchings, B. D. Rainford, and H. J. Guggenheim, J. Phys. C. Solid St. Phys. **3**, 307 (1970).

[62] J. Strempfer, U. Rütt, and W. Jauch, Phys. Rev. Lett. **86**, 3152 (2001).

[63] Spin-flop is not observed in the samples discussed here.

[64] I. Henins and J. A. Bearden, Phys. Rev. **135** (1964).

[65] P. M. Oppeneer, *Handbook of Magnetic Materials* (Elsevier, Amsterdam, 2001), vol. 13.

[66] J. Kerr, Philos. Mag. **3**, 321 (1877).

[67] Z. J. Yang and M. R. Scheinfein, J. Appl. Phys. **74** (1993).

[68] *CRC Handbook of Chemistry and Physics* (CRC Press, Boca Raton, 2004), pp. 12–133 to 12–156, 85th ed.

[69] W. Voigt, *Magneto- und Electrooptik* (B. G. Teubner, Leipzig, 1908).

[70] OOMMF code. http://math.nist.gov/oommf.

[71] J. W. F. Brown, *Micromagnetics* (Krieger, New York, 1978).

[72] H. Shi, D. Lederman, K. V. O'Donovan, and J. A. Borchers, Phys. Rev. B **69**, 214416 (2004).

[73] R. Skomski, J. Phys. Cond. Mat. **15**, R841 (2003).

[74] M. Fraune, U. Rüdiger, G. Güntherodt, S. Cardoso, and P. Freitas, Appl. Phys. Lett. **77**, 3815 (2000).

[75] J.-G. Zhu, Y. Zheng, and X. Lin, J. Appl. Phys. **81**, 4336 (1997).

[76] Y.-J. Wang and C.-H. Lai, J. Appl. Phys. **89**, 7537 (2001).

[77] V. Baltz, J. Sort, S. Landis, B. Rodmacq, and B. Dieny, Phys. Rev. Lett. **94**, 117201 (2005).

[78] N. J. Gökemeijer and C. L. Chien, J. Appl. Phys. **85**, 5516 (1999).

[79] J. Olamit, E. Arenholz, Z.-P. Li, O. Petracic, I. V. Roshchin, I. K. Schuller, and K. Liu, Phys. Rev. B **72**, 12408 (2005).

[80] T. L. Kirk, O. Hellwig, and E. E. Fullerton, Phys. Rev. B **65**, 224426 (2002).

[81] C.-H. Lai, Y.-H. Wang, C.-R. Chang, J.-S. Yang, and Y. D. Yao, Phys. Rev. B **64**, 94420 (2001).

[82] T. Zhao, H. Fujiwara, K. Zhang, C. Hou, and T. Kai, Phys. Rev. B **65**, 14431 (2001).

[83] L. Wee, R. L. Stamps, L. Malkinski, and Z. Celinski, Phys. Rev. B **69**, 134426 (2004).

[84] C. Leighton, H. Suhl, M. J. Pechan, R. Compton, J. Nogues, and I. K. Schuller, J. Appl. Phys. **92**, 1483 (2002).

[85] M. Grimsditch, A. Hoffmann, P. Vavassori, H. Shi, and D. Lederman, Phys. Rev. Lett. **90**, 257201 (2003).

[86] X. Chen, C. Binek, A. Hochstrat, and W. Kleemann, Phys. Rev. B **65**, 12415 (2001).

[87] M. R. Fitzsimmons, C. Leighton, J. Nogués, A. Hoffmann, K. Liu, C. F. Majkrzak, J. A. Dura, J. R. Groves, R. W. Springer, P. N. Arendt, V. Leiner, H. Lauter, and I. K. Schuller, Phys. Rev. B **65**, 134436 (2002).

[88] There are complications when the first rotated domain is very small so that it cannot completely overcome the unidirectional anisotropy in the second domain and drag that large domain to also rotate in the same direction. There the opposite field-sweep shows more clearly the two successive rotations, hence our choice of the $m_\perp$ fraction definition.

[89] J. Nogués, T. J. Moran, D. Lederman, I. K. Schuller, and K. V. Rao, Phys. Rev. B **59**, 6984 (1999).

[90] Z. Li and S. Zhang, Phys. Rev. B **61**, R14897 (2000b).

[91] A. Scholl, F. Nolting, J. W. Seo, H. Ohldag, J. Stöhr, S. Raoux, J.-P. Locquet, and J. Fompeyrine, Appl. Phys. Lett. **85**, 4085 (2004b).

[92] Z.-P. Li, O. Petracic, J. Eisenmenger, and I. K. Schuller, Appl. Phys. Lett. **86**, 72501 (2005).

[93] Z.-P. Li, O. Petracic, R. Morales, J. Olamit, X. Batlle, K. Liu, and I. K. Schuller, Phys. Rev. Lett. **96**, 217205 (2006a).

[94] Z.-P. Li, J. Eisenmenger, C. W. Miller, and I. K. Schuller, Phys. Rev. Lett. **96**, 137201 (2006b).

[95] M. T. Hutchings, M. P. Schulhof, and H. J. Guggenheim, Phys. Rev. B **5**, 154 (1972).

[96] In bulk FeF_2 there are three exchange constants, where $J_2 = -0.45$ meV is the dominant coupling constant with *eight* neighbors.

[97] A. Tillmanns and S. Oertker and B. Beschoten and G. Güntherodt and C. Leighton and Ivan K. Schuller and J. Nogués, Condmat/501006, 2005.

[98] C. Daboo, R. J. Hicken, E. Gu, M. Gester, S. J. Gray, D. E. P. Eley, E. Ahmad, J. A. C. Bland, R. Ploessl, and J. N. Chapman, Phys. Rev. B **51**, 15964 (1995).

[99] The interfacial coupling that gives the best fit to the experiment is $J_{FM/AF} =$ -0.88 eV, comparable with the exchange coupling in FeF_2 -0.45 eV from Ref. 13. This number is not meaningful in its absolute value because it depends on the assumed number, 7% in our case, of the frozen AF uncompensated moments.

[100] J. E. Davies, O. Hellwig, E. E. Fullerton, J. S. Jiang, S. D. Bader, G. T. Zimanyi, and K. Liu, Appl. Phys. Lett. **86**, 262503 (2005).

[101] Micromagnetic parameters $M_S = 800$ kA/m and $A = 13$ pJ/m of Py used are from Ref. [73].

[102] The interfacial coupling is found to be -0.52 eV.

[103] A. Misra, U. Nowak, and K. D. Usadel, J. Appl. Phys. **95**, 1357 (2004).

[104] M. R. Scheinfein, J. Unguris, R. J. Celotta, and D. T. Pierce, Phys. Rev. Lett. **63** (1989).

[105] A. Tillmanns and S. Oertker and B. Beschoten and G. Güntherodt and J. Eisenmenger and Ivan K. Schuller, Condmat/509419, 2005.

[106] T. Gredig, I. N. Krivorotov, and E. D. Dahlberg, J. Appl. Phys. **91**, 7760 (2002).

[107] R. L. Stamps, J. Phys. D **33**, R247 (2000).

[108] A. Mougin, S. Poppe, J. Fassbender, B. Hillebrands, G. Faini, U. Ebels, M. Jung, D. Engel, A. Ehresmann, and H. Schmoranzer, J. Appl. Phys. **89**, 6606 (2001).

[109] J. Yu, A. D. Kent, and S. S. P. Parkin, J. Appl. Phys. **87**, 5049 (2000).

[110] A. Hoffmann, M. Grimsditch, J. E. Pearson, J. Nogus, W. A. A. Macedo, and I. K. Schuller, Phys. Rev. B **67**, 220406 (2003).

[111] R. M. Osgood, III, S. D. Bader, B. M. Clemens, R. L. White, and H. Matsuyama, J. Magn. Magn. Mat. **182** (1998).

[112] T. Ambrose and C. L. Chien, J. Appl. Phys. **83**, 7222 (1998).

[113] C. Tsang and K. Lee, J. Appl. Phys. **53**, 2605 (1983).

[114] F. Radu, M. Etzkorn, T. Schmitte, R. Siebrecht, A. Schreyer, K. Westerholt, and H. Zabel, J. Magn. Magn. Mat. **240**, 251 (2002).

[115] C. Leighton, M. Song, J. Nogués, M. C. Cyrille, and I. K. Schuller, J. Appl. Phys. **88**, 344 (2000b).

[116] I. N. Krivorotov, C. Leighton, J. Nogués, I. K. Schuller, and E. D. Dahlberg, Phys. Rev. B **65**, 100402 (2002).

[117] A. Kirilyuk, T. Rasing, H. Jaffrès, D. Lacour, and F. N. V. Dau, J. Appl. Phys. **91**, 7745 (2002).

[118] J. McCord, R. Schäfer, R. Mattheis, and K.-U. Barholz, J. Appl. Phys. **93**, 5491 (2003).

[119] M. S. Lund, W. A. A. Macedo, K. Liu, J. Nogués, I. K. Schuller, and C. Leighton, Phys. Rev. B **66**, 54422 (2002).

[120] U. Nowak, A. Misra, and K. D. Usadel, J. Appl. Phys. **89**, 7269 (2001).

[121] M. Hanson, O. Kazakova, P. Blomqvist, R. Wäppling, and B. Nilsson, Phys. Rev. B **66**, 144419 (2002).

[122] M. Grimsditch, Y. Jaccard, and I. K. Schuller, Phys. Rev. B **58**, 11539 (1998).

[123] S. Zhang and Z. Li, Phys. Rev. B **65**, 54406 (2001).

[124] J. K. Ha, R. Hertel, and J. Kirschner, Phys. Rev. B **67**, 224432 (2003).

[125] R. P. Cowburn, J. Phys. D **33**, 0 (2000).

[126] J. I. Martín, J. Nogués, K. Liu, J. L. Vicent, and I. K. Schuller, J. Magn. Magn. Mat. **256**, 449 (2003).

[127] Y. Imry, *Introduction to Mesoscopic Physics* (Oxford University Press, Oxford, 1997).

[128] D. D. Awschalom, D. Loss, and N. Samarth, eds., *Semiconductor Spintronics and Quantum Computation* (Springer, Berlin, 2002).

[129] M. N. Baibich, J. M. Broto, A. Fert, F. N. V. Dau, F. Petroff, P. Etienne, G. Creuzet, A. Friederich, and J. Chazelas, Phys. Rev. Lett. **61**, 2472 (1988).

[130] S. A. Wolf, D. D. Awschalom, R. A. Buhrman, J. M. Daughton, S. von Molnár, M. L. Roukes, A. Y. Chtchelkanova, and D. M. Treger, Science **294**, 1488 (2001).

[131] I. Zutic, J. Fabian, and S. D. Sarma, Rev. Mod. Phys. **76**, 323 (2004).

[132] P. Weiss, Science News **169**, 11 (2006).

[133] E. B. Myers, D. C. Ralph, J. A. Katine, R. N. Louie, and R. A. Buhrman, Science **285**, 867 (1999).

[134] E. L. Venturini and P. M. Richards, J. Appl. Phys. **47**, 1632 (1976).

[135] S. Demirtas, M. R. Hossu, R. E. Camley, H. C. Mireles, and A. R. Koymen, Phys. Rev. B **72**, 184433 (2005).